CONTROLLING ENTRAINMENT IN LARGE-EDDY SIMULATION OF STRATOCUMULUS CLOUDS

Von der Fakultät für Maschinenbau, Elektro- und Energiesysteme der Brandenburgischen Technischen Universität Cottbus-Senftenberg zur Erlangung des akademischen Grades eines

Doktors der Ingenieurwissenschaften

genehmigte Dissertation vorgelegt von

Diplom-Ingenieur
Eckhard Kadasch, geb. Dietze

geboren am 6. Juni 1983 in Dresden, Deutschland

Vorsitzender:	Prof. Dr.-Ing. Arnold Kühhorn	BTU Cottbus-Senftenberg
Gutachter:	Prof. Dr.-Ing. Heiko Schmidt	BTU Cottbus-Senftenberg
Gutachter:	Prof. Dr.-Ing. Rupert Klein	FU Berlin

Tag der mündlichen Prüfung: 1. Juli 2016

Dipl.-Ing. Eckhard Kadasch:
Controlling entrainment in large-eddy simulation of stratocumulus clouds

SUPERVISORS:
Prof. Dr.-Ing. Heiko Schmidt
Prof. Dr. Bjorn Stevens
Dr. Juan Pedro Mellado

REVIEWERS:
Prof. Dr.-Ing. Heiko Schmidt
Prof. Dr.-Ing. Rupert Klein

LOCATION:
Cottbus, Germany

DATE:
July 2016

ABSTRACT

A front-tracking algorithm for large-eddy simulation (LES) is developed to untangle the numerical and physical contributions to entrainment in stratocumulus-topped boundary layers. The front-tracking algorithm is based on the level set method. Instead of resolving the cloud-top inversion, it is represented as a discontinuous interface separating the boundary layer from the free atmosphere. The location of the interface is represented as an isosurface of an evolving marker function the evolution of which is governed by an additional transport equation. The algorithm has been implemented in an existing LES code based on the anelastic approximation of the Navier-Stokes equations.

The original LES algorithm is verified against direct-numerical simulation (DNS) data of an idealized two-dimensional cloud-top mixing layer. For this, the subgrid-scale model of the LES code was replaced by a constant molecular viscosity in order to focus on numerical errors only. A grid convergence study confirmed the anticipated global second-order rate of convergence and the convergence to the DNS solution. The slower convergence of the LES code as compared to the higher-order DNS yielded leading-order errors in the mixing layer growth at the coarsest resolutions, which were finer still than typical LES resolutions.

The front-tracking algorithm is verified by LESs of two different convective atmospheric boundary layers: the smoke cloud, a solely radiatively driven boundary layer, and a stratocumulus-topped boundary layer based on data from the DYCOMS II field study. Specifying zero entrainment, it was shown that entrainment in LES can be controlled effectively by the front-tracking algorithm. The algorithm drastically reduces entrainment errors and reduces dependencies of the solution to numerical parameters such as the choice of flux-limiters and grid resolution.

ZUSAMMENFASSUNG

Es wird ein Fronten-Verfolgungsverfahren für Large Eddy Simulationen (LES) entwickelt mit dem Ziel, numerische Beiträge zum Entrainment in Stratocu-mulus-bedeckten atmosphärischen Grenzschichten von den physikalischen Beiträgen zu trennen. Das Fronten-Verfolgungsverfahren basiert auf der Level-Set-Methode. Dabei wird die Inversion über der Wolkenoberseite als diskontinuierliche Grenzfläche aufgefasst, die die atmosphärische Grenzschicht von der darüberliegenden freien Atmosphäre trennt. Die Position der Grenz-fläche wird dabei als eine Isofläche einer sich entwickelnden Markierungsfunktion beschrieben deren Entwicklung von einer zusätzlichen Transportgleichung bestimmt ist. Das Verfahren wurde als Erweiterung eines bestehenden und auf den anelastischen Gleichungen basierenden LES-Codes implementiert.

Das ursprüngliche LES-Verfahren wird anhand von Ergebnissen einer direkten numerischen Simulation (DNS) einer idealisierten zweidimensionalen Wolken-Mischungsschicht verifiziert. Um ausschließlich numerische Effekte zu messen, wurde dafür das Feinstrukturmodell der LES durch eine konstante molekulare Viskosität ersetzt. In einer Gitterstudie wurde die

theoretisch erwartete Konvergenz von global zweiter Ordnung sowie die Konvergenz zur DNS-Lösung nachgewiesen. Wegen der im Vergleich zur DNS niedrigen Konvergenzordnung wurden auf dem gröbsten Gitter der Studie, das dennoch feiner als in typischen LESn ist, Fehler führender Ordnung in der Wachstumsrate der Mischungsschicht gemessen.

Das Fronten-Verfolgungsverfahren wird anhand von LES zweier konvektiver atmosphärischer Grenzschichten verifiziert: der sogenannten Smoke Cloud, einer ausschließlich strahlungsgetreibenen Grenzschicht, und einer Stratocumulus-bedeckten atmosphärischen Grenzschicht basierend auf Daten der DYCOMS II Messkampagne. In Simulationen mit vorgeschriebenem Null-Entrainment wurde belegt, dass das Fronten-Verfolgungsverfahren Entrainment in LESn effektiv kontrollieren kann. Das Verfahren reduziert Entrainment-Fehler drastisch und mildert Abhängigkeiten der Lösung von numerischen Parametern wie der Wahl des Flusslimiters und der Gitterauflösung.

PUBLICATIONS

Some ideas and figures have appeared previously in the following publications:

Dietze, E., Mellado, J. P., Stevens, B., & Schmidt, H. (2013). Study of low-order numerical effects in the two-dimensional cloud-top mixing layer. *Theoretical and Computational Fluid Dynamics*, 27(3-4), pp. 239-251. Springer Berlin / Heidelberg. doi:10.1007/s00162-012-0263-0

Dietze, E., Schmidt, H., Stevens, B., & Mellado, J. P. (2015). Controlling entrainment in the smoke cloud using level set-based front tracking. *Meteorologische Zeitschrift*, 23(6), pp. 661-674. Schweizerbart'sche Verlagsbuchhandlung Stuttgart. doi:10.1127/metz/2014/0595

The code that was developed as part of this thesis can be found on GitHub:

- https://github.com/uclales/uclales/tree/level-set-smoke-cloud and
- https://github.com/uclales/uclales/tree/level-set-stbl .

ACKNOWLEDGMENTS

This dissertation was done as part of my work as research assistant at the chair of numerical flow and gas dynamics at Brandenburg University of Technology Cottbus-Senftenberg in collaboration with the Max-Planck Institute for Meteorology in Hamburg. I owe my thanks to many people at both institutions.

First, I want to thank Prof. Dr.-Ing. Heiko Schmidt for giving me the opportunity to embark on this project. From him I not only learned to adhere to first principles and critically question my assumptions but also the strength of arguments by which to convince others. I am grateful for his guidance and encouragement, and for the confidence he has shown me.

This work would not have been possible without the additional support of Prof. Dr. Bjorn Stevens and Dr. Juan Pedro Mellado. To both I am grateful for their patience in answering my questions and for their constructive feedback of my work. I benefitted greatly from our discussions on clouds, thermodynamics, and numerics. While often demanding, our discussions left me with great inspiration and motivation.

My colleagues at both institutions contributed to the success of this project on one level or another. With Suvarchal Kumar, I not only enjoyed hours of discussions about low clouds and meteorological terminology, he also connected me to many people at MPI who made my stays in Hamburg to be more than official meetings. I also want to acknowledge Thijs Heus and Anurag Dipankar for their valuable comments on the UCLA-LES which helped me navigate the code.

My work at BTU Cottbus would not have been the same without my colleagues Falko Meiselbach, Christoph Glawe, Zoltan Jozefik, and Mark Simon Schöps with whom I shared many fruitful discussions on numerics and statistics, heap and stack, finance, helicopter precision landings, and sport. Silke Kaschwich assisted in all organizational matters and her insight in university bureaucracy amazes me. Andreas Stöckert and Andreas Krebs always had open ears for my questions on IT and Linux administration.

I want to thank my parents who gave me the freedom to pursue my own interests and who supported me despite my (ongoing) ignorance of gardening work and despite my early (and now faded) reluctance to eat vegetables. Finally, the greatest thanks are due for my partner Frauke whose continuous support kept me going in difficult times and whose critical questions provided me with an invaluable outside perspective.

Funding for this work was provided by the German Research Foundation (DFG) within Priority Programme SPP 1276 MetStröm (Projects ME 3833/1-3, SCHM 1682/4-3, and STE 1785/1-3). Computational resources for the studies presented in Chapters 4 and 6 were provided by German Climate Computing Center (DKRZ) in Hamburg and the North-German Supercomputing Alliance (HLRN) in Berlin (Project "Level set-based front tracking for large-eddy simulation of stratocumulus and smoke clouds"), respectively.

CONTENTS

LIST OF FIGURES

LIST OF TABLES

ACRONYMS

BL	boundary layer
CBL	convective boundary layer
CPU	central processing unit
CTI	cloud-top interface
CTEI	cloud-top entrainment instability
CV	control volume
CFL	Courant-Friedrichs-Lewy (number)
DNS	direct numerical simulation
DYCOMS	Dynamics and Chemistry of Marine Stratocumulus (field study)
FD	finite-difference
FV	finite-volume
GCM	global climate model
HJ	Hamilton-Jacobi
LES	large-eddy simulation
LS-LES	level set LES
LSM	level set method
MC	monotonized-central (limiter)
MBL	marine boundary layer
MPI	message-passing interface
ODE	ordinary differential equation
ODT	one-dimensional turbulence
PDE	partial differential equation
PPW	points per wavelength
RF01	research flight 1 (of the DYCOMS II field study)
RK	Runge-Kutta
SC	stratocumulus
SGS	subgrid-scale
SST	sea surface temperature
STBL	stratocumulus-topped boundary layer
TKE	turbulent kinetic energy
UCLA-LES	University of California, Los Angeles Large-Eddy Simulation
VTKE	vertically integrated TKE density

Table 1: Capital Latin symbols

SYMBOL	UNIT	DESCRIPTION
C_s	$[-]$	Smagorinsky constant
$\boldsymbol{D}$	$[\mathrm{s}^{-1}]$	Resolved deformation tensor
D	$[-]$	Buoyancy reversal parameter
D	$[\mathrm{s}^{-1}]$	Subsidence
E	$[\mathrm{m\,s}^{-1}]$	Entrainment rate
E	$[\mathrm{m\,s}^{-1}]$	Local turbulent entrainment velocity
G		Godunov Hamiltonian (function)
Gr	$[-]$	Grashof number
H	$[\mathrm{m}]$	Boundary layer height
H	$[\mathrm{m}]$	Height of the computational domain
H		Hamiltonian (function)
H	$[-]$	Heaviside function
L_2		L2 norm
L_∞		Maximum norm
L_v	$[\mathrm{J\,kg}^{-1}\,\mathrm{K}^{-1}]$	Enthalpy of vaporization of water
N	$[\mathrm{s}^{-1}]$	Brunt-Väisälä frequency
R, R_d	$[\mathrm{J\,kg}^{-1}\,\mathrm{K}^{-1}]$	Ideal gas constant of dry air
R_v	$[\mathrm{J\,kg}^{-1}\,\mathrm{K}^{-1}]$	Ideal gas constant of water vapor
Re_t	$[-]$	Turbulent Reynolds number
S	$[-]$	Smooth sign function
T	$[\mathrm{s}]$	Period
T	$[\mathrm{K}]$	Temperature
T_1	$[\mathrm{s}]$	Mean computational time per iteration
T_2	$[-]$	Mean computational per characteristic time
T_v	$[\mathrm{K}]$	Virtual temperature

Table 2: Lower-case Latin symbols

SYMBOL	UNIT	DESCRIPTION
a	$[\mathrm{m}]$	Double wave amplitude
b	$[\mathrm{m^2\,s^{-1}}]$	Buoyancy
b_1	$[\mathrm{m^2\,s^{-1}}]$	Maximum buoyancy
c	$[\mathrm{m\,s^{-1}}]$	Speed of sound
c_p	$[\mathrm{J\,kg^{-1}\,K^{-1}}] = [\mathrm{m^2\,s^{-2}\,K^{-2}}]$	Isobaric specific heat of dry air
g	$[\mathrm{m\,s^{-2}}]$	Gravitational acceleration
h	$[\mathrm{m}]$	Height
h	$[\mathrm{J\,kg^{-1}}] = [\mathrm{m^2\,s^{-2}}]$	Specific enthalpy
h	$[\mathrm{m}]$	Reference grid spacing
h_b	$[\mathrm{m}]$	Downdraught penetration length
h_t	$[\mathrm{m}]$	Perturbation thickness of the inversion
$\boldsymbol{k}$	$[-]$	Vertical Cartesian unit vector
l	$[\mathrm{m}]$	Eddy length scale
m	$[\mathrm{kg}]$	Mass
$\boldsymbol{n}$	$[-]$	Interface unit normal vector
p	$[\mathrm{Pa}] = [\mathrm{kg\,m^{-1}\,s^{-2}}]$	Pressure
p	$[-]$	Order of convergence
q	$[\mathrm{J\,kg^{-1}}] = [\mathrm{m^2\,s^{-2}}]$	Specific heat
q	$[\mathrm{kg\,kg^{-1}}] = [-]$	Mixture fraction
q_d	$[\mathrm{kg\,kg^{-1}}]$	Dry air mixture fraction
q_l	$[\mathrm{kg\,kg^{-1}}]$	Liquid water mixture fraction
q_t	$[\mathrm{kg\,kg^{-1}}]$	Total water mixture fraction
q_v	$[\mathrm{kg\,kg^{-1}}]$	Water vapor mixture fraction
r	$[\mathrm{kg\,kg^{-1}}]$	Mixing ratio
r_l	$[\mathrm{kg\,kg^{-1}}]$	Liquid water mixing ratio
r_t	$[\mathrm{kg\,kg^{-1}}]$	Total water mixing ratio
r_v	$[\mathrm{kg\,kg^{-1}}]$	Water vapor mixing ratio
t	$[\mathrm{s}]$	Time
u	$[\mathrm{J\,kg^{-1}}] = [\mathrm{m^2\,s^{-2}}]$	Internal energy
u, v, w	$[\mathrm{m\,s^{-1}}]$	Velocity in x, y, and z
$\boldsymbol{v}$	$[\mathrm{m\,s^{-1}}]$	Flow velocity vector
w_e	$[\mathrm{m\,s^{-1}}]$	Entrainment velocity
x, y, z	$[\mathrm{m}]$	Cartesian coordinates

Table 3: Greek symbols

SYMBOL	UNIT	DESCRIPTION
Θ_0	[K]	Reference temperature
Φ		Arbitrary scalar, discrete
Ω	$[\mathrm{rad\,s^{-1}}]$	Earth's stellar angular velocity
Ω_+	$[-]$	Subdomain where the level set function $\phi > 0$
Ω_0	$[-]$	Subdomain where the level set function $\phi = 0$
Ω_-	$[-]$	Subdomain where the level set function $\phi < 0$
Ω_x	[m]	Computational domain extent in x direction
Ω_z	[m]	Computational domain extent in z direction
α	$[-]$	Cell volume fraction
β	$[-]$	Cell face fraction
$\boldsymbol{\gamma}$	[]	Turbulent scalar flux vector
γ	$[-]$	Isentropic exponent
δ	[m]	Width parameter for error function profiles
δ_s	$[-]$	Smoothing parameter for buoyancy mixing function
ϵ	$[-]$	Small number, $\epsilon \ll 1$
θ	[K]	Potential temperature
θ_l	[K]	Liquid water potential temperature
θ_v	[K]	Virtual potential temperature
$\kappa = R/c_p$	$[-]$	Poisson constant
κ	$[-]$	von Kármán constant
λ	[m]	Wave length
π	$[-]$	Exner pressure function
ρ	$[\mathrm{kg\,m^{-3}}]$	Density
$\boldsymbol{\tau}$	$[\mathrm{m^2\,s^{-2}}]$	Tensor of turbulent momentum fluxes
τ	[s]	Time constant, artificial time
ν	$[\mathrm{m^2\,s^{-1}}]$	Kinematic viscosity (of the mixture)
ϕ	[], [rad]	Latitude
ϕ	[m]	Level set function
φ		Arbitrary scalar, continuous
χ	$[-]$	Normalized mixture fraction

1 INTRODUCTION

1.1 MOTIVATION

Clouds amaze us with a multitude of different forms and sizes, with different colours and densities, and life spans from minutes to weeks. Despite their obvious dissimilarities, all cloud types share some key aspects which warrants the unifying term 'cloud'. The International Cloud Atlas [3] by the World Meteorological Organization defines a cloud in the following way:

> "A cloud is a hydrometeor consisting of minute particles of liquid water or ice, or of both, suspended in the free air and usually not touching the ground. It may also include larger particles of liquid water or ice as well as non-aqueous liquid or solid particles such as those present in fumes, smoke or dust."

The term 'hydrometeor' refers to a kind of observable phenomena in the atmosphere, specifically one consisting of an ensemble of liquid or solid water particles. Other definitions of clouds exist (see for instance the glossaries of the National Oceanic and Atmospheric Administration's National Weather Service [2] and the American Meteorological Society [1]) but many of them, as does the one above, involve three defining characteristics:

1. Clouds are visible. This is in contrast to the Earth's atmosphere in which they exist, which is largely translucent. Their visibility emphasises the fact that clouds interact with radiation and hints on their importance for the Earth's energy balance. Furthermore, observations show their wide range of life spans and physical extents, sometimes approaching the planetary scale.

2. Clouds comprise of tiny particles. This hints on the importance of small-scale processes relevant for forming those particles as well as for transporting them in the atmosphere. In combination with the first characteristic, this reveals the wide spectrum of scales on which processes may contribute to the evolution of clouds.

3. The cloud particles are made of water, either in liquid or solid form. Thus, cloud formation and evolution depends on the ways by which water is absorbed by the atmosphere and distributed within it.

It is remarkable that the challenges faced with simulating cloudy systems and their relevance to our climate have their roots in these basic characteristics and their associated physical processes. In fact, Bony and Dufresne [7] show that some cloud types are the dominant source of errors in global climate models (GCMs). Stevens and Bony [73] conclude in their brief review–*What are climate models missing?*–that "[t]here is now ample evidence that an inadequate representation of clouds and moist convection, or more generally the coupling between atmospheric water and circulation, is the main limitation in current representations of the climate system".

With the realization of global warming, the question about how sensitive our climate is to the emission of green house gases has been raised. An important metric to approach an answer is the *equilibrium climate sensitivity*,

i.e. the steady-state change in the annual global mean surface temperature associated with a doubling in CO_2 in the atmosphere [53, 73]. Unfortunately, model intercomparisons exhibit a large spread among different GCMs. Numerical experiments of an aquaplanet by Medeiros et al. [38] show that the climate sensitivity is comparable to that observed in Earth-like control simulations. In fact, the differences between the two GCM models used are greater than differences between the Earth-like and the aquaplanet scenarios. Both results suggest that improving the accuracy of the global water cycle is key to reducing uncertainties in estimations of climate sensitivity and that other effects not included in the aquaplanet might be secondary. In other words, current GCMs don't lack complexity, but the processes that are included, are not simulated accurately enough.

Investigating the origin of the uncertainties in the Earth system, Bony and Dufresne [7] identify marine boundary layer (MBL) clouds, which are poorly resolved by currently customary GCM meshes, as one of the primary sources for uncertainties of model-based estimates of the equilibrium climate sensitivity. They conclude that the representation of MBL processes must be improved in order to reduce cloud-related uncertainties.

One approach to better represent such cloud systems in climate projections is to carry out small-scale numerical studies of specific cloud types and derive improved parameterizations for GCMs. Large-eddy simulation (LES) has been used extensively as a tool for such small scale studies, but our ability to simulate shallow clouds accurately are still limited by available computer power due to the shear range of important temporal and spatial scales. Important quantities, such as cloud cover and albedo are still sensitive to the parameterization of unresolved small-scale processes or details in the numerical methods (see for instance [79]). On the other hand, direct numerical simulation (DNS), resolving the flow down to the Kolmogorov (dissipation) scales have been used to understand in detail the instabilities and turbulent-laminar mixing at the top of stratiform clouds [10, 40, 43, 46]. Unfortunately, such studies remain limited to relatively small region around the cloud top and are currently not able to simulate an entire boundary layer (BL) and, thus, miss feedbacks from turbulent surface interactions. However, the three approaches—DNSs, large-eddy simulations (LESs), and GCMs—can be used to complement each other.

This thesis is dedicated to the improvement of LESs of stratocumulus clouds as an important archetype of MBL clouds. By (i) eliminating one of the major sources of numerical errors in LESs and (ii) providing an interface for small-scale parameterizations based on DNS studies, the present work supplies a part in this complementary hierarchy. The next section discusses in more detail the climatological relevance and spatial structure of stratocumulus clouds, describe the challenges of simulating them accurately using LES, and introduce the methodology based on the level set method that is used here to remove numerical errors. The proposed methodology is implemented in the University of California, Los Angeles Large-Eddy Simulation (UCLA-LES), a flow solver, that has been successfully used to simulate and study a variety of relevant atmospheric flows [4, 5, 36, 58, 74, 75, 79, 86].

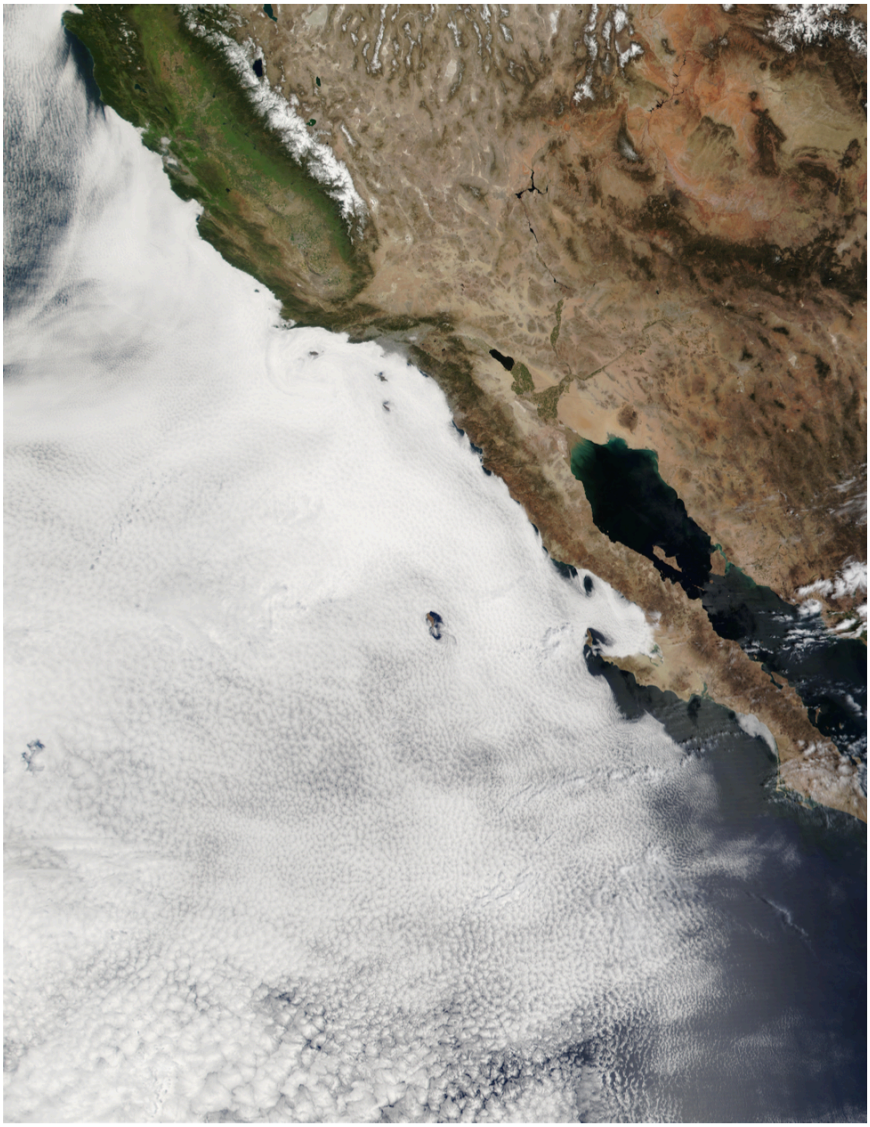

Figure 1: Satellite image of a stratocumulus cloud field off the coast of California on March 31, 2002. (Image by Jacques Descloitres, MODIS Land Rapid Response Team, NASA/GSFC [14])

1.2 STRATOCUMULUS CLOUDS

Stratocumulus clouds often form closed decks with high albedo reflecting much of the incoming light. Figure 1 shows an example off the west coast of California and Baja California extending over more than 1000 km in both longitude and latitude. As shown in Fig. 2, stratocumulus clouds can occur almost anywhere on Earth but are most frequently found over the subtropical eastern oceans where their annual mean coverage exceeds 40% [89]. In the annual mean, about one fifth of Earth's surface is covered by stratocumulus making it the dominant cloud type by area covered [89]. As a result, stratocumulus clouds significantly affect Earth's radiative energy balance exerting a net cooling effect on the Atmosphere.

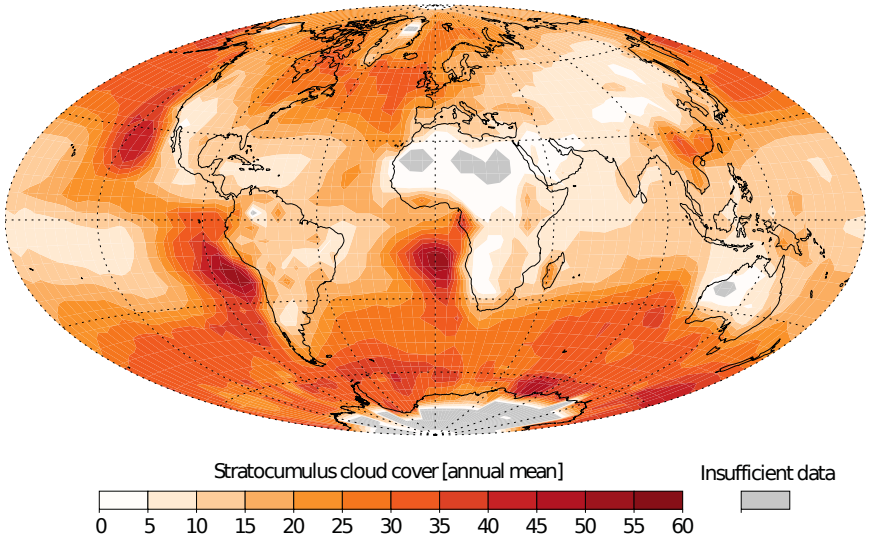

Figure 2: Annual mean of global stratocumulus cloud cover in %. (Figure by Robert Wood [89], ©American Meteorological Society. Used with permission.)

The stratocumulus-topped boundary layer (STBL) consists of a layer of cool moist air which is capped by relatively warmer and drier air. The configuration is illustrated in Fig. 3. The boundary layer is well mixed due to turbulent convection and is topped by a stratocumulus cloud. The boundary layer and the free atmosphere above are separated by a strongly stratified inversion layer. The thickness of this inversion layer is measured in metres over which the temperature gradient can be positive (keeping in mind the temperature gradient for neutral stratification is -10 K km^{-1}) giving rise to the terminology inversion layer, as the temperature gradient is inverted relative to the tropospheric norm. The convection in the boundary layer is driven from the cloud top, mainly by radiative cooling and evaporative cooling. Shear due to large-scale boundary layer vortices may further enhance turbulent mixing at the cloud top.

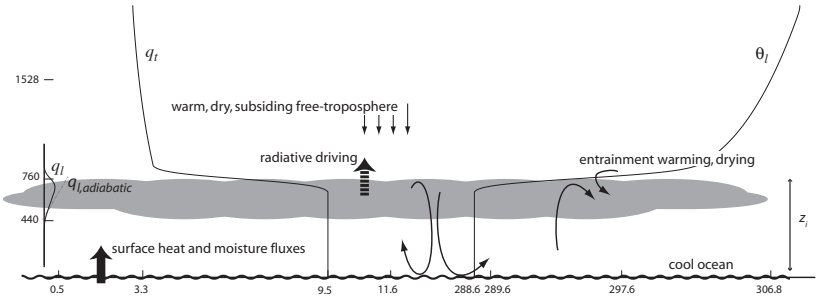

Figure 3: Sketch of mean thermodynamics structure of lower troposphere, for July 2001, near 120W 30N. The potential temperature, specific humidity and height at 850 hPa are indicated, as are values within and just above the STBL. (Sketch by Bjorn Stevens et al. [80], ©American Meteorological Society. Used with permission.)

While radiative cooling acts on the scale of tens of meters, see e.g. the radiative flux profiles in Bretherton at al.'s [8] simulations, evaporative cooling occurs at the molecular scale which can be on the order of millime-

tres[1] [40, 46]. Evaporative cooling can even lead to *buoyancy reversal* [68, 90], where in mixing relatively warmer and drier air into the inversion layer, heavier mixtures can develop if evaporative cooling dominates entrainment warming. Chapter 4 explores this effect in detail in an idealized case, where convection is driven solely by evaporative cooling.

Already the mixed-layer theory by Lilly [32] identified entrainment, associated with turbulent mixing across the cloud-top inversion, as an important determinant for the evolution of the cloud. Entrainment can be thought of as a process with two steps, both of which occur simultaneously in reality: While mixing at the cloud top tends to blur the inversion, turbulent mixing below homogenizes the BL and tends to steepen the cloud-top gradients. As a result, air from the free atmosphere is mixed into the BL gradually warming and drying it and its depth slowly increases over time. This process is typically described by a bulk entrainment velocity or rate, e.g. if $H(t)$ is the average inversion height of the STBL,

$$w_e = \frac{dH}{dt} \quad . \tag{1.1}$$

The entrainment rate is typically countered by an inflow of warm tropical air subsiding from the Hadley circulation [72].

1.3 LARGE-EDDY SIMULATION OF STRATOCUMULUS CLOUDS

LES has been used extensively to improve understanding of the dynamics of the STBL. The fidelity of LES has increased tremendously over the last decades. Spatial resolution increased from 50 m in the early studies, such as the one by Deardorff [13], to 5 m and less in recent LES [48, 79, 81, 91]. However, important quantities such as entrainment remain dependent on the grid resolution and grid spacing aspect ratio, even in recent high-resolution LES with vertical resolutions of up to 2.5 m [92]. Unfortunately, GCMs and even LES currently have, and in the foreseeable future will have, insufficient grid resolution to resolve the cloud top and the small-scale mixing processes. Even at the relatively high resolution characteristics of present studies, the evolution of stratocumulus remains sensitive to the parameterization of subgrid-scale (SGS) processes, or the numerical representation thereof. In some cases, there are order one errors in important properties of simulated stratocumulus such as the entrainment rate. By making an effort to limit mixing, for instance by switching the SGS terms off and using numerical errors as a closure model, the results improve in some cases [72] but for unphysical reasons. This is unsatisfactory, since the "good" comparison depends among other on the grid size and the order of the numerical method. This suggests that (i) SGS processes play a significant role in the evolution of the cloud, and that (ii) numerical errors are of leading order, thus making it hard to distinguish between numerical and physical effects.

The reasons for the difficulty of simulating the STBL with high accuracy using LES are both physical and numerical. The physical aspect is that small-scale mixing processes are not explicitly simulated but typically parameterized using standard closures the underlying assumptions of which are not satisfied at the cloud top. Mellado et al. [45] showed that probability density functions of velocity in the turbulent region show a strong vertical variability

1 With the radiation model used in Chapt. 5 for the smoke cloud, the vertical radiative flux (Eq. (5.2)) decreases to 50 % of its maximum at a depth of 35 m from the cloud top. In DNS of buoyancy reversal [40, 46], the dissipation scale was about 3 mm.

and often non-Gaussian behaviour, even in the horizontal component. This indicates strong anisotropy and inhomogeneity of the turbulence which, in addition to the relevance of molecular transport, further complicates turbulence modelling in LES for this kind of flows.

The numerical aspect is that the steep gradients of total water content and temperature in the inversion layer are insufficiently resolved. As a result, important quantities such as cloud-top entrainment can develop leading-order errors (see Chapt. 4 and [15], respectively). The fact that many physical and numerical uncertainties interact makes it hard to separate their individual contributions and make the solution dependent on details in the numerics as well as in the microphysical and turbulence model (cf. Moeng et al. [47]).

Several idealizations have been made in order to help understand individual parts of the entrainment problem. Most notably is the separation of evaporative and radiative cooling, based on which numerical and experimental studies have been carried out. Already in 1968, Lilly [32] introduced a simplified model of the STBL, the smoke cloud. It is similar to the STBL in that the convective boundary layer (CBL) is driven by radiative cooling. It is simpler than the STBL in that it is dry and, thus, avoids evaporative feedback on entrainment. Instead of water, in the form of vapour or droplets, it contains radiatively active smoke. This simplification has two main advantages. First, it makes the boundary layer problem accessible to experiments. McEwan and Paltridge [37] as well as Sayler and Breidenthal [59] conducted tank experiments, the latter of which was also numerically reproduced by Schmidt et al. [62] using a 1D stochastic model. Secondly, it allows more direct investigation of the uncertainty associated with differences in the numerical methods used in LES. Bretherton et al. [8] carried out LES of the smoke cloud comparing various LES codes. Because they specified the radiation using the identical dependence on the smoke concentration, they could attribute differences among the various codes to differences in the numerical algorithms and the choice of subgrid-scale models. Small-scale studies are also possible. DeLozar and Mellado [10] carried out DNS of the smoke cloud-top interface. Similarly, high-resolution methods, which allow for a representation of molecular effects, have been used to explore the entrainment mechanism under buoyancy reversal. Examples include, one-dimensional stochastic models such as the linear eddy model [28] and the one-dimensional turbulence model [90] but also DNSs without [42, 43, 40] and with additional shear [46] based on the Boussinesq approximation and a continuous two-fluid formulation [44]. Unfortunately, the link to the large-scale boundary-layer motions in DNS remains difficult.

In summary, no simulation strategy alone is currently able to simulate all important details of the STBL accurately enough. The reasons are connected to the fundamental characteristics of stratocumulus (SC) clouds mentioned initially in Sect. 1.1 and the central one being the broad range of temporal and spatial scales present in the STBL. But different simulation strategies can be used to complement each other and this thesis presents one approach of doing so, that enables to combine high-resolution methods or derived parameterizations based on them, with LES that can simulate an entire STBL. The approach is based on the level set method (LSM), which is described in the next section.

1.4 OVERVIEW OF THE LEVEL SET METHOD

Level set methods have been successfully used in many problems where evolving interfaces between discontinuous physical properties are important. Level set methods use a scalar marker field, the zero level set or isosurface of which represents the interface. The dynamics of the interface are described by the Hamilton-Jacobi-type level set equation. The concept was formally introduced by Osher and Sethian [52] and since then many methods for a variety of problems have been developed based on the idea. These include multiphase flows [84, 82, 83], combustion modelling [21, 60, 63, 69], as well as image processing and computer vision [27]. The idea to represent interfaces using level sets is equivalent to the G equation concept coined by Markstein [35] which is frequently used in the combustion literature. Level set methods add to this idea mathematical theory and analysis of suitable numerical algorithms [52, 51]. Overviews of level set methods and the spectrum of their applications can be found in the reviews by Osher and Fedkiw [51] and by Sethian and Smereka [65] as well as in the books by the same authors [50, 64].

In this thesis, the level set method is used to represent the cloud-top boundary as a discontinuity on the LES grid instead of trying to resolve it. By supplying internal boundary conditions on both sides using the ghost fluid method [18], discretization over the discontinuity is avoided. The main goal is to untangle the numerical and physical contributions to entrainment, by eliminating the numerical problem mentioned above. In a similar effort to improve the representation of cloud boundaries and to reduce numerical errors in their vicinity, e.g. Margolin et al. [34] and Kao et al. [25] have used the volume-of-fluid method. The main advantage of the level set method is, however, that there is no substantial logic required in order to reconstruct the topology of the interface. Rather, it is given directly by the isosurface of the associated level set scalar.

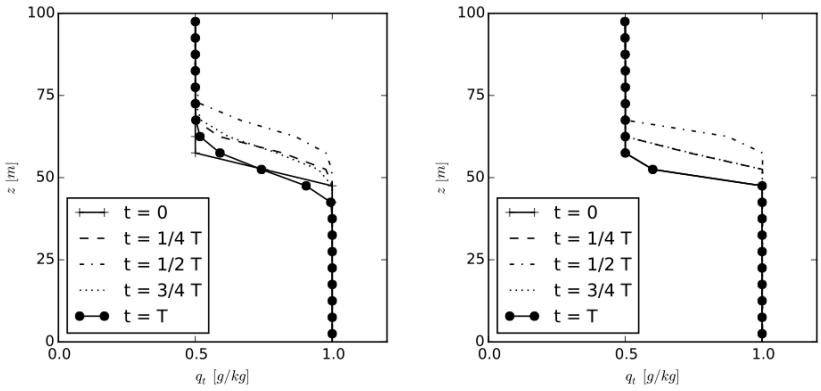

Figure 4: Advection of an initially discontinuous profile of total water content without (left) and with the level set method (right) using a standard, globally second-order finite-volume advection scheme. The uniform vertical motion was prescribed as in Eq. (1.2).

Figure 4 shows the results of a numerical experiment illustrating the usefulness of the level set method. Profiles of an initially discontinuous distri-

bution of the total water content q_t are shown at various stages during one period T of the uniform vertical motion

$$w(t) = \sin(2\pi t/T) \quad . \tag{1.2}$$

The left panel shows the profiles obtained using the globally second-order finite-volume advection scheme using the monotonized-central flux limiter, as presented in Sect. 3.2.2. No other effects are present, especially no molecular or turbulent diffusion and a typical high LES resolution of 5 m is used. After one period of oscillation, the jump in q_t has visibly spread over two more grid cells. The right panel shows the same experiment using in addition the level set method. Here, the profile after one oscillation matches the initial one as expected from the exact solution.

The behaviour of the standard method on the left panel is well known, see for instance LeVeque's textbook [31], but is problematic for simulating the STBL. The blurring of the moisture profile artificially enhances mixing and, thus, entrainment of the BL. This can dramatically alter global properties of the cloud such as cloud cover and albedo, especially considering that small changes in the total water content can yield large changes of the condensed part.

2 MATHEMATICAL MODEL

This chapter discusses the governing equations for the stratocumulus-topped boundary layer (STBL) problem. It is divided into two parts. The first part, Sect. 2.1, is concerned with the equations of motion and the thermodynamic considerations that together describe the fluid mechanics. After that, Sect. 2.2 presents the model equations based on the level set method which are used to model the cloud-top interface as discontinuity embedded in the flow. The division between fluid mechanical equations and interface model equations also highlights the contribution of this thesis to the University of California, Los Angeles Large-Eddy Simulation (UCLA-LES) code: The first part describes the equations that underly the standard UCLA-LES solver and forms the starting point for the present work; the second part reflects the contribution of this thesis to the standard UCLA-LES.

The numerical methods employed to solve the equations are discussed in the next chapter—in Sects. 3.2 and 3.3—following the same division.

2.1 EQUATIONS OF MOTION

Atmospheric flows are multi-component and multi-phase turbulent flows. In most cases, the greatest constituent is dry air: a mixture of 78.110 vol. % Nitrogen, 20.953 vol. % Oxygen, and 0.934 vol. % Argon [17]. Other substances may be suspended or resolved, the most important of which is water, which can be either solid, liquid, or gaseous. Other substances of mineral, biological, or industrial origin may also be present. Here, dust and sea salt particles are notable because when suspended in the atmosphere, they form condensation nuclei for water vapour. The presence of such particles in the atmosphere is of crucial importance for the formation of fog, clouds, and rain. In the scope of this work, only mixtures of dry air and water in its liquid and gaseous state are considered. Water ice and other particles are neglected.

As discussed in the introduction, clouds are a suspension of water droplets in the atmosphere. On the microscopic scale, this can be regarded as a continuous multi-component flow where density and species concentration change continuously across the surfaces of droplets. On a larger scale, cloud droplets may be regarded as particles embedded in the otherwise gaseous flow. On a yet larger scale, where many of such particles exist in a given control volume, they may be approximated as a continuous mass fraction. Opposed to the first view, this concentration would not show individual droplets anymore. Information about size distribution and droplet density is then lost and, if important for the respective application, would have to be modelled. The two-component suspension of liquid water droplets in a dry-air/vapour mixture is then represented by a mixture of two continuous fluids.

In this work, the fluid is described using such a two-fluid formulation. The main underlying hypotheses are the following. (i) The liquid water can be considered a continuous phase, (ii) the mixture always stays in local thermodynamic equilibrium, and (iii) the diffusivity of the liquid phase equals that of dry air and water vapour. Mellado et al. [40] discuss the validity and

the implications of these assumptions. They show that the simplifications (i-iii) are not satisfied in reality but provide a reasonable approximation to study latent heat effects.

The composition of an air parcel is typically characterized by *mixing ratios* which are denoted q_x. Here, the subscript x represents any of the contributions: dry air (d), water vapour (v), liquid water (l), or total water (t). Here, mixing ratios are defined such that they relate the mass of a component, m_x, in an air parcel to the total mass, m, of the parcel, i.e.

$$q_x = m_x / m \quad . \tag{2.1}$$

The total water mixing ratio q_t is also referred to as specific humidity. Sometimes, mixing ratios are referred to more loosely as total water content and water vapour content, etc. Note that, per definition, the sum of the fractions of all water phases present equals the total water content, i.e.

$$q_t = q_v + q_l \quad ,$$

and the fractions of all components present is

$$1 = q_d + q_t = q_d + q_v + q_l \quad . \tag{2.2}$$

Sometimes, mixing ratios are defined relative to the dry air mass m_d, denoted r_x. As shown in Appendix A.1, the relative error between the two mixing ratio definitions for a two-component multi-phase fluid equals the total water mixing ratio itself. Since for the cases considered here, typical q_t, and r_t for that matter, do barely exceed values of $10\,\mathrm{g/kg} = 0.01$ (c.f. [9, 78]), the difference between mixture fraction and mixing ratio is small. Since the nomenclature is sometimes used interchangeably, it should be carefully checked which of the two definitions is used, especially in cases where greater mixing ratios occur.

As Etling [17] points out, dry air behaves very much like an ideal gas. Although this is not the case for water vapour, the approximation holds for moist air in the atmospheric boundary layer because total water mixing ratios for the cases considered here are of around 1 % or less.

With these assumptions, the flow in the STBL can be described by eight unknowns. These are the three components of the velocity vector, $\boldsymbol{v} = (u, v, w)^{\mathrm{T}}$, the pressure, p, density ρ, absolute temperature, T, and the mixing ratios of total water, q_t, and either water in liquid, q_l, or vapour form, q_v. The unknowns are solved for using the conservations laws for momentum, mass, and energy. Specifically, the anelastic limit of the Navier-Stokes equations is used in conjunction with the appropriate continuity equation and a temperature equation that is based on the first law of thermodynamics. The partitioning between liquid water q_l and water vapour q_v is diagnosed from the Clausius-Clapeyron relation and Dalton's law of partial pressures and Eq. (2.2) from pressure, temperature and total water content.

The following sections present how the governing equations that are solved in the UCLA-LES are obtained. Specifically, Sect. 2.1.1 presents the relevant thermodynamic relations for the dry atmosphere leading to an evolution equation for temperature as a from of the first law of therodynamics. Then, Sects. 2.1.2 and 2.1.3 describe the anelastic approximation of the equations of motion for the dry atmosphere and their modifications for moist systems, respectively. Finally, Sect. 2.1.4 presents the LES-filtered set of equations the UCLA-LES is based on.

2.1.1 *Dry atmosphere*

The equilibrium state of a thermodynamic system at rest is defined by the thermodynamic state variables density ρ, temperature T, and pressure p. For an ideal gas, which is a reasonable approximation for air in the atmosphere [17], these variables are linked via

$$p = \rho R T \quad . \tag{2.3}$$

Here, R is the specific gas constant of the working fluid given by the difference of the isobaric and volumetric specific heats, $c_p - c_v$. (Table 14 lists typical values of these parameters for dry air under atmospheric conditions.) According to this equation of state, any two of the three variables ρ, T, and p define the state of the system.

Over the height of the well mixed STBL, pressure changes considerably due to the hydrostatic weight of the atmosphere. As a result, air parcels change temperature while they are advected through it. For such cases, it is useful to use the potential temperature

$$\theta = T \left(\frac{P}{p} \right)^{R/c_p} \tag{2.4}$$

in place of the absolute temperature T. The reference pressure P is typically taken to be 1000 hPa, which is a typical value for the pressure at the surface of the STBL. Equation (2.4) is obtained by integrating the first law of thermodynamics in enthalpy form

$$dh = c_p \, dT = dp/\rho + \delta q \tag{2.5}$$

from a reference state, θ and P, to an arbitrary end state, T and p, assuming an adiabatic process ($\delta q = 0$), see Appendix A.3. Accordingly, θ is the temperature of an air parcel that was brought adiabatically from temperature T and pressure p to reference pressure level P. This invariance of the potential temperature to adiabatic displacements is one benefit of using it. Another one is that the potential temperature translates to buoyancy in a dry atmosphere and thus indicates the convective stability. That is, regions where $\frac{\partial \theta}{\partial z} > 0$ are stably stratified and regions where $\frac{\partial \theta}{\partial z} < 0$ are unstably stratified. This can be best seen in the buoyancy Eq. (2.59). Assume a parcel is lifted in an adiabatic atmosphere where $\frac{\partial \theta}{\partial z} > 0$. The parcel will then be surrounded by air at higher potential temperature compared to which it will be less buoyant. As a result, the parcel will be accelerated back towards its original position. Thus, such an atmosphere is called stably stratified. The reverse argument can be made for the case where $\frac{\partial \theta}{\partial z} < 0$.

The inverse of the pressure term in Eq (2.4) is called the Exner function or Exner pressure

$$\pi = \left(\frac{p}{P} \right)^{R/c_p} \quad . \tag{2.6}$$

The exponent in the relations above is known as the Poisson constant $\kappa = R/c_p$ which, for dry air, approximately assumes the value 0.286 [17]. With Eq. (2.6), the potential tempereature definition Eq. (2.4) can be restated as

$$T = \theta \pi \quad , \tag{2.7}$$

such that the ideal gas law (2.3) can be restated as

$$p = \rho R \theta \pi \quad . \tag{2.8}$$

Over the height of 1 km, Exner pressure reduces by about 3.3 %. According to Eq. (2.7), this translates to a reduction of the absolute temperature of about 10 K.

An evolution equation for the potential temperature can be derived from the first law of thermodynamics (2.5). From Joule's law it follows, that the enthalpy is proportionally related to the temperature via the isobaric specific heat according to

$$dh = c_p dT \quad . \tag{2.9}$$

Then, Eq. (2.4) can be used to express the first law in terms of the potential temperature. Dividing by the time differential dt eventually gives

$$\frac{d\theta}{dt} = \frac{\theta}{c_p T}\dot{q} = \frac{\dot{q}}{c_p \pi} \quad , \tag{2.10}$$

where $\dot{q} = \delta q / dt$. This equation constitutes an alternative form of the first law of thermodynamics, restated in terms of the potential temperature and Exner pressure. Equation (2.10) expresses the rate of change of the potential temperature in a Lagrangian frame of reference. By expanding the total derivative, an equation in the Eulerian frame is obtained:

$$\frac{\partial \theta}{\partial t} + \boldsymbol{v} \cdot \nabla \theta = \frac{\dot{q}}{c_p \pi} \quad . \tag{2.11}$$

A conservative form, that is more suitable for finite-volume discretization, can be obtained by multiplying by ρ and adding θ times the continuity equation

$$\frac{\partial \rho}{\partial t} + \nabla \cdot (\rho \boldsymbol{v}) = 0 \quad . \tag{2.12}$$

The result is

$$\frac{\partial (\rho\theta)}{\partial t} + \nabla \cdot (\rho\theta \boldsymbol{v}) = \frac{\rho \dot{q}}{\pi c_p} \quad . \tag{2.13}$$

For adiabatic flows, Eq. 2.13 reduces to

$$\frac{\partial (\rho\theta)}{\partial t} + \nabla \cdot (\rho\theta \boldsymbol{v}) = 0 \quad . \tag{2.14}$$

Note that these equations neglect heat conduction, which is thought to be small compared to turbulent mixing in atmospheric flows.

2.1.2 *Anelastic approximation*

High-Reynolds-number flows, such as atmospheric flows, can be approximately described by the compressible Euler equations. The only simplification over the full Navier-Stokes equations is the omission of viscous terms which can be shown to become small for high-Reynolds-number flows. The Euler equations retain both acoustic waves as well as gravity waves. It is desirable to remove the high-frequency acoustic waves and only retain the low-frequency gravity waves, because acoustic waves barely influence atmospheric flows [17], but they pose a severe time step constraint in the numerical solution. Consider the speed of sound, c, in an ideal gas [17]

$$c = \sqrt{\gamma \frac{p}{\rho}} = \sqrt{\gamma R T} \quad . \tag{2.15}$$

For values typical at the Earth's surface, e.g. $T = 293.15K$, and air with $\gamma = \frac{c_p}{c_v} = 1.4$, c takes values of approximately 343 m/s. This is about 100 times that of what can be expected as typical convective velocities in the STBL. Thus, the time step size could be increased by a factor of about 100, if acoustic waves could be filtered out from the system of equations. Ogura and Phillips's anelastic equations [49] provide such a filtered set.

Ogura and Phillips [49] start their asymptotic analysis with a compressible set of equations closely related to the Euler equations. The differences to the Euler equations are the use of the first law of thermodynamics instead of the total energy equation and the use of potential temperature and Exner pressure instead of their thermodynamic equivalents. In the following it is illustrated how this set can be obtained.

Atmospheric flows can be described by the equation of motion in the advective form

$$\frac{\partial \boldsymbol{v}}{\partial t} + \boldsymbol{v} \cdot \nabla \boldsymbol{v} = -\frac{1}{\rho} \nabla p - g\boldsymbol{k} \quad , \tag{2.16}$$

the first law of thermodynamics in the form of the temperature equation

$$\frac{\partial \theta}{\partial t} + \boldsymbol{v} \cdot \nabla \theta = 0 \quad , \tag{2.17}$$

and the continuity Eq. (2.12)

$$\frac{\partial \rho}{\partial t} + \nabla \cdot (\rho \boldsymbol{v}) = 0 \quad .$$

Note that this set of equations describes the dry and adiabatic atmosphere. Diabatic effects due to radiation and heat conduction, and latent heat effects due to condensation and evaporation can be added. The equations can be stated more concisely in the Lagrangian form

$$\frac{d\boldsymbol{v}}{dt} = -\frac{1}{\rho} \nabla p - g\boldsymbol{k} \quad , \tag{2.18}$$

$$\frac{d\theta}{dt} = 0 \quad , \tag{2.19}$$

$$\frac{1}{\rho} \frac{d\rho}{dt} = -\nabla \cdot \boldsymbol{v} \quad , \tag{2.20}$$

by using the material derivative $d/dt = \frac{\partial()}{\partial t} + \boldsymbol{v} \cdot \nabla()$. The set of equations involves as the six unknowns the three components of the Cartesian velocity vector $\boldsymbol{v}$, the pressure p, the density ρ and the potential temperature θ. Furthermore, $\boldsymbol{g}$ denotes the gravitational acceleration and $\boldsymbol{k}$ is the vertical unit vector. The set of equations is completed by the ideal gas law (2.3). As shown in Appendix A.6, the pressure term in the momentum equation (2.18) can be restated using the Exner function (2.6) as

$$\frac{1}{\rho} \nabla p = c_p \theta \, \nabla \pi \quad . \tag{2.21}$$

As a result, the momentum Eq. (2.18) becomes

$$\frac{d\boldsymbol{v}}{dt} = -c_p \theta \, \nabla \pi - g\boldsymbol{k} \quad . \tag{2.22}$$

Ogura and Phillips [49] formulate the continuity equation in terms of θ and π as

$$\frac{d}{dt} \left(\ln \theta + \left(1 - \frac{1}{\kappa} \right) \ln \pi \right) = \nabla \cdot \boldsymbol{v} \tag{2.23}$$

which has the advantage that ρ is not needed as an additional variable. Equation (2.23) is obtained form logarithmic differentiation of the ideal gas law (shown in Appendix A.7). Here, however the density form, Eq. (2.20), is used for conciseness.

In order to cary out the asymptotic analysis, the set of equations, Eq. (2.22), (2.19), and (2.20), has to be non-dimensionalized. For this, Ogura and Phillips [49] introduce a (yet arbitrary) reference time τ and temperature Θ_0 scale, and a reference length H given here by the boundary layer (BL) height. Using these and the reference pressure P, the physical variables and operators can be replaced by

$$\nabla = \nabla^* / H \quad , \qquad \frac{\partial}{\partial t} = \frac{\partial}{\partial t^*} / \tau \quad ,$$
$$\boldsymbol{v} = \boldsymbol{v}^* \frac{H}{\tau} \quad , \qquad \theta = \theta^* \Theta_0 \quad , \qquad \rho = \rho^* \frac{P}{R\Theta_0} \quad ,$$

where the asterisks (*) denote non-dimensional symbols. After collecting the factors, the equations become

$$\frac{H^2}{\tau^2 c_p \Theta_0} \frac{d\boldsymbol{v}^*}{dt^*} = -\theta^* \nabla^* \pi - \frac{gH}{c_p \Theta_0} \boldsymbol{k} \quad , \tag{2.24}$$

$$\frac{d\theta^*}{dt^*} = 0 \quad , \tag{2.25}$$

$$-\frac{1}{\rho^*} \frac{d\rho^*}{dt^*} = \nabla^* \cdot \boldsymbol{v}^* \quad . \tag{2.26}$$

For their asymptotic approximation, Ogura and Phillips [49] make two assumptions. The first is, that the potential temperature varies only slightly around the reference temperature Θ_0, i.e. $\theta^* \approx 1$ and $\epsilon = \frac{\Delta\theta}{\Theta_0}$ is a small number. The second one involves the relevant time scale τ: The Euler equations include both acoustic waves as well as gravity waves. As discussed before, it is desirable to remove the high-frequency acoustic waves and only retain the low-frequency gravity waves. Thus, the relevant time scale τ is that of oscillations governed by buoyancy differences which corresponds to the Brunt-Väisälä frequency N given by

$$N = \sqrt{\frac{g}{\theta} \frac{\partial \theta}{\partial z}} \quad . \tag{2.27}$$

The corresponding oscillation time scales as

$$\tau = 1/N = \sqrt{H/\epsilon g} \quad . \tag{2.28}$$

With this choice, the smallness parameter ϵ enters the momentum equation (2.24) which becomes

$$\epsilon\beta \frac{d\boldsymbol{v}^*}{dt^*} = -\theta^* \nabla^* \pi - \beta \boldsymbol{k} \tag{2.29}$$

using the dimensionless parameter

$$\beta = \frac{gH}{c_p \Theta_0} \quad . \tag{2.30}$$

The other equations remain unchanged.

If ϵ is indeed a small number, it reasonable to assume scale separation, i.e. processes occuring at a certain scale result in changes close to that scale.

In other words, terms of order $\epsilon^0 = 1$ mostly interact with each other, and the interaction with terms of a different order can be neglected. In order to reveal that separation, the prognostic variables are expanded in a power series of ϵ:

$$\begin{aligned} \boldsymbol{v}^* &= \boldsymbol{v}_0^* + \epsilon \boldsymbol{v}_1^* + \epsilon^2 \boldsymbol{v}_2^* + \cdots \\ \pi &= \pi_0 + \epsilon \pi_1 + \epsilon^2 \pi_2 + \cdots \\ \rho^* &= \rho_0 + \epsilon \rho_1^* + \epsilon^2 \rho_2^* + \cdots \\ \theta^* &= 1 + \epsilon \theta_1^* + \epsilon^2 \theta_2^* + \cdots \quad . \end{aligned} \tag{2.31}$$

Note that $\theta_0^* = 1$ (and, thus, $\theta_0 = \Theta_0$) in this expansion, which reflects the assumption of small variations of the potential temperature around the mean. After replacing the prognostic variables in the non-dimensional set of equations, they can be split into individual equations for each scale ϵ^0, ϵ^1, and so forth.

Collecting all ϵ^0 terms in the momentum Eq. (2.29) gives

$$\epsilon^0 : \quad \nabla^* \pi_0 = -\beta \boldsymbol{k} \quad . \tag{2.32}$$

As a result, π_0 is constant along x and y and varies only with height z. Integrating Eq. (2.32) from the surface to an arbitrary (non-dimensional) height z^* gives the solution of the pressure as

$$\pi_0(z^*, t^*) = \pi(0, t^*) - \beta z^* = \pi_{00}(t^*) - \beta z^* \quad ,$$

where $\pi_{00}(t^*) = \pi_0(z^* = 0, t^*)$. This is the pressure profile of a hydrostatic atmosphere at rest, and at constant and uniform potential temperature Θ_0. The density in such an atmosphere is obtained from the ideal gas law, Eq. (2.3), as

$$\rho_0^*(z^*, t^*) = \pi_0^{(1/\kappa)-1} = (\pi_{00}(t^*) - \beta z^*)^{(1/\kappa)-1} \quad . \tag{2.33}$$

The equation of the ϵ^0 terms of the continuity Eq. (2.26) gives

$$\frac{\partial \rho_0^*}{\partial t^*} + \nabla^* \cdot (\rho_0^* \boldsymbol{v}_0^*) = 0 \tag{2.34}$$

It can be shown, that with appropriate boundary conditions, the time integral in Eq. (2.34) vanishes. Because ρ_0^* can only vary in height and time according to Eq. (2.33) and periodic boundary conditions:

$$\frac{\partial \rho_0^*}{\partial t^*} = -\frac{\partial}{\partial z^*} \langle \rho_0^* w_0^* \rangle_{xy} \tag{2.35}$$

Taking the time derivative of Eq. (2.33) gives another equation for $\frac{\partial \rho_0^*}{\partial t^*}$:

$$\frac{\partial \rho_0^*}{\partial t^*} = \frac{\partial \pi_{00}}{\partial t^*} (1/\kappa - 1) \, (\pi_{00}(t^*) - \beta z^*)^{(1/\kappa)-2} \tag{2.36}$$

Equating both Eqs. (2.35) and (2.36), integrating from $z^* = 0$ to an arbitrary z'^*, and using the wall boundary condition $\boldsymbol{w}_0(z^* = 0) = 0$ gives

$$\langle \rho_0^* w_0^* \rangle_{xy} \, (z'^*) = \frac{\partial \pi_{00}}{\partial t^*} ((1/\kappa) - 1) \int_{z^*=0}^{z'^*} (\pi_{00}(t^*) - \beta z^*)^{(1/\kappa)-2} \, dz^* \quad . \tag{2.37}$$

The antiderivative of the integrand is

$$F(z^*) = -\frac{(\pi_{00} - \beta z^*)^{(1/\kappa)-1}}{\beta((1/\kappa) - 1)} + \text{const.} \quad , \tag{2.38}$$

so that Eq. (2.37) becomes

$$\langle \rho_0^* w_0^* \rangle_{xy}(z'^*) = \frac{1}{\beta}\frac{\partial \pi_{00}}{\partial t^*}\left((\pi_{00} - \beta z'^*)^{(1/\kappa)-1} - (\pi_{00})^{(1/\kappa)-1} \right) \quad . \tag{2.39}$$

Setting the boundary conditions $w_0^*(z^* = z_{\text{top}}^*) \equiv 0$ requires the time derivative to vanish. As a result, both pressure and density are constant in time and only change with height according to

$$\pi_0(z^*) = \pi_{00} - \beta z^* \quad , \tag{2.40}$$

$$\rho_0^*(z^*) = (\pi_{00} - \beta z^*)^{(1/\kappa)-1} \quad , \tag{2.41}$$

and the leading-order continuity Eq. (2.34) reduces to the divergence constraint

$$\nabla^* \cdot (\rho_0^* \boldsymbol{v}_0^*) = 0 \quad . \tag{2.42}$$

This equation constitutes the anelastic continuity equation.

Since the ϵ^0 equations for momentum and temperature contain no information about $\boldsymbol{v}^*$ and θ^*, the ϵ^1 equations need to be considered next. The ϵ^1 terms in the momentum equation (2.29) read

$$\begin{aligned} \epsilon^1 : \quad \beta \frac{D\boldsymbol{v}_0^*}{Dt^*} &= -(\nabla^* \pi_1 + \theta_1^* \nabla^* \pi_0) \\ &= -\nabla^* \pi_1 + \theta_1^* \beta \boldsymbol{k} \quad , \end{aligned} \tag{2.43}$$

where π_0 was replaced by the solution obtained in Eq. (2.32). The first-order terms in the temperature equation (2.25) give

$$\epsilon^1 : \quad \frac{\partial \theta_1^*}{\partial t} + \boldsymbol{v}_0^* \cdot \nabla^* \theta_1^* = 0 \quad . \tag{2.44}$$

These two equations complete the dimensionless anelastic system which is summarized as

$$\beta \frac{\partial \boldsymbol{v}_0^*}{\partial t^*} + \beta \boldsymbol{v}_0^* \cdot \nabla^* \boldsymbol{v}_0^* = -\nabla^* \pi_1 + \theta_1^* \beta \boldsymbol{k} \quad , \tag{2.45}$$

$$\frac{\partial \theta_1^*}{\partial t^*} + \boldsymbol{v}_0^* \cdot \nabla^* \theta_1^* = 0 \quad , \tag{2.46}$$

$$\nabla^* \cdot (\rho_0^* \boldsymbol{v}^*{}_0) = 0 \quad . \tag{2.47}$$

The UCLA-LES solves the anelastic equations in *dimensional form*, which is readily obtained from the transformation back to physical variables:

$$\frac{\partial \boldsymbol{v}_0}{\partial t} + \boldsymbol{v}_0 \cdot \nabla \boldsymbol{v}_0 = -c_p \Theta_0 \nabla \tilde{\pi} + \frac{\tilde{\theta} g}{\Theta_0} \boldsymbol{k} \tag{2.48}$$

$$\frac{\partial \tilde{\theta}}{\partial t} + \boldsymbol{v}_0 \cdot \nabla \tilde{\theta} = 0 \tag{2.49}$$

$$\nabla \cdot (\rho_0 \boldsymbol{v}_0) = 0 \quad . \tag{2.50}$$

Herein, the first-order perturbations of the Exner pressure $\epsilon \pi_1$ and potential temperature $\epsilon \theta_1$ have been replaced by $\tilde{\pi}$ and $\tilde{\theta}$, respectively. If one neglects the higher-order terms in the power series given by Eq. (2.31), these correspond to

$$\tilde{\pi} \approx \pi - \pi_0 \quad , \tag{2.51}$$

$$\tilde{\theta} \approx \theta - \Theta_0 \quad . \tag{2.52}$$

Since Θ_0, or ϵ for that matter, is a constant, the temperature Eq. (2.49) is both valid for the perturbation $\tilde{\theta}$ as well as θ itself. Note, while all other quantities and differential operators are dimensional, the dynamic pressure perturbation $\tilde{\pi}$ remains as a non-dimensional variable.

2.1.3 *Moist atmosphere*

When simulating the moist atmosphere, the anelastic equations have to be modified to account for latent heat and compositional effects. This leads to a new state variable in place of the potential temperature and changes in the formulation of buoyancy in the momentum equation.

In the dry case, the first law of thermodynamics, Eq. (2.5),

$$c_p\, dT = dp/\rho + \delta q$$

was reflected by the balance equation for the potential temperature. However, if condensation and evaporation take place, latent heat release and consumption have to be included as an additional energy form in the first law

$$c_p\, dT = dp/\rho + \delta q + L_v\, dq_l \quad . \tag{2.53}$$

Herein, L_v is the enthalpy of vaporization of water. This form of the first law is approximately satisfied by the balance equation of a new state variable, the *liquid water potential temperature*

$$\theta_l = \theta \exp\left(-\frac{L_v q_l}{c_p T}\right) \quad . \tag{2.54}$$

The evolution equation follows from the first law including latent heat effects, Eq. (2.53), as

$$\frac{\partial \theta_l}{\partial t} + \boldsymbol{v} \cdot \nabla \theta_l = \frac{\theta_l \dot{q}}{T c_p} \quad . \tag{2.55}$$

The derivations of both Eqs. (2.53) and (2.55) are presented in Appendix A.4.

The liquid water potential temperature was first proposed by Betts [6] in 1973 and its usefulness for large-eddy simulation (LES) of shallow moist convection was later highlighted by Deardorff [12]. The main virtues of it are that (i) it is approximately conserved under both dry-adiabatic processes and under water phases changes and (ii) that it reduces to the potential temperature in the absence of condensate. If, in addition to liquid water, ice is present, the ice-liquid water potential temperature can be used [85].

Composition of the fluid affects the density of the fluid via the ideal gas law. Specifically, the gas constant depends on the composition [72] according to

$$R = q_d R_d + q_v R_v = R_d(1 + q_v R_v/R_d - q_t) \quad . \tag{2.56}$$

In order to continue to work with the gas constant for dry air, the *virtual potential temperature*

$$\theta_v = \theta(1 + q_v R_v/R_d - q_t) \tag{2.57}$$

is often used to carry the compositional effects rather than the gas constant of the mixture. Thus, the ideal gas law becomes

$$p = \rho R_d \theta_v \pi \quad . \tag{2.58}$$

From logarithmic differentiation of Eq. (2.58) and its linearization it follows that buoyancy from the dry case

$$b \approx -\frac{\rho - \rho_0}{\rho_0} g \approx \frac{\theta - \Theta_0}{\Theta_0} g \tag{2.59}$$

becomes

$$b \approx -\frac{\rho - \rho_0}{\rho_0} g \approx \frac{\theta_v - \Theta_0}{\Theta_0} g = \frac{\tilde{\theta}_v}{\Theta_0} g \tag{2.60}$$

in the moist case. Note the difference in the sign between the density and the temperature formulation. In summary, the adiabatic anelastic system for moist air becomes

$$\frac{\partial \boldsymbol{v}_0}{\partial t} + \boldsymbol{v}_0 \cdot \nabla \boldsymbol{v}_0 = -c_p \Theta_0 \nabla \tilde{\pi} + \frac{\tilde{\theta}_v g}{\Theta_0} \boldsymbol{k} \quad , \tag{2.61}$$

$$\frac{\partial \tilde{\theta}_l}{\partial t} + \boldsymbol{v}_0 \cdot \nabla \tilde{\theta}_l = 0 \quad , \tag{2.62}$$

$$\nabla \cdot (\rho_0 \boldsymbol{v}_0) = 0 \quad . \tag{2.63}$$

where $\tilde{\theta}_v$ is now the buoyancy variable in the momentum equation and the first law is now represented by the conservation of θ_l.

2.1.4 *LES-filtering and turbulence closure*

The flow in the STBL is a multi-scale turbulent flow. Unfortunately, it is currently and in the foreseeable future not possible to simulate all important scales on a computer since this requires more degrees of freedom, or grid points, than currently feasible. LES offers a way around this problem by explicitly simulating only larger, energy-carrying scales and modelling contributions of smaller scales.

The range of scales present can be expressed in terms of the turbulent Reynolds number

$$Re_t = \frac{VH}{\nu} \quad , \tag{2.64}$$

where H and V are a characteristic length scale, e.g. the BL depth, and fluctuation velocity scale, e.g. convection velocity, respectively, and ν ist the kinematic viscosity of air. For the simplest case of isentropic turbulence (c.f. Pope's textbook [54]) the ratio between the smallest dissipative scales, η, and the largest integral scales, H, scales as

$$\frac{H}{\eta} \sim Re_t^{3/4} \quad , \tag{2.65}$$

see e.g. the book by Sagout [57]. Thus, the degrees of freedom for a volume H^3 scales as $Re_t^{9/4}$.

A reasonable estimate for the STBL with

$$H \sim 1000\,\mathrm{m} \quad , \tag{2.66}$$

$$V \sim 1\,\mathrm{m\,s^{-1}} \quad , \tag{2.67}$$

and

$$\nu \sim 10^{-5}\,\mathrm{m^2\,s^{-1}} \tag{2.68}$$

gives a Reynolds number of 10^8 and a Kolmogorov scale, according to Eq. (2.65), of $\eta \sim 1\,\mathrm{mm}$. In other words, if a numerical scheme required one grid point per Kolmogorov length η to produce a converged solution, a numerical grid with 10^6 points in each direction or 10^{16} total degrees of

freedom would be necessary, which, still today, remains out of reach for high-performance computers. Currently, customary grids have on the order 10^3 points in each direction, approaching 10^4, which gives approximately 10^{10} to 10^{11} degrees of freedom (see e.g. the direct numerical simulation (DNS) of atmospheric convection by de Lozar and Mellado [10, 11] or the DNS of a turbulent channel flow by Lee and Moser [29]).

This continuing inability to simulate all scales led to the idea of large-eddy simulation (LES), where, as the name suggests, only the large scales that carry most of the turbulent kinetic energy are simulated and the less energetic small scales are modelled. This is achieved by splitting each principal variable into a filtered, or grid-scale, part and a residual, or subgrid-scale (SGS), part [54]. For instance, the velocity in x direction is expanded as

$$u(\boldsymbol{x},t) = \bar{u}(\boldsymbol{x},t) + u'(\boldsymbol{x},t) \quad . \tag{2.69}$$

If this splitting is applied to the anelastic Eqs. (2.61) to (2.63), a similar set of equations for the filtered variables is obtained,

$$\frac{\partial \bar{\boldsymbol{v}}}{\partial t} + \bar{\boldsymbol{v}} \cdot \nabla \bar{\boldsymbol{v}} = c_p \Theta_0 \nabla \overline{\tilde{\pi}} + \frac{g \overline{\tilde{\theta}}_v}{\Theta_0} \boldsymbol{k} + \frac{1}{\rho_0} \nabla \cdot (\rho_0 \boldsymbol{\tau}) \quad , \tag{2.70}$$

$$\frac{\partial \bar{\theta}_l}{\partial t} + \bar{\boldsymbol{v}} \cdot \nabla \bar{\theta}_l = \frac{1}{\rho_0} \nabla \cdot (\rho_0 \gamma_{\bar{\theta}_l}) + Q \quad , \tag{2.71}$$

$$\frac{\partial \bar{q}_t}{\partial t} + \bar{\boldsymbol{v}} \cdot \nabla \bar{q}_t = \frac{1}{\rho_0} \nabla \cdot (\rho_0 \gamma_{q_t}) \quad , \tag{2.72}$$

$$\nabla \cdot (\rho_0 \bar{\boldsymbol{v}}) = 0 \quad , \tag{2.73}$$

where additional terms, the turbulent fluxes of momentum

$$\boldsymbol{\tau} = \overline{\boldsymbol{v} \otimes \boldsymbol{v}} - \bar{\boldsymbol{v}} \otimes \bar{\boldsymbol{v}} \quad , \tag{2.74}$$

and and scalars,

$$\gamma_{\theta_l} = \overline{\boldsymbol{v}\theta_l} - \bar{\boldsymbol{v}}\bar{\theta}_l \quad , \tag{2.75}$$

emerged that depend on the SGS structure of the solution which is unknown. This is sometimes referred to as the *closure problem* and requires model assumptions to be made in order to solve the system (2.70) - (2.73).

In the UCLA-LES, these additional unknowns are approximated using a Smagorinsky-Lilly model (see Stevens et al. [75, 76]) which represents the SGS turbulence as diffusion governed by the eddy viscosity K_m according to

$$\boldsymbol{\tau} \approx \boldsymbol{\tau}^{\text{Smag.}} = -K_m \boldsymbol{D} \quad , \tag{2.76}$$

$$\gamma_{\theta_l} \approx \gamma_{\theta_l}^{\text{Smag.}} = -K_m / Pr_t \nabla \bar{\theta}_l \quad , \tag{2.77}$$

$$\gamma_{q_t} \approx \gamma_{q_t}^{\text{Smag.}} = -K_m / Sc_t \nabla \bar{q}_t \quad . \tag{2.78}$$

Herein, Sc_t and Pr_t are the turbulent Schmidt and Prandtl numbers, respectively, and $\boldsymbol{D}$ is the resolved deformation

$$\boldsymbol{D} = \nabla \boldsymbol{u} + (\nabla \boldsymbol{u})^T \quad . \tag{2.79}$$

Upon replacing $\boldsymbol{\tau}$ and γ_{θ_l, q_t} in the filtered Eqs. (2.70) to (2.73) by the models (2.76) and (2.78), the so called LES equations are obtained. The eddy viscosity in the Smagorinsky-Lilly model is computed according to

$$K_m = (C_s l)^2 S \sqrt{1 - \frac{Ri}{Pr_t}} \quad , \tag{2.80}$$

with the local SGS (or deformation) Richardson number

$$Ri = \frac{N^2}{S^2} \quad , \tag{2.81}$$

the magnitude of the deformation

$$S = \sqrt{\nabla \boldsymbol{u} : \boldsymbol{D}} \quad , \tag{2.82}$$

and the Brunt-Väisälä frequency

$$N^2 = \frac{g}{\Theta_0} \frac{\partial \bar{\theta}_v}{\partial z} \quad . \tag{2.83}$$

The remaining model parameters are the Smagorinsky constant C_s which is set to the value 0.23, and the eddy length scale

$$l^{-2} = (\Delta x, \Delta y, \Delta z)^{-2/3} + (z\kappa / C_s)^{-2} \tag{2.84}$$

which is chosen based on the numerical grid spacings, $\Delta x, \Delta y$ and Δz, and the height z. Finally, κ is the von Kármán constant which takes the value 0.4.

The equations will be discretized using a finite-volume (FV) method, the details of which are discussed in Chapt. 3. The central idea in FV methods is to subdivide the problem domain into finite control volumes and keep track of changes of the content of each volume. For this, it is appropriate to consider the integral conservative form of Eqs. (2.70)-(2.73). The conservative differential form of the Eqs. (2.70)-(2.73) can be obtained by multiplying by ρ and adding the continuity Eq. (2.12), times $\bar{\boldsymbol{v}}$, times $\overline{\bar{\theta}}$, or times $\bar{q}_t$, respectively. With this, the anelastic system become

$$\frac{\partial \rho_0 \bar{\boldsymbol{v}}}{\partial t} + \nabla \cdot (\rho_0 \bar{\boldsymbol{v}} \otimes \bar{\boldsymbol{v}}) = \rho_0 c_p \Theta_0 \nabla \overline{\bar{\pi}} + \frac{\rho_0 g \overline{\bar{\theta}}_v}{\Theta_0} \boldsymbol{k} + \nabla \cdot (\rho_0 \boldsymbol{\tau}) \quad , \tag{2.85}$$

$$\frac{\partial \rho_0 \bar{\theta}_l}{\partial t} + \nabla \cdot (\rho_0 \bar{\theta}_l \bar{\boldsymbol{v}}) = \nabla \cdot (\rho_0 \gamma_{\bar{\theta}_l}) + Q(\bar{\theta}_l) \quad , \tag{2.86}$$

$$\frac{\partial \rho_0 \bar{q}_t}{\partial t} + \nabla \cdot (\rho_0 \bar{q}_t \bar{\boldsymbol{v}}) = \nabla \cdot (\rho_0 \gamma_{q_t}) \quad . \tag{2.87}$$

The continuity equation remains unchanged. Integrating over an arbitrary, stationary control volume V and using Gauss's theorem to replace the volume integrals over the advective and diffusive flux divergences by surface integrals yields the integral conservative form

$$\begin{aligned} \int_V \frac{\partial \rho_0 \bar{\boldsymbol{v}}}{\partial t} \, dV + \oint_S (\rho_0 \bar{\boldsymbol{v}} \otimes \bar{\boldsymbol{v}}) \cdot \boldsymbol{n} \, dS = \int_V \rho_0 c_p \Theta_0 \nabla \bar{\pi} \, dV \\ + \int_V \frac{\rho_0 g \bar{\theta}'}{\Theta_0} \boldsymbol{k} \, dV + \oint_S \rho_0 \boldsymbol{\tau} \cdot \boldsymbol{n} \, dS \, , \end{aligned} \tag{2.88}$$

$$\int_V \rho_0 \frac{\partial \bar{\theta}_l}{\partial t} \, dV + \oint_S \rho_0 \bar{\theta}_l \boldsymbol{v} \cdot \boldsymbol{n} \, dS = \oint_S \rho_0 \gamma_{\bar{\theta}_l} \cdot \boldsymbol{n} \, dS + \int_V Q(\bar{\theta}_l) \, dV \, , \tag{2.89}$$

$$\int_V \rho_0 \frac{\partial \bar{q}_t}{\partial t} \, dV + \oint_S \rho_0 \bar{q}_t \boldsymbol{v} \cdot \boldsymbol{n} \, dS = \oint_S \rho_0 \gamma_{\bar{q}_t} \cdot \boldsymbol{n} \, dS \quad , \tag{2.90}$$

suitable for FV discretization.

A REMARK ON THE UCLA-LES IMPLEMENTATION For the scalar transport, the UCLA-LES implements the non-conservative advective form of the

transport equations. The implemented equation follows if the advection term, e.g. for the temperature, is expanded as

$$\boldsymbol{v} \cdot \nabla \bar{\theta}_l = \frac{1}{\rho_0} \nabla \cdot (\rho_0 \bar{\theta}_l \boldsymbol{v}) - \frac{1}{\rho_0} \bar{\theta}_l \nabla \cdot (\rho_0 \boldsymbol{v}) \quad . \tag{2.91}$$

After integrating over the control volume V and applying Gauss's theorem, the temperature Eq. (2.71) becomes

$$\int_V \rho_0 \frac{\partial \bar{\theta}_l}{\partial t} \, dV + \oint_S \rho_0 \bar{\theta}_l \boldsymbol{v} \cdot \boldsymbol{n} \, dS - \underbrace{\int_V \bar{\theta}_l \nabla \cdot (\rho_0 \boldsymbol{v}) \, dV}_{=0} =$$

$$\oint_S \rho_0 \gamma_{\bar{\theta}_l} \cdot \boldsymbol{n} \, dS + \int_V Q(\bar{\theta}_l) \, dV \quad .$$

Advection of temperature is now expressed in term of the flux form and an additional dilatation source term. The UCLA-LES discretizes both terms. Since the dilatation term vanishes according to the anelastic continuity Eq. (2.63), the results are practically identical to using the conservative Eq. (2.89). Thus, for the following discussion of the numerical discretization in Chapt. 3, the conservative equations will be used.

2.2 THE LEVEL SET METHOD

The cloud-top interface is charaterized by sharp gradients of the specific humidity and temperature profiles. Instead of resolving these gradients, the level set method is used to represent this transitional layer as a discontinuity. This section presents the equations that are solved as part of the level set method and its coupling to the anelastic equations of motion.

Level set methods describe interfaces as implicit surfaces of a space-filling scalar function. This implicit surface representation is described in Sect. 2.2.1. Its evolution in time is governed by a transport equation for that scalar function, as shown in Sect. 2.2.2. Section 2.2.3 then introduces the concept of signed-distance functions, which are typically chosen for the implicit surface representation due to their smoothness in the vicinity of the interface. They need to be frequently regularized into signed-distance state which is typically done using another partial differential equation (PDE). Finally, boundary conditions are needed in order to couple the unknowns of the equations of motion to the level set. Here, these are generated with help of the Fedkiw at al.'s ghost fluid method [19] which uses extrapolation in the interface normal direction based on another PDE. This is shown in Sect. 2.2.4.

2.2.1 *Implicit surfaces representation*

Level set methods are based on the idea of implicit surfaces. Rather than explicitly keeping track of points on the interface in a Lagrangian sense, level set methods describe the interface geometry in terms of the zero level set of a smooth space-filling function $\phi(\boldsymbol{x}, t)$, with $\boldsymbol{x}$ being the position vector $(x, y, z)^T$. The location of the interface ϕ_0 is then implicitly given as the set of points where ϕ vanishes:

$$\phi_0 = \{\boldsymbol{x} : \phi(\boldsymbol{x}, t) = 0\} \, . \tag{2.92}$$

Thus, an n-dimensional surface is described using an $n+1$ dimensional function and, once defined, the location of the implicit surface is readily

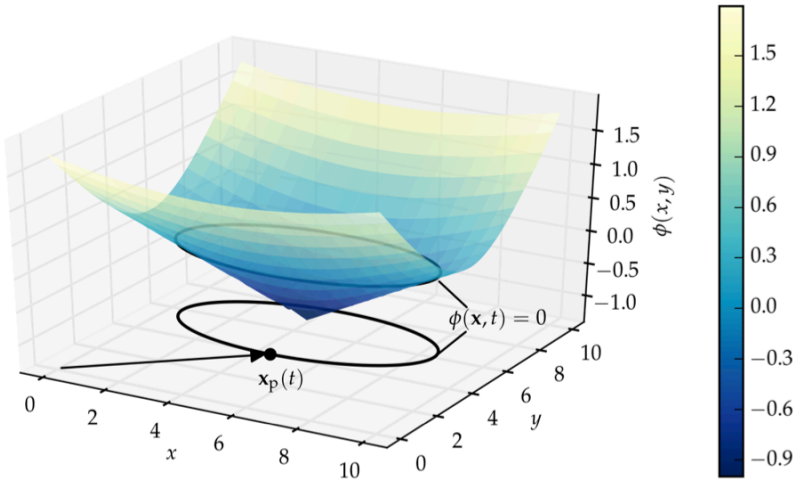

Figure 5: 2D elliptic cone function $\phi(x,y)$ and its zero level set describing a 1D elliptic interface $r(\theta)$ (black line). The interface has been projected onto the $x-y$ plane. $\boldsymbol{x}_p = (x_p, y_p)^T$ is the position vector of an arbitrary point on the interface in this 2D space.

obtained by finding its roots. Figure 5 illustrates this with a 2D example where an ellipse is described in terms of the zero level set of an elliptical cone function. The function $\phi(\boldsymbol{x},t)$ is referred to as *level set function*.

The major advantage of the implicit surface representation over other interface tracking methods is that the level set function carries specific information about the topology of the interface:

1. The location of the interface is given by the $\phi = 0$ isosurface.
2. Both sides of the interface are directly identified by the sign of ϕ, which divides the domain of interest Ω into the three regions

$$\Omega_+ = \{\boldsymbol{x} : \phi(\boldsymbol{x},t) > 0\} \tag{2.93}$$
$$\phi_0 = \Omega_0 = \{\boldsymbol{x} : \phi(\boldsymbol{x},t) = 0\} \tag{2.94}$$
$$\Omega_- = \{\boldsymbol{x} : \phi(\boldsymbol{x},t) < 0\} \quad . \tag{2.95}$$

3. Local information, such as the interface normals $\boldsymbol{n}$ and curvature κ are given by the local derivatives

$$\boldsymbol{n} = \frac{\nabla\phi}{|\nabla\phi|}, \quad \kappa = \nabla\cdot\boldsymbol{n} = \frac{\nabla^2\phi}{|\nabla\phi|}\,. \tag{2.96}$$

In the case of the STBL, the three regions correspond to the free atmosphere, the inversion, and the boundary layer. The choice in which region ϕ is positive and negative is arbitrary. Here, ϕ is defined such that $\phi > 0$ for air above the cloud-top interface, i.e. Ω_+ corresponds to the free atmosphere.

2.2.2 *The level set equation*

Level set methods use the implicit surface idea to describe evolving surfaces the dynamics of which are described in terms of the *level set equation*

$$\frac{\partial\phi}{\partial t} + \boldsymbol{v}_\phi\cdot\nabla\phi = 0 \quad , \tag{2.97}$$

where $\boldsymbol{v}_\phi$ is the appropriate transport velocity field. If the interface is passively advected by the surrounding flow, as is the case for a contact discontinuity, then the external velocity equals the flow velocity, i.e. $\boldsymbol{v}_\phi = \boldsymbol{v}$. Additional processes may contribute to the motion of the interface, e.g. interfacial mass transport due to entrainment or the consumption and generation of a fluid component due to chemical reactions. Such effects can be incorporated by an additional velocity component in the normal direction. For instance in case of turbulent entrainment, the external velocity field becomes $\boldsymbol{v}_\phi = \boldsymbol{v} + E\boldsymbol{n}$, where E denotes a local turbulent entrainment rate. This definition is in contrast to what is typically called entrainment rate, w_e, of an atmospheric boundary layer, which denotes a global statistic as in Eq. (1.1).

2.2.3 *Signed-distance functions*

The level set function, ϕ, may have any shape as long as it satisfies Eqs. (2.93) to (2.95) and is monotone in the vicinity of ϕ_0. It is numerically convenient to use smooth functions for ϕ. Specifically, it has been customary to initialize ϕ into a signed-distance function of the interface which satisfies the eikonal equation

$$|\nabla\phi| = 1 \quad . \tag{2.98}$$

Such a function will be smooth in the vicinity of a smoothly shaped interface and can be evolved numerically with high accuracy according to the level set Eq. (2.97).

Generally, the level set function will not maintain its signed-distance property as the flow evolves. Especially, in the present case of interfacial convection, the level set function will quickly steepen in the vicinity of the stably stratified interface. This would generate the same difficulties in accurately simulating the evolution of zero level set which the level set method is intended to circumvent.

This problem can be avoided by frequently reinitializing ϕ into a signed-distance function. While the most intuitive way is to directly set ϕ values to the shortest distance to the interface, it is more efficient to use a PDE. Sussman et al.[82] proposed to iterate the reinitialization equation

$$\frac{\partial\phi}{\partial\tau} = \operatorname{sign}(\tilde{\phi})(1 - |\nabla\phi|) \tag{2.99}$$

in virtual time τ to steady state. Here, $\tilde{\phi}$ is the solution of the current simulation time step which is held constant during the reinitialization process. The effect of equation (2.99) can be understood more easily if it is restated as the hyperbolic transport equation

$$\phi_\tau + \operatorname{sign}(\tilde{\phi})\boldsymbol{n}\cdot\nabla\phi = \operatorname{sign}(\tilde{\phi}) \quad . \tag{2.100}$$

With the values of ϕ at the interface as boundary conditions,

$$\phi(\boldsymbol{x}_p, \tau) = \tilde{\phi}(\boldsymbol{x}_p) \quad \forall \quad \boldsymbol{x}_p \in \phi_0 \quad , \tag{2.101}$$

Eq. (2.100) caries the distance information away from the interface such that, in the steady state, the advective transport of ϕ by the virtual velocity $\operatorname{sign}(\tilde{\phi})\boldsymbol{n}$ balances the source term $\operatorname{sign}(\tilde{\phi})$. The hyperbolic nature of this equation also suggests that upwind schemes ought to be used to discretize $\nabla\phi$ in Eq. (2.100) and, consequently, in Eq. (2.99).

Unfortunately standard numerical schemes to solve Eq. (2.100) slightly displace the zero level set. As a result, much of the research about numerical schemes to solve the reinitialization equation has been devoted to minimize that shortcoming. Sussman et al. [82] proposed a Godunov scheme to solve the reinitialization equation. But as Russo and Smereka [56] later pointed out, the numerical displacement of Sussman et al.'s scheme is proportional to the number of iterations such that the displacement error can potentially be large, if the level set is frequently reinitialized. They attribute part of the problem to the fact that Sussman et al.'s scheme does not adhere to the upwind principle in points adjacent to the interface and improve on it with their *subcell fix*, making the method strictly upwind in those points. They further show, that the maximum interface displacement of their method is bounded and independent of the number of iterations. Hartman [24] and Hartmann et al. [22, 23] further reduce reinitialization displacement with a family of constrained reinitialization schemes that result from a minimization of the displacement error which they also generalized to higher-order schemes [21].

Here, a variation of Russo and Smereka's subcell fix is used for reinitialization, the details of which are presented in Sect. 3.3.2 in the next chapter.

2.2.4 *Interface boundary conditions*

The anelastic equations are coupled to the level set by setting appropriate boundary conditions at the interface and modifying the numerical method accordingly. As described in the introduction, the location of the cloud-top interface is governed by the interplay between turbulent mixing at the turbulent-laminar interface of the cloud top and the re-homogenization due to convection within the BL. (Molecular dissipation of mass and enthalpy is neglected in the anelastic equations.) The appropriate discontinuous analogue of the cloud top interface is that of a semi-permeable contact discontinuity, i.e. the modelled cloud-top interface is permeable from only one side, namely by parcels from the free atmosphere into the BL.

If no entrainment mixing were present, the cloud-top interface became a contact discontinuity with no permeability. This case is considered in the present thesis. (A strategy for including entrainment mixing is presented in Appendix B.) The appropriate boundary conditions at the interface result from requiring that there is no molecular or turbulent exchange of water or enthalpy between the STBL and the free atmosphere. This requirement translates into Neumann conditions with zero gradients in the interface normal direction on both sides, i.e. for an arbitrary scalar φ

$$\lim_{\boldsymbol{x}_+ \to \boldsymbol{x}_0} (\boldsymbol{n} \cdot \nabla \varphi) = \lim_{\boldsymbol{x}_- \to \boldsymbol{x}_0} (\boldsymbol{n} \cdot \nabla \varphi) = 0 \quad \forall\, \boldsymbol{x}_0 : \phi(\boldsymbol{x}_0) = 0 \quad , \tag{2.102}$$

where $\boldsymbol{x}_+ \in \Omega_+$ and $\boldsymbol{x}_- \in \Omega_-$. These conditions are realized by two-sided extrapolation using Fedkiw et al.'s [18] *ghost fluid method*. For this, two PDEs of the form

$$\frac{\partial \varphi}{\partial \tau} + \boldsymbol{n} \cdot \nabla \varphi = 0 \tag{2.103}$$

are iterated in virtual time τ, one in $(\phi_0 \bigcup \Omega_+)$ and one in $(\phi_0 \bigcup \Omega_-)$, in order to generate ghost data on the respective opposite sides of the interface. The extrapolation is based on physical data on one side serving as Dirichlet boundary conditions for Eq. (2.103). The extrapolated ghost data is then used as a Dirichlet boundary condition for φ such that the Neumann

conditions, Eqs. (2.102), are met. The details of the numerical algorithm are presented in Sect. 3.3.3 in the next chapter.

3 NUMERICAL METHODS

The level set-based front tracking algorithm has been implemented in the UCLA-LES (University of California, Los Angeles Large-Eddy Simulation). The original UCLA-LES has been widely used for simulation of various problems in the realm of atmospheric convection. Examples include shallow cumulus clouds [36, 74, 86], stratocumulus clouds [4, 79], as well as transitions between cloud types under changing large-scale conditions [5, 58].

This chapter presents the relevant numerical methods that are implemented in the original UCLA-LES code as well as the methods of the front-tracking algorithm and necessary modifications to the original code. The UCLA-LES discretizes the governing equations using the finite-volume method. The concept is explained in detail in text books such as the ones by LeVeque [31] or Ferziger and Peric [20], however Sect. 3.1 gives a concise overview on the concept for the sake of completeness. Based on this, Sect. 3.2 describes the numerics of the UCLA-LES relevant for the modifications made as part of the front-tracking algorithm which is described in detail in Sect. 3.3.

The code of both the original UCLA-LES as well as the modifications done by the author of this thesis is available on the Web on GitHub[1].

3.1 FINITE-VOLUME METHODS

The basic idea of finite-volume (FV) methods is to subdivide the problem domain into small control volumes (CVs), or cells, ΔV and keep track of how the content of any conserved variable changes over time due to fluxes over its boundaries or due to sources and sinks within the cell. This is analogous to a rigorous derivation of balance equations from physical conservation laws. Thus, FV methods are naturally applied to the integral form of the balance equations, Eqs. (2.88)-(2.90), which follow from the same approach. Alternatively, the integral equations can be formally derived from the differential form, Eqs. (2.70)-(2.73) simply by integrating over an arbitrary CV V. If ρ is moved inside the time derivative, it can be moved out of the integral by requiring fixed limits of integration, i.e. requiring that the CVs do not move or deform over time, and by requiring that the time derivative be smooth in space. The results are equations of the form

$$\frac{d}{dt}\int_V \rho\varphi \, dV = -\int_V \nabla \cdot \boldsymbol{f}(\varphi) \, dV + \int_V s(\varphi, x, t) \, dV \quad , \tag{3.1}$$

where $\boldsymbol{f}(\varphi)$ denotes the net flux vector and $s(\varphi, x, t)$ denotes the net source term of an arbitrary scalar φ. Using Gauss's theorem, the volume integral over the flux divergence $\nabla \cdot \boldsymbol{f}(\varphi)$ can be restated as the surface integral of the normal flux through the CV's boundaries and Eq. (3.1) becomes

$$\frac{d}{dt}\int_V \rho\varphi \, dV = -\oint_S \boldsymbol{f}(\varphi) \cdot \boldsymbol{n} \, dS + \int_V s(\varphi, x, t) \, dV \quad , \tag{3.2}$$

where $\boldsymbol{n}$ denotes the CV surface normal.

This equation is valid for arbitrary CVs. If the domain of interest is divided into small control volumes ΔV and Eq. (3.2) is applied to each individual

1 https://github.com/uclales/uclales

volume, a set of integral differential equations is obtained. Then, by finding approximations to the volume and surface integrals, it can be transformed into a set of algebraic equations. The time derivative can be removed by integrating the equation in time as described in Sect. 3.1.3. In the following, this scalar transport equation is used to illustrate the FV concept. Since all of the governing Eqs. (2.88)-(2.90) share this form, the following considerations apply to them accordingly.

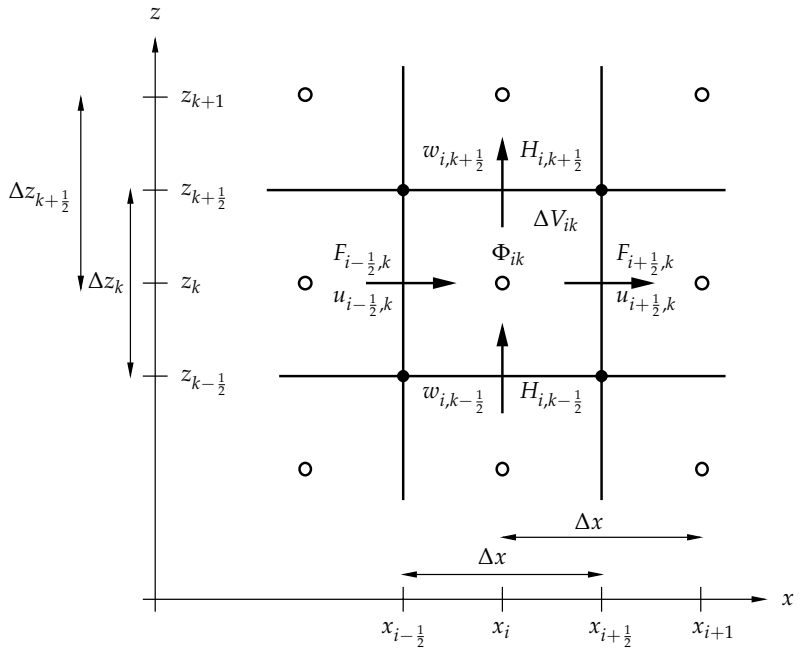

Figure 6: Computational grid used in the UCLA-LES. F and H denote horizontal and vertical fluxes of an arbitrary scalar Φ, respectively, through faces of the control volume ΔV.

The FV concept can be in applied to structured and unstructured grids with arbitrarily shaped CVs. Here, a structured Cartesian grid is used. Especially when flows are considered that are driven by internal volume forces without boundary conditions for complex geometry, structured Cartesian grids are favoured over unstructured grids due to their simplicity: Structured grids make it efficient to lay out and access data in computer memory and easy to compute local grid geometry. Figure 6 shows the grid as used in the University of California, Los Angeles Large-Eddy Simulation (UCLA-LES) in two dimensions. It can be easily generalized to three dimensions. All state variables—namely density ρ, liquid water potential temperature θ_l, pressure π, and the total water mixture fraction q_t—are located at the cell centres and are referred to as *thermal points*. Thermal points are denoted by $\boldsymbol{x}_{ijk} = (x_i, y_j, z_k)$ and are marked by the open circles in Figure 6. Velocities are staggered half a grid-point in the direction of the respective velocity component and located on the centres of the cell faces, referred to as *momentum points*. Momentum points are indicated by the black arrows and are denoted by modifying the coordinate in the respective direction. The modified coordinate is indicated by primed indices $i' = i + 1/2$, $j' = j + 1/2$, or $k' = k + 1/2$. For instance, the momentum point at the top of cell (i, j, k) has coordinates $(x_i, y_j, z_{k+1/2}) = (x_i, y_j, z_{k'})$. The grid spacing is equidistant in the two lateral directions, i.e. for all cells, the widths Δx and Δy equal the lateral distances between cell centres and between cell

faces: $\Delta x = x_{i'} - x_{i'-1} = x_{i+1} - x_i$ and $\Delta y = y_{j'} - y_{j'-1} = y_{j+1} - y_j$. In the vertical direction, the grid allows for stretching. Thus the grid spacings may be different for each vertical level for all cells and $\Delta z_k = z_{k'} - z_{k'-1}$ and $\Delta z_{k'} = z_{k+1} - z_k$. The grid is organized such that thermal points, even in the stretched case, are always located half-way between momentum points, i.e. $z_k = 1/2(z_{k'-1} + z_{k'})$. On this grid, the cell (ijk) occupies the volume $\Delta V_{ijk} = \Delta x \Delta y \Delta z_k$ and is bounded by cell faces having the areas $\Delta x \Delta y$, $\Delta x \Delta z_k$, and $\Delta y \Delta z_k$, respectively.

The following sections explain how the integrals and the time derivative in Eq. (3.2) are discretized on the grid shown in Fig. 6.

3.1.1 *Discretization of volume integrals*

Since the numerical unknowns Φ_{ijk} are defined at the midpoint of each cell (thermal points), it is natural to approximate the volume integral using the midpoint quadrature rule

$$\int_{\Delta V_{ijk}} \rho\varphi \, dV = \rho_k \Phi_{ijk} \, \Delta V_{ijk} + \mathcal{O}(\Delta x^2, \Delta y^2, \Delta z_k^2) \quad , \tag{3.3}$$

which is second-order accurate. Because density is uniform in the lateral directions in the anelastic system (2.70)-(2.73), the indices i and j have been omitted. By comparison with the definition equation of the cell average

$$\overline{\rho\varphi} = \frac{1}{\Delta V} \int_{\Delta V} \rho\varphi \, dV \quad ,$$

the midpoint value $\rho_k \Phi_{ijk}$ in Eq. (3.3) can be seen to be an approximation to the cell average.

Any other variables that are not defined on the thermal points need to be interpolated first. In order to then maintain the second-order accuracy for the midpoint rule, the interpolation is required to be at least second-order accurate as well. For instance, at least linear interpolation supported by the cell face values had to be used.

3.1.2 *Discretization of surface integrals*

The integral over the surface of the grid cell, A_{ijk} can be split up into individual integrals over the individual cell faces A_l, i.e. in 3D with $l \in \{1, 2, ..., 6\}$ the surface integral can be restated as

$$\oint_{A_{ijk}} \boldsymbol{f}(\varphi) \cdot \boldsymbol{n}, \, dA = \sum_{l=1}^{6} \oint_{A_l} \boldsymbol{f}(\varphi) \cdot \boldsymbol{n} \, dA \quad . \tag{3.4}$$

Each surface integral is now approximated using numerical quadrature. For this, the flux $f(\varphi)$ has to be evaluated and integrated on the cell face. On the numerical grid shown in Fig. 6, the midpoint rule lends itself to approximate the surface integral over the cell face. The thermal points, where the scalars represented by φ are defined, are located on lines through the centres of cell faces. Thus, data needed on the momentum point can be interpolated linearly from two neighbouring thermal points to second-order. Then, with

F, G, and H denoting the approximated midpoint fluxes in the x, y, and z direction, respectively, one obtains the surface integral

$$\sum_{l=1}^{6} \oint_{A_l} \boldsymbol{f}(\varphi) \cdot \boldsymbol{n}\, dA = (F_{i'},_{j,k} - F_{i'-1,j,k})\Delta y \Delta z_k + (G_{i,j',k} - G_{i,j'-1,k})\Delta x \Delta z_k + (H_{i,j,k'} - H_{i,j,k'-1})\Delta x \Delta y + \mathcal{O}(\Delta x^2, \Delta y^2, \Delta z^2) \quad . \tag{3.5}$$

Since both steps are second-order accurate, the quadrature is second-order accurate as well.

By replacing the volume and surface integrals in the balance Eq. (3.2) with the discrete approximations given by Eqs. (3.3) and (3.5), the integral equation can be restated approximately as

$$\begin{aligned} \frac{d\Phi_{ijk}}{dt} = &- \frac{1}{\rho_k} \frac{F_{i',j,k} - F_{i'-1,j,k}}{\Delta x} \\ &- \frac{1}{\rho_k} \frac{G_{i,j',k} - G_{i,j'-1,k}}{\Delta y} \\ &- \frac{1}{\rho_k} \frac{H_{i,j,k'} - H_{i,j,k'-1}}{\Delta z_k} + \frac{1}{\rho_k} S_{ijk} \quad , \end{aligned} \tag{3.6}$$

where S_{ijk} is the midpoint value of the source term $s(\varphi, \boldsymbol{x}, t)$. This form is obtained after both sides have been divided by $\rho_k \Delta x \Delta y \Delta z_k$. (Because both the density and the cell volume are constant in time, they can be moved out of time derivative and on the right hand side.) If the right hand side of Eq. (3.6) is condensed into the spatial operator L, it can be abbreviated as

$$\frac{d\Phi}{dt} = L(\Phi) \quad . \tag{3.7}$$

Thus, $L(\Phi)$ corresponds to the rate of change of Φ which will be referred to as *tendency* in the following.

3.1.3 *Time integration*

In order to obtain an iterative time-marching scheme, the time derivative has to be discretized. In a FV manner this is be done by integrating from time t^n to $t^{n+1} = t^n + \Delta t$ which yields

$$\Phi^{n+1} = \Phi^n + \int_{t^n}^{t^{n+1}} L(\Phi)\, dt \quad \text{with} \quad \Phi^n = \Phi(t^n) \quad . \tag{3.8}$$

Note that this represents the exact time integral of Eq. (3.6). The discrete approximation consists in how the time integral on the right hand side is evaluated. If $L(\Phi)$ is evaluated at time level t^n and considered constant over the time step Δt, on obtains the classical explicit Euler method. Evaluating $L(\Phi)$ at time t^{n+1} instead, gives the implicit Euler method. Both are first-oder accurate, i.e. the leading error scales as Δt, or $\mathcal{O}(\Delta t)$. While the implicit method is unconditionally stable, stability of the explicit method is bound to a maximum critical time step [20, 31]

$$\Delta t \leq \Delta t_{\text{crit.}} \quad .$$

The explicit Euler method can expressed as special one-step case within the family of multi-step Runge-Kutta (RK) methods. Shu and Osher [66] formulate these methods as

$$\Phi^{(0)} = \Phi^n \tag{3.9}$$

$$\Phi^{(l)} = \sum_{k=0}^{l-1} (\alpha_{lk}\Phi^{(k)} + \Delta t \beta_{lk} L(\Phi^{(k)})) \quad l = 1, 2, 3, ..., m \tag{3.10}$$

$$\Phi^{n+1} = \Phi^{(m)} \quad , \tag{3.11}$$

which is now known as the Shu-Osher form of RK methods. Here, the superscripts in parentheses, (l), indicate the number of the RK step, as opposed to the superscripts without parentheses which indicate the global time step. Schemes of this form are explicit and thus easy to parallelize by domain decomposition. The schemes differ in the storage requirements for intermediate results and stability region, order of convergence, and, obviously, the number of intermediate steps. Spiteri and Ruuth [70] review standard RK schemes and present optimal schemes in terms of stability region at a given order of accuracy and also present low-storage variants which sometimes trade off computational efficiency.

3.2 THE UCLA-LES FLOW SOLVER

The section above introduced the general idea behind FV methods: By approximating integrals over fluxes and source terms using numerical quadrature, integral equations of the form of Eq. (3.2) were transformed into a set of discrete equations of the form (3.6). Similarly, numerical quadrature helps to approximate the remaining time derivative and transform the differential equations into a set of algebraic equations that can be solved using an iterative time-stepping scheme. This section presents the details of the spatial discretizations as well as the time-stepping scheme which are used in the standard UCLA-LES. The discretization of the scalar transport equation is specifically emphasised since this scheme is later modified to be coupled with the level set method in order to improve the representation of discontinuous scalar fields (see Sect. 3.3).

3.2.1 *Time integration*

The UCLA-LES uses a three-step, third-order RK scheme with coefficients α_{ik} and β_{ik} as listed in Tab. 4. It can be summarized as follows:

$$\Phi^{(1)} = \Phi^{(0)} + \frac{8}{15}\Delta t L\left(\Phi^{(0)}\right) \tag{3.12}$$

$$\Phi^{(2)} = \Phi^{(1)} - \frac{17}{60}\Delta t L\left(\Phi^{(0)}\right) + \frac{5}{12}\Delta t L\left(\Phi^{(1)}\right) \tag{3.13}$$

$$\Phi^{(3)} = \Phi^{(2)} - \frac{5}{12}\Delta t L\left(\Phi^{(1)}\right) + \frac{3}{4}\Delta t L\left(\Phi^{(2)}\right) \tag{3.14}$$

where $\Phi^{(0)} = \Phi^n$ and $\Phi^{n+1} = \Phi^{(3)}$. Note that this particular scheme requires only storage for the solution at the current RK step and two additional tendency arrays.

Table 4: Coefficients of the UCLA-LES Runge-Kutta scheme

RK step		a_{lk}			β_{lk}		
$l \downarrow$	$k \rightarrow$	0	1	2	0	1	2
1		1			$\frac{8}{15}$		
2		0	1		$-\frac{17}{60}$	$\frac{5}{12}$	
3		0	0	1	0	$-\frac{5}{12}$	$\frac{3}{4}$

The UCLA-LES adjusts the time step Δt at every iteration n so the Courant-Friedrichs-Lewy (CFL) number

$$\max\left[\max_{(i'jk)}\left(\frac{|u_{i'jk}|}{\Delta x}\right), \max_{(ij'k)}\left(\frac{|v_{ij'k}|}{\Delta y}\right), \max_{(ijk')}\left(\frac{|w_{ijk'}|}{\Delta z_{k'}}\right)\right]\Delta t = 0.5$$

is maintained. In every RK step, the UCLA-LES computes the total tendency by accumulating the tendencies of each process

$$L(\Phi^{(l)}) = {}^{\text{adv}}L(\Phi^{(l)}) + {}^{\text{diff}}L(\Phi^{(l)}) + {}^{\text{source/sink}}L(\Phi^{(l)}) \quad .$$

Each operator on the right hand side represents a tendency of Φ due to advection and diffusion, denoted by 'adv' and 'diff', and effects of sources and sinks. The following sections describe how the UCLA-LES discretizes these individual parts.

3.2.2 *Scalar advection in the UCLA-LES*

The advective tendency results from of the isolated advection problem

$$\int_V \rho_0 \frac{\partial \varphi}{\partial t}\, dV = -\oint_S \rho_0 \varphi \boldsymbol{v}\cdot\boldsymbol{n}\, dS \tag{3.15}$$

within the scalar transport equations (2.89) and (2.90), where φ represents either q_t or θ_l. Discretizing the advection problem with FVs as described above, the corresponding rate of change is

$$\begin{aligned}{}^{\text{adv}}L(\Phi^{(l)}) = -\Bigg[&\frac{F^{(l)}_{i'jk} - F^{(l)}_{i'-1,j,k}}{\Delta x} + \frac{G^{(l)}_{ij'k} - G^{(l)}_{i,j'-1,k}}{\Delta y} \\ &+ \frac{1}{\rho_{0,k}}\frac{H^{(l)}_{ijk'} - H^{(l)}_{i,j,k'-1}}{\Delta z_k}\Bigg] \quad ,\end{aligned} \tag{3.16}$$

where F, G, and H denote the advective fluxes in the x, y, and z direction, respectively. Note that in the anelastic approximation the density is constant along the horizontal directions on a particular k level. Thus, $1/\rho_{0,k'}$ cancels with the density in the horizontal fluxes F and G and is only retained in front of the vertical terms. The advective fluxes are discretized using the scheme

$$\begin{aligned}H_{k'} = &\frac{1}{2}(\Phi_{k+1} + \Phi_k)\,\rho_{0,k'} w_{k'} \\ &- \frac{1}{2}(\Phi_{k+1} - \Phi_k)\left[(1 - C_{k'})\rho_{0,k'}|w_{k'}| + \rho_{0,k'} w_{k'}\frac{w_{k'}\Delta t}{\Delta z_{k'}} C_{k'}\right] \quad ,\end{aligned} \tag{3.17}$$

where the indices i, j and l have been dropped because they are the same in every term. The density $\rho_{0,k'}$ is the interpolated value $\frac{\rho_{0,k}+\rho_{0,k+1}}{2}$ in the cell face. The symbol $C_{k'}$ denotes a flux limiter function which assumes values between zero and one. Using $w_{k'}w_{k'} = |w_{k'}|^2$ and factoring out $\rho_{0,k'}|w_{k'}|$, it is easy to show that this form is equivalent to LeVeque's advective flux based on piecewise linear reconstruction (see LeVeque's book [31], eq. (6.32), p. 113)

$$H_{k'} = \frac{1}{2}(\Phi_{k+1}+\Phi_k)\,\rho_{0,k'}w_{k'} - \frac{1}{2}(\Phi_{k+1}-\Phi_k)\,\rho_{0,k'}|w_{k'}| + \frac{1}{2}(\Phi_{k+1}-\Phi_k)\,\rho_{0,k'}|w_{k'}|\left[1-\frac{|w_{k'}|\Delta t}{\Delta z_{k'}}\right]C_{k'} \quad . \tag{3.18}$$

Note that the correct grid spacing in the two equations above is not Δz_k but $\Delta z_{k'}$ which corresponds to the vertical distance between the thermal points $\boldsymbol{x}_{ijk}$ and $\boldsymbol{x}_{i,j,k+1}$ (see Fig. 6). The first line in Eq. (3.18) corresponds to the first-order upwind flux, which can be easily verified by considering the two cases $w_{k'} \geq 0$ and $w_{k'} < 0$. The second line corrects the first-order flux to second-order in the case of $C'_k = 1$. The horizontal fluxes are computed using the same scheme with indices and grid spacing changed accordingly. They only differ in that the density is removed from the equation as it cancelled with the $1/\rho_{0,k'}$ factor due to the lack of lateral variability.

The UCLA-LES uses the monotonized-central (MC) limiter as default but also offers the Minmod, van-Leer, and Superbee limiter. The MC limiter (see e.g. LeVeque's book [31]) is given by

$$C_{i'} = \max(0, \min(2r_{i'}, 1/2(1+r_{i'}), 2))$$

where $r_{i'}$ denotes the ratio of slopes in the upwind direction

$$r_{i'} = (\Phi_{I+1}-\Phi_I)/(\Phi_{i+1}-\Phi_i) \quad \text{with}$$
$$I = \begin{cases} i-1 & \text{if} \quad u > 0 \\ i+1 & \text{otherwise} \end{cases}$$

Chapter 5 discusses among other aspects how different choices of the limiter function affect turbulence statistics in simulations of the smoke cloud boundary layer.

3.2.3 *Scalar diffusion in the UCLA-LES*

The diffusive tendency results from of the isolated diffusion problem

$$\int_V \rho_0 \frac{\partial \varphi}{\partial t}\,dV = -\oint_S (-\rho_{0,k}K_h\nabla\varphi\cdot\boldsymbol{n})\,dS$$

within the scalar transport equations (2.89) and (2.90). Again, φ represents either q_t or θ_l. As opposed to the explicit advection discretization, the UCLA-LES uses a directional-split semi-implicit scheme to discretize the diffusion problem which is of the form

$${}^{\text{diff}}L(\Phi^{(l)}) = -\frac{1}{\rho_{0,k}}\left[\frac{F^{(l)}_{i',j,k}-F^{(l)}_{i'-1,j,k}}{\Delta x} + \frac{G^{(l)}_{i,j',k}-G^{(l)}_{i,j'-1,k}}{\Delta y}\right] + \frac{\tilde{\Phi}^{(l+1)}_{ijk}-\Phi^{(l)}_{ijk}}{\Delta t} \quad . \tag{3.19}$$

The horizontal fluxes, F and G, are treated in an explicit fashion while the vertical diffusion is included as a tendency from the implicit vertical subproblem. (The intermediate variable $\tilde{\Phi}_{ijk}^{(l+1)}$ is the solution of the implicit problem.) This is advantageous if the vertical grid spacing is much smaller than the horizontal spacing, as is often done when simulating strongly stratified flows. By choosing an implicit scheme in the vertical, one can bypass the potentially severe stability constraint on the time step associated with small vertical grid spacings.

The explicit horizontal fluxes are approximated using the central scheme

$$F_{i'jk}^{(l)} = -\frac{\rho_{0,k} K_{h,i'jk}^{(l)}}{\Delta x}(\Phi_{i+1,j,k}^{(l)} - \Phi_{ijk}^{(l)}) \quad ,$$

where the eddy diffusivities K_h at the momentum points are linearly interpolated form the four neighbouring vertical momentum points according to

$$K_{h,i'jk}^{(l)} = \frac{1}{4}(K_{h,i,j,k'}^{(l)} + K_{h,i+1,j,k'}^{(l)} + K_{h,i',j,k'-1}^{(l)} + K_{h,i+1,j,k'-1}^{(l)}) \quad .$$

The same scheme is used in the y direction, which is obtained by switching the indices i and j and using Δy in place of Δx.

The implicit problem results from a balance of the vertical diffusive fluxes at time $t^{(l+1)}$. Since only the vertical direction is considered, one independent problem arises for each column i, j:

$$\tilde{\Phi}_k^{(l+1)} = \Phi_k^{(l)} - \frac{\Delta t}{\rho_{0,k}\Delta z_k}\left[H_{k'}^{(l+1)} - H_{k'-1}^{(l+1)}\right] \quad . \tag{3.20}$$

For brevity the indices i and j are omitted here and thereafter. With the vertical diffusive flux

$$H_{k'}^{(l+1)} = -\frac{\rho_{0,k'} K_{h,k'}^{(l)}}{\Delta z_{k'}}(\Phi_{k+1}^{(l+1)} - \Phi_k^{(l+1)})$$

and the abbreviations

$$\tau_k = \frac{\Delta t}{\rho_{0,k}\Delta z_{t,k}} \quad \text{and} \quad \sigma_{k'}^{(l)} = \frac{\rho_{0,k'} K_{h,k'}^{(l)}}{\Delta z_{k'}} \quad ,$$

one obtains the tridiagonal linear system

$$-\tau_k\sigma_{k'}^{(l)}\,\Phi_{k-1}^{(l+1)} + [1 + \tau_k(\sigma_{k'}^{(l)} + \sigma_{k'+1}^{(l)})]\,\Phi_k^{(l+1)} - \tau_k\sigma_{k'+1}^{(l)}\,\Phi_{k+1}^{(l+1)} = \Phi_k^{(l)} \quad . \tag{3.21}$$

Note that in order to decouple the implicit problem from the velocity field, the eddy diffusivity K_h is taken at the current RK time step $t^{(l)}$ allowing to explicitly evaluate it from the current time step data. The tridiagonal system is solved using the Thomas algorithm.

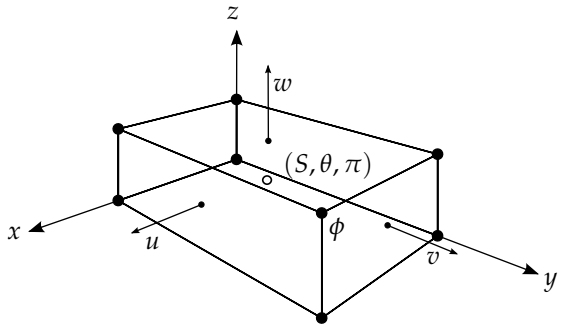

Figure 7: Sketch of a cell of the staggered grid. The prognostic variables are located at the cell centre (○), velocities are located at the cell faces (•⟶) and the level set scalar is located at the cell corners (•).

3.2.4 *Poisson solver*

The anelastic continuity equation (2.73) is obeyed by solving the Poisson equation for $\bar{\pi}$

$$\nabla \cdot (\rho_0 \nabla \bar{\pi}) = \frac{1}{c_p \Theta_0} \left[\nabla \cdot \left(- \nabla \cdot (\rho_0 \bar{\boldsymbol{v}} \otimes \bar{\boldsymbol{v}}) + \frac{\rho_0 \bar{\theta}' g}{\Theta_0} \boldsymbol{k} + \nabla \cdot (\rho_0 \boldsymbol{\tau}) \right) \right] . \quad (3.22)$$

which results from taking the divergence of the anelastic momentum equation, Eq. (2.70). The time derivative drops out according to the continuity equation. The solution is a new pressure field such that continuity is assued, i.e. $(\rho_0 \boldsymbol{v})$ is divergence free. The effect of the newly obtained dynamic pressure is directly applied applied to the velocities after each RK step.

Fourier decomposition in the two periodic directions is used to reduce the Poisson Eq. (5.7) to a second-order ordinary differential equation (ODE) in the vertical. The resulting ODE is solved directly to machine accuracy using a tridiagonal solver.

3.3 THE FRONT TRACKING ALGORITHM

This section discusses the numerical methods used to solve the equations associated with the level set method (LSM) (Sects. 3.3.1 to 3.3.3) and the modifications of the UCLA-LES necessary to couple the LSM to the flow solver (Sects. 3.3.4 to 3.3.6).

Many equations used in level set methods are first-order partial differential equations (PDEs), specifically the equations are of Hamilton-Jacobi (HJ) type

$$\frac{\partial \phi}{\partial t} + H \left(\frac{\partial \phi}{\partial x}, \frac{\partial \phi}{\partial y}, \frac{\partial \phi}{\partial z} \right) = 0 \quad . \quad (3.23)$$

Here H is the so called *Hamiltonian* which depends on the first derivatives of ϕ at most. Examples include the level set equation, Eq. (2.97), the reinitialization equation, Eq. (2.99), and the extrapolation equation, Eq. (2.103). Hamilton-Jacobi equations are related to hyperbolic conservation laws. In one dimension, it can be shown that the derivative of the solution of a HJ equation is the solution of a corresponding hyperbolic conservation law [50].

Although this analogy does not carry over to multiple dimensions, an important conclusion can be drawn: Since hyperbolic conservation laws can develop discontinuities from smooth initial conditions, HJ equations can develop kinks form initially smooth data [50]. Thus, numerical methods that yield the correct weak solution of HJ equations need to be used in cases where kinks can develop. Osher and Fedkiw [51] recommend Godunov's method to discretize the Hamiltonian which reduces to simple upwinding for linear problems.

3.3.1 *The level set method*

Recall that the evolution of the interface described by the level set is governed by the so-called level set equation, Eq. (2.97)

$$\frac{\partial \phi}{\partial t} + \boldsymbol{v}_\phi \cdot \nabla \phi = 0 \quad .$$

With the front-tracking algorithm it is discretized using finite-difference (FD) on the vertices of the finite-volume grid cells where ϕ is located (see Fig. 7). This location was chosen in order to allow for direct evaluation of the interface intersection points on the cell edges. The interface locations are later used to evaluate face fractions and volume fractions which is explained later in section 3.3.6.

The gradient in the advective term is discretized using a directionally-split upwind method based on second-order upwind polynomials. For example, the first spatial derivatives the x direction is approximated as

$$\left[\frac{\partial \phi}{\partial x}\right]_{i'} = \begin{cases} \frac{1}{2\Delta x'}(-1\phi_{i'-2} + 4\phi_{i'-1} - 3\phi_{i'}) & \text{if } u_{\phi,i'} \geq 0 \\ \frac{1}{2\Delta x'}(3\phi_{i'} - 4\phi_{i'-1} + 1\phi_{i'+2}) & \text{if } u_{\phi,i'} < 0 \end{cases} \tag{3.24}$$

where indices j' and k' have been dropped for convenience. The approximations in the other two dimensions are the same with indices and velocity components changed accordingly. The velocities at the cell corners—$u_{\phi,i'j'k'}$, $v_{\phi,i'j'k'}$, and $w_{\phi,i'j'k'}$—are linearly interpolated from the LES velocity field according to

$$\begin{aligned} u_{\phi,i'j'k'} = {} & \frac{1}{2}(u_{ijk} + u_{i,j+1,k}) \\ & + \frac{1}{4}\frac{\Delta z_k}{\Delta z_{k'}}(u_{i,j,k+1} + u_{i,j+1,k+1} - u_{ijk} - u_{i,j+1,k}) \quad . \end{aligned} \tag{3.25}$$

The same equation is used for the v_ϕ velocity component, with indices i and j exchanged. The vertical velocities are interpolated using the slightly simpler expression

$$w_{\phi,i'j'k'} = \frac{1}{4}(w_{ijk} + w_{i+1,j,k} + w_{i+1,j+1,k} + w_{i,j+1,k}) \tag{3.26}$$

since the grid is guaranteed to be uniform in the lateral directions in the UCLA-LES. The level set equation (2.97) is evolved in time using the same third-order RK scheme as used for the other variables (see Eqs. (3.12) to (3.14)).

3.3.2 *Level set reinitialization*

In order to maintain the signed-distance property of the level set scalar ϕ, it is frequently reinitialized using the reinitialization equation, Eq. (2.99)

$$\frac{\partial \phi}{\partial \tau} = \text{sign}(\tilde{\phi})(1 - |\nabla \phi|) \quad ,$$

which can be restated as the hyperbolic transport equation (2.100)

$$\phi_\tau + \text{sign}(\tilde{\phi})\boldsymbol{n} \cdot \nabla \phi = \text{sign}(\tilde{\phi})$$

As pointed out earlier, the hyperbolic nature of this equation also suggests that Godunov schemes ought to be used that minimize the numerical displacement of the zero level set during reinitialization.

Sussman et al. [82] propose a Godunov scheme which reads, extended to three dimensions,

$$\phi^{n+1}_{i'j'k'} = \phi^n_{i'j'k'} - \Delta\tau S(\tilde{\phi}_{i'j'k'}) G^n_{i'j'k'} \quad , \tag{3.27}$$

where

$$S(\tilde{\phi}) = \frac{\tilde{\phi}}{\sqrt{\tilde{\phi}^2 + \epsilon^2}} \tag{3.28}$$

is a smoothed sign function with e.g. $\epsilon = \Delta x$, and

$$G_{i'j'k'} = \begin{cases} \sqrt{\max(a_+^2, b_-^2) + \max(c_+^2, d_-^2) + \max(e_+^2, f_-^2)} - 1 & \text{if } \phi_{i'j'k'} > 0 \\ \sqrt{\max(a_-^2, b_+^2) + \max(c_-^2, d_+^2) + \max(e_-^2, f_+^2)} - 1 & \text{if } \phi_{i'j'k'} < 0 \\ 0 & \text{otherwise.} \end{cases} \tag{3.29}$$

is the Godunov Hamiltonian. The variables a to f are the backward and forward differences

$$a = \frac{\phi_{i'j'k'} - \phi_{i'-1,j',k'}}{\Delta x} \qquad b = \frac{\phi_{i'+1,j',k'} - \phi_{i'j'k'}}{\Delta x}$$
$$c = \frac{\phi_{i'j'k'} - \phi_{i',j'-1,k'}}{\Delta y} \qquad d = \frac{\phi_{i',j'+1,k'} - \phi_{i'j'k'}}{\Delta y}$$
$$e = \frac{\phi_{i'j'k'} - \phi_{i',j',k'-1}}{\Delta z_k} \qquad f = \frac{\phi_{i',j',k'+1} - \phi_{i'j'k'}}{\Delta z_k}$$

and the subscripts $+$ and $-$ denote their positive and negative parts, e.g $a_+ = \max(a, 0)$ and $a_- = \min(a, 0)$.

Russo and Smereka [56] note that applying this method may considerably displace the location of the interface towards the closest grid node, which they attribute to the choice of the discretization stencil. On points adjacent to the interface, Sussman et al.'s [82] method would discretize $|\nabla\phi|$ across the interface, locally—only on these points—violating the upwind principle. Russo and Smereka [56] propose a modification, called the *subcell fix*, making the method strictly upwind by approximating $|\nabla\phi|$ based on geometrical considerations in points adjacent to the interface. Their modified scheme reads

$$\phi^{n+1}_{i'j'k'} = \begin{cases} \phi^n_{i'j'k'} - \frac{\Delta\tau}{\Delta x}(S(\tilde{\phi}_{i'j'k'})|\phi^n_{i'j'k'}| - d_{i'j'k'}) & \text{if } \phi_{i'j'k'}\hat{\phi}_{i'j'k'} < 0,\ \forall \hat{\phi}_{i'j'k'} \in \mathcal{N}_{i'j'k'} \\ \phi^n_{i'j'k'} - \Delta\tau S(\tilde{\phi}_{i'j'k'}) G^n_{i'j'k'} & \text{otherwise} \end{cases}$$

(3.30)

where the set

$$\mathcal{N}_{i'j'k'} = \{\phi_{i'+1,j',k'}, \phi_{i'-1,j',k'}, \phi_{i',j'+1,k'}, \phi_{i',j'-1,k'}, \phi_{i',j',k'+1}, \phi_{i',j',k'-1}\} \quad (3.31)$$

contains all neighbours of $\phi_{i'j'k'}$, and

$$d_{i'j'k'} = \frac{\tilde{\phi}_{i'j'k'}}{\sqrt{[\phi_x]^2_{i'j'k'} + [\phi_y]^2_{i'j'k'} + [\phi_z]^2_{i'j'k'}}} \quad (3.32)$$

is an approximation to the signed distance function to the interface. Note that since d and the smooth sign function S only depend on the initial ϕ field, the only have to be evaluated once per large-eddy simulation (LES) time step. Russo and Smereka [56] showed (i) that the subcell fix greatly reduces the spurious displacement of the interface, and (ii) that the maximum displacement error is independent of the number of iterations.

In the present work, the subcell-fix method is used with one modification. Russo and Smereka [56] propose to use central differences to approximate the spatial derivatives in Eq. (3.32). However, Hartmann et al. [23] showed that using central differences in this instance may lead to oscillations of the interface where it is tightly curved and propose a mixed upwind/central discretization scheme which yields smooth results in these situations. Hartmann et al.'s scheme uses only points adjacent to the interface, i.e. whenever the central stencil reaches out of the set of adjacent points, it is reduced to a one-sided stencil towards the interface.

As mentioned above, the straight-forward way to reinitialize ϕ into signed-distance state is to compute the shortest distance to the interface and set ϕ equal to that value for every grid point. Consider a 3D grid with N^3 grid points. The number of discrete points of a 2D surface in 3D space scales as N^2 and, thus, computing the shortest distance at a given point requires work C_1N^2, where the constant C_1 accounts for additional points due to undulations of the interface as well as the number of floating-point operations needed to compute the distance to one interface point. Then, the required work for directly reinitializing at every grid point is $C_1N^2N^3 = C_1N^5$. In other words, this algorithm had the complexity $\mathcal{O}(N^5)$.

If instead of the direct method, a PDE such as Eq. (2.99) is used, the computational cost can potentially be drastically reduced. Given that in this equation information travels at speed 1 and perpendicular to the interface, C_2N iterations are needed for an iterative method to propagate information across the entire domain. The computational work for reinitialization scales as $N^2 * C \times \mathit{iterations}$, giving the complexity $\mathcal{O}(N^2)$.

The direct algorithm can be improved by confining the computation to a small band around the interface, which reduces the complexity by one order to $\mathcal{O}(N^4)$.

3.3.3 *Interface boundary conditions*

The interface boundary conditions are realized by two-sided extrapolation using Fedkiw et al.'s [18] *ghost fluid method* as described in Sect. 2.2.4. For this, for each scalar two HJ-type equations of the form of Eq. (2.103) are iterated in virtual time τ, one on each side of the interface. After the process, there are two fluids present on both sides of the interface: one physical fluid and one ghost.

Take for example the generation of the ghost fluid of a scalar φ in the top region. For this, the notation of Eqs. (2.93) to (2.95) is carried over into the discrete sense: The set of cut cells is denoted as Ω_0, the set of cells for which all $\phi > 0$ as Ω_+, and the set of cells for which all $\phi < 0$ as Ω_-. First, the physical field φ is copied to a new one, φ_0, serving as initial condition. Then, in the top region $(\Omega_0 \bigcup \Omega_+)$, i.e. in all cut cells and the uncut cells above the interface, we iterate the extrapolation equation

$$\frac{\partial \varphi_0}{\partial \tau} + \boldsymbol{n} \cdot \nabla \varphi_0 = 0 \tag{3.33}$$

in virtual time τ with the values in Ω_- serving as Dirichlet boundary conditions. Having defined ϕ so it is positive above the interface, this carries information at speed 1 from the bottom upwards. After the process, the field φ_0 contains physical values of φ in Ω_- and ghost values in $(\Omega_0 \bigcup \Omega_+)$. The process is then repeated in $(\Omega_0 \bigcup \Omega_-)$ to generate φ_1 from another copy of φ. The only difference is that the plus sign in Eq. (3.33) is inverted to a minus sign so information travels from the top downwards. As a result, there are two scalar fields for each scalar φ, φ_0 and φ_1, both of which consist of physical fluid on one side of the interface and ghost fluid on the other side. The index signifies the origin of the ghost information: Index 0 (zero) stands for "originating from the bottom", and index 1 stands for "originating from the top" (see the top Fig. 8).

Equation (3.33) is discretized using the Euler method and with the first-order upwind FD scheme

$$\begin{aligned}
\Phi^{n+1}_{0,ijk} = \Phi^{n}_{0,ijk} - \Delta t \Big(& \min(n_{x,ijk}, 0)\, \frac{\Phi^{n}_{0,i+1,j,k} - \Phi^{n}_{0,ijk}}{\Delta x} \\
& + \max(n_{x,ijk}, 0)\, \frac{\Phi^{n}_{0,ijk} - \Phi^{n}_{0,i-1,j,k}}{\Delta x} \\
& + \min(n_{y,ijk}, 0)\, \frac{\Phi^{n}_{0,i,j+1,k} - \Phi^{n}_{0,ijk}}{\Delta y} \\
& + \max(n_{y,ijk}, 0)\, \frac{\Phi^{n}_{0,ijk} - \Phi^{n}_{0,i,j-1,k}}{\Delta y} \\
& + \min(n_{z,ijk}, 0)\, \frac{\Phi^{n}_{0,i,j,k+1} - \Phi^{n}_{0,ijk}}{\Delta z_{k'}} \\
& + \max(n_{z,ijk}, 0)\, \frac{\Phi^{n}_{0,ijk} - \Phi^{n}_{0,i,j,k-1}}{\Delta z_{k'}} \Big) \quad ,
\end{aligned} \tag{3.34}$$

where n_x, n_y, and n_z, are components of the interface normal vector discretized using central differences. For instance, the component in x direction is discretized using

$$n_{x,ijk} = \frac{[\phi_x]_{ijk}}{\sqrt{[\phi_x]^2_{ijk} + [\phi_y]^2_{ijk} + [\phi_z]^2_{ijk}}} \quad , \tag{3.35}$$

where $[\phi_x]_{ijk}$, $[\phi_y]_{ijk}$, and $[\phi_z]_{ijk}$, are the central difference approximations to the partial derivatives of ϕ on the thermal points according to

$$\begin{aligned}
[\phi_x]_{ijk} = \frac{1}{4\Delta x} \big(& \phi_{i'j'k'} - \phi_{i'-1,j',k'} + \phi_{i',j'-1,k'} - \phi_{i'-1,j'-1,k'} \\
& + \phi_{i',j',k'-1} - \phi_{i'-1,j',k'-1} + \phi_{i',j'-1,k'-1} - \phi_{i'-1,j'-1,k'-1} \big) \quad .
\end{aligned} \tag{3.36}$$

The difference equations for the derivatives in the other two directions follow from appropriately modifying the grid spacing and indices.

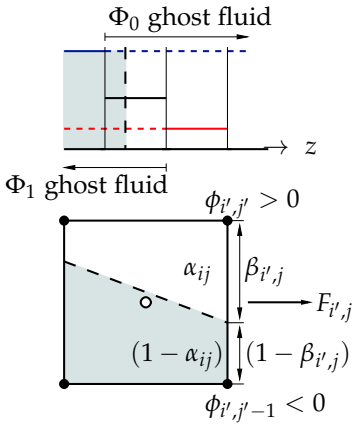

Figure 8: Sketch of a cut cell to illustrate the ghost fluid method (top) and flux superposition (bottom). The dashed line indicates the location of the interface. Shaded regions are immersed in smoke. The primed indices abbreviate $i' = i + 1/2$ and $j' = j + 1/2$. The symbol Φ denotes an arbitrary scalar, such as in case of the STBL liquid water potential temperature θ_l or the total water mixing ratio q_t.

3.3.4 *Level set/advection coupling*

So far, the evolution of the prognostic variables and the level set function are coupled only one-way, i.e. the level set is passively advected with the flow. In order to couple the evolution of the prognostic variables with the level set, we follow the concept by Smiljanovski et al. [69]. In their compressible framework, they used a level set method to track the position of a flame front, and they used Rankine-Hugoniot jump conditions to supply internal boundary conditions at the interface. The reconstruction allows for computing fluxes and source terms associated with the two states present in a cut cell individually. The individual fluxes and source terms can then be superimposed to obtain the net effect in the particular cell. In the present anelastic system, only the latter part of the approach is retained and Fedkiw's et al. [18] ghost fluid method is used to supply internal boundary conditions.

Following Smiljanovski et al.'s approach, fluxes of a scalar Φ caused by boundary layer (BL) fluid, $F(\Phi_0)$, and those caused by fluid of the free atmosphere, $F(\Phi_1)$, are computed individually. The net flux of Φ, say in the x direction, is then obtained as the weighted sum

$$F_{i'j}(\Phi) = (1 - \tilde{\beta}_{i'j})\ F_{i'j}(\Phi_0)\ +\ \tilde{\beta}_{i'j}\ F_{i'j}(\Phi_1) \quad , \tag{3.37}$$

where the $\tilde{\beta}_{i'j}$ are the face fractions at the respective cell face (see Fig. 8) time-averaged over one LES time step. With this approach, the same flux scheme can be used both at the interface as well as in the interior of the flow. No special treatment for cut cells is necessary.

In the UCLA-LES, this concept is implemented in two steps where the contribution of each fluid is computed separately and added to the scalars ten-

dency. That is, for the fluid of the free atmosphere, the rate of change in the original UCLA-LES, Eq. (3.15), is modified to

$$
\begin{aligned}
{}^{\text{adv}}\tilde{L}^{(l)}_{ijk}(\Phi_1,\Delta t) = -\frac{1}{\rho_k}\Bigg[& \frac{\bar\beta^x_{i'jk}F^{(l)}_{i'jk} - \bar\beta^x_{i'-1,j,k}F^{(l)}_{i'-1,j,k}}{\Delta x} && (3.38)\\
& + \frac{\bar\beta^y_{ij'k}G^{(l)}_{ij'k} - \bar\beta^y_{i,j'-1,k}G^{(l)}_{i,j'-1,k}}{\Delta y} && (3.39)\\
& + \frac{\bar\beta^z_{ijk'}H^{(l)}_{ijk'} - \bar\beta^z_{i,j,k'-1}H^{(l)}_{i,j,k'-1}}{\Delta z_k}\Bigg] \quad . && (3.40)
\end{aligned}
$$

The rate of change due to the BL fluid is computed accordingly by using the Φ_0 field instead and $(1-\bar\beta)$ in place of $\bar\beta$. The advective fluxes F, G, and H are discretized using LeVeque's scheme (3.18) which is mathematically equivalent with the UCLA-LES scheme, as noted in Sect. 3.2.2.

3.3.5 *Level set/diffusion coupling*

Similar to the advective parts, the coupled diffusion scheme is obtained by superimposing the diffusive fluxes of both ghost fluids weighted by their face fractions

$$
\begin{aligned}
{}^{\text{diff}}L^{(l)}_{ijk}(\Phi_1,\Delta t) = -\frac{1}{\rho_k}\Bigg[& \frac{\bar\beta^x_{i'jk}F^{(l)}_{i'jk} - \bar\beta^x_{i'-1,j,k}F^{(l)}_{i'-1,j,k}}{\Delta x} && (3.41)\\
& + \frac{\bar\beta^y_{ij'k}G^{(l)}_{ij'k} - \bar\beta^y_{ij'-1k}G^{(l)}_{i,j'-1,k}}{\Delta y}\Bigg] && (3.42)\\
& + \frac{\tilde\Phi^{n+1}_{ijk} - \Phi^n_{ijk}}{\Delta t} \quad . && (3.43)
\end{aligned}
$$

In order to derive the equations to be solved for the implicit vertical problem, it is helpful and more concise to consider the differential form of the 1D diffusion equation. For the anelastic system this is

$$
\frac{\partial(\alpha\varphi_1 + (1-\alpha)\varphi_0)}{\partial t} = -\frac{1}{\rho_0}\frac{\partial\left(\beta h(\varphi_1) + (1-\beta)h(\varphi_0)\right)}{\partial z} \quad , \tag{3.44}
$$

where the φ and its diffusive flux $h(\varphi)$ was expanded using

$$
\begin{aligned}
\varphi &= \alpha\varphi_1 + (1-\alpha)\varphi_0 \qquad \text{and}\\
h(\varphi) &= \beta h(\varphi_1) + (1-\beta)h(\varphi_0) \quad . && (3.45)
\end{aligned}
$$

By requiring that the fluxes of fluid 1 to have no effect on fluid zero and vice versa, the equation can be split into the two equations

$$
\begin{aligned}
\alpha\,\frac{\partial\varphi_1}{\partial t} &= -\frac{1}{\rho_0}\frac{\partial\left(\,\beta\,h(\varphi_1)\right)}{\partial z} \quad , && (3.46)\\
(1-\alpha)\,\frac{\partial\varphi_0}{\partial t} &= -\frac{1}{\rho_0}\frac{\partial\left(\,(1-\beta)\,h(\varphi_0)\right)}{\partial z} \quad . && (3.47)
\end{aligned}
$$

Here, it is assumed that diffusion does not change the location of the interface, i.e. $\partial\alpha/\partial t = 0$. Since both equations are equivalent, the first one will be used to illustrate the numerical scheme to solve them. Discretizing

Eq. (3.46) using the FV method and integrating from t^n to $t^{n+1} = t + \Delta t$ yields the scheme

$$\alpha_k \rho_{0,k} \Phi_k^{n+1} = \alpha_k \rho_{0,k} \tilde{\Phi}_k^n - \frac{\Delta t}{\Delta z_k} \left[H_{k'}^{n+1} - H_{k'-1}^{n+1} \right]$$

with the flux

$$H_{k'} = \frac{(\rho_0 \bar{\beta}^n K_h^n)_{k'}}{\Delta z_{k'}} \left(\Phi_{k+1}^{n+1} - \Phi_k^{n+1} \right) \quad .$$

Here, the index of Φ, indicating the current fluid was omitted for brevity. Using the abbreviations

$$\tau_i = \frac{\Delta t}{\Delta z_k} \quad \text{and} \quad \sigma_{k'} = \frac{(\rho_0 \bar{\beta}^n K_h^n)_{k'}}{\Delta z_{k'}}$$

the system can be rewritten as

$$-\tau_i \sigma_{k'-1} \Phi_{k-1}^{n+1} + \left[\alpha_i \rho_{0,k} + \tau_i (\sigma_{k'-1} + \sigma_{k'}) \right] \Phi_k^{n+1} - \tau_i \sigma_{k'} \Phi_{k+1}^{n+1} = \alpha_i \rho_{0,k} \Phi_k^n \quad . \tag{3.48}$$

This scheme is similar to the original implicit diffusion scheme (3.21) except that the scalar concentration is scaled by the available partial volume α and that the diffusivity is limited by the current face fraction $\bar{\beta}$. As with advection, the corresponding scheme for the BL fluid is obtained by using Φ_0 field instead and $(1 - \bar{\beta})$ in place of $\bar{\beta}$.

Note, that the current implementation does not allow for breaking waves at the interface. The algorithm assumes that there are exactly two separate implicit vertical problems. If waves are allowed to break, the interface separates the column in a multiple of two implicit diffusion problems which have to be isolated and solved individually.

3.3.6 *Face fractions and volume fractions*

The FV schemes above are complete once the volume fractions α and face fractions β are supplied. This section formally defines these quantities and describes how they are numerically integrated und in the UCLA-LES.

The volume and face fractions can be conveniently defined as the integrals

$$\alpha = \frac{1}{V} \int_{(V)} H(\phi) \, dV \quad \text{and} \quad \beta = \frac{1}{A} \int_{(A)} H(\phi) \, dA \quad . \tag{3.49}$$

over the Heaviside function

$$H(\phi) = \begin{cases} 1 & \text{if} \quad \phi \geq 0 \\ 0 & \text{if} \quad \phi < 0 \end{cases} \quad , \tag{3.50}$$

where V and A are the volume of the respective grid cell and the area of a grid face, respectively. According to this definition, $\alpha = \beta = 1$ in the free atmosphere, $\alpha = \beta = 0$ inside the BL, and assume values in between for cut cells or faces, respectively.

First the 2D case is considered, i.e. the integration of face fractions β. For every RK step, the six face fractions of all cells are initialized to

$$\beta_{\text{init}} = \frac{1}{2}(1 + \text{sign}(\phi_{ijk})) \quad . \tag{3.51}$$

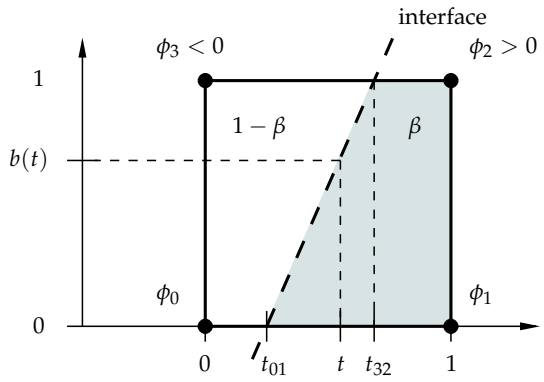

Figure 9: Sketch of a cut cell face with the face fraction β shaded in grey. The interface (– –) defines a piecewise linear cross section function function, $b(t)$, with $b(t) = 0$ for $t < t_{01}$ and $b(t) = 1$ for $t > t_{32}$.

Then, the values of all cut faces are overwritten by the actual intermediate value, which is computed as follows.

First, consider an arbitrary axis t parallel to one of the cell edges of the respective face. Along this axis, an ordered sequence of points is established, where the zero level set intersects either of the two edges parallel to t. The sequence also includes the start and end points (see Fig. 9). Then, a piecewise linear cross section function, $b(t)$, is constructed that interpolates the cross section at each of the intersection points. Both $b(t)$ and t are normed by the dimensions of the grid cell, i.e.

$$0 \leq b(t) \leq 1, \quad \forall t \in [0,1] \quad .$$

The integrals in Eqs. (3.49) can now be approximated as integrals over the cross section function $b(t)$. That is, the face fraction can be computed as

$$\beta = \int_{t=0}^{1} b(t)\, dt \quad . \tag{3.52}$$

The piecewise linear function $b(t)$ can be integrated exactly as is shown nn the following. This procedure corresponds to the quadrature of the unknown exact cross section using the trapezoidal rule. Given a cut cell face having the ϕ values ϕ_0 to ϕ_3 at its vertices, as shown in Fig. 9, the code chooses (arbitrarily) the main integration direction t. Along this axis, there are two intersection points in the most general case, denoted by t_{01} and t_{32}, that partition the cell in three sections. The intersection points are the roots of the linear interpolants of ϕ along the top and bottom edge:

$$t_{01} = \begin{cases} -\frac{\phi_0}{\phi_1 - \phi_0} & \text{if} \quad \phi_0 \phi_1 < 0 \\ 1 & \text{else} \end{cases} \tag{3.53}$$

and

$$t_{32} = \begin{cases} -\frac{\phi_3}{\phi_2 - \phi_3} & \text{if} \quad \phi_3 \phi_2 < 0 \\ 1 & \text{else} \end{cases} \quad . \tag{3.54}$$

Their corresponding cross sections are based on the linear reconstruction of ϕ along the bottom (ϕ_{01}) and top edge (ϕ_{32}), respectively,

$$\phi_{01}(t_i) = \phi_0 + t_i(\phi_1 - \phi_0) \tag{3.55}$$

$$\phi_{32}(t_i) = \phi_3 + t_i(\phi_2 - \phi_2) \quad . \tag{3.56}$$

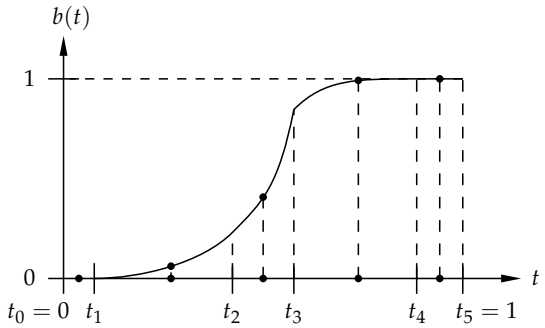

Figure 10: Polynomial reconstruction of the cross section of a grid cell from uncut, to partially immersed, to fully immersed in the free atmosphere.

and are given by

$$b = \begin{cases} -\frac{\phi_{01}}{\phi_{32}-\phi_{01}} & \text{if} \quad \phi_{01}\phi_{32} < 0 \quad \text{and} \quad \phi_{32} < 0 \\ -\frac{\phi_{32}}{\phi_{01}-\phi_{32}} & \text{if} \quad \phi_{01}\phi_{32} < 0 \quad \text{and} \quad \phi_{32} \geq 0 \\ H(\phi_{01}) & \text{else} \end{cases} \tag{3.57}$$

The integral of the piecewise linear cross section function gives the face fraction

$$\beta = \sum_{i=1}^{3} \frac{1}{2}(t_{i+1} - t_i)\,(b_{i+1} + b_i) \quad . \tag{3.58}$$

Here, t_i contains the intersection points in ascending order

$$t_i = \begin{pmatrix} 0 \\ \max[0, \min(t_{01}, t_{32}) - \epsilon] \\ \min[1, \max(t_{01}, t_{32}) + \epsilon] \\ 1 \end{pmatrix} \quad . \tag{3.59}$$

and $b_i = b(t_i)$ contains the corresponding cross sections and ϵ is choosen to be 10^{-15}.

Volume fractions are integrated in the same fashion with only three major differences. The first one is the dimension of the cross sections. In 2D, the cross section function $b(t)$ is a line fraction; in the 3D case it is an area fraction. The area fractions are computed using the face fractions algorithm described above.

The second one is the possible number of intersection points. In 2D, t_i has at most four components including the start and end values; in the 3D case, t_i may have up to six components. These include up to four intersection points for the four edges and the start and end values.

The third difference is that quadratic interpolation is used to establish the cross section function $b(t)$. In the 2D case, the cross section changes linearly with linearly-changing ϕ values along edges. In contrast, cross sections in the 3D case may change quadratically with linearly changing ϕ. For instance, if the partial volume is a (clipped) three-sided pyramid, its triangular cross section changes as the square of t.

The most general case is shown in Fig. 10, there are four intersection points along an arbitrary axis t, that divide the cell in five segments. First, the sequence of the points t_0 to t_5 is established, as well as the corresponding cross sections $b_i = b(t_i)$. Then, in every of the five cell segments, the the cross

section is interpolated by the quadratic polynomial and the volume fraction is given by the sum of the integrals over all five polynomials

$$\alpha = \sum_{i=1}^{5} \int_{t=t_{i-1}}^{t_i} b_i(t)\, dt \quad . \tag{3.60}$$

In order to determine each polynomial, an additional b value at the midpoint of each segment is computed. Four linear reconstructions of ϕ along the respective edges (cf. Eq. (3.55)) supply the values at the midpoints. The face fraction algorithm above is then used to evaluate the corresponding cross section. With three cross sections $b_{i\{1,2,3\}}$, the polynomial

$$b_{ij} = a_{0j} + a_{1j} t_j + a_{2j} t_j^2, \quad j \in 1,2,3 \tag{3.61}$$

is fully defined. The coefficients a_0 to a_2 are obtained by solving the inverse 3×3 problem. With the exact integrals over the obtained polynomials, Eq. (3.60) becomes

$$\alpha = \sum_{l=1}^{5} a_{l0}(t_{l1} - t_{l0}) + \frac{a_{l1}}{2}(t_{l1} - t_{l0})^2 + \frac{a_{l2}}{3}(t_{l1} - t_{l0})^3 \quad . \tag{3.62}$$

The implemented quadrature deviates under certain conditions from the presented methodology in order to avoid errors due to fixed numerical precision. The exceptions are:

- Segments with $(t_{i+1} - t_i) < 10^{-6}$ are neglected.
- Linear interpolation is used instead of quadratic interpolation in segments where the magnitude of the determinant of matrix a_{ij} in Eq. (3.61) is less than 10^{-12}.

The UCLA-LES implementation of the presented methodology is a Fortran adaptation of the original C code by Schmidt and Klein [61]. The same methodology as for α is implemented to compute the time-average $\tilde{\beta}$, but linear interpolation is used in all segments.

3.3.7 *Level set synchronisation*

An interesting detail of the method is its overdetermination in terms of how the interface is described. By introducing the level set equation, Eq. 2.97, one more equation describing the evolution of the interface is added which, in terms of this information, is redundant with the scalar transport equations. If the location of the interface ϕ_0 and the resulting volume fractions and face fractions are not synchronised with the interface location represented by the scalar fields, errors in the form of overshoots and undershoots may accumulate to leading order.

One approach to resolve this redundancy is to combine the level set method with volume-of-fluid techniques. Schneider [63] formulates a correction method in terms of an elliptical equation connecting all cells along the interface. The solution of the elliptical equation are corrections of the face fractions to be used in Eq. (3.37) which distribute the corrections along the cut cells. Similar techniques are subject of current research ([87]).

A second way is to let the level set govern the location of the interface and reassign cell averages in cells cut during an LES time step according to the current volume fraction given by ϕ_0, that is for an arbitrary scalar Φ:

$$\Phi_{\text{cut}} = \alpha_{\text{cut}} \Phi_1 + (1 - \alpha_{\text{cut}}) \Phi_0 \tag{3.63}$$

Here, $\Phi_{0,1}$ are the extrapolated fields as discussed in Sect. 3.3.3. The method is local and, thus, computationally simpler than the first approach. However, note that this correction method is not globally conservative. For instance, in the smoke cloud simulations presented in Chapt. 5, the maximum mass change was +1.4% and +0.8% in the low and high resolution cases, respectively.

4

LOW-ORDER NUMERICAL EFFECTS IN THE TWO-DIMENSIONAL CLOUD-TOP MIXING LAYER

The results presented in this chapter have previously been published in

[15] Dietze, E., Mellado, J. P., Stevens, B., & Schmidt, H. (2013). Study of low-order numerical effects in the two-dimensional cloud-top mixing layer. *Theoretical and Computational Fluid Dynamics*, 27(3-4), pp. 239-251. Springer Berlin / Heidelberg. doi:10.1007/s00162-012-0263-0.

4.1 INTRODUCTION

In chapter 1, two sources of errors where identified that challenge our ability to simulate the stratocumulus-topped boundary layers (STBLs) using large-eddy simulation (LES): the first one is related to physics, the other one to numerics. The physical one is the lack of an accurate representation of the small-scale turbulent mixing in traditional subgrid models. Especially in the vicinity of the cloud-top interface, turbulence is anisotropic and partially caused by small-scale fluctuations due to convective instabilities, both of which are not appropriately modelled. The second, numerical source is insufficient grid resolution to resolve the strong gradients at the cloud top. This chapter explores the effect of the latter error source on the solution for a case (i) that is relevant to the cloud-top problem and (ii) where an accurate solution is known.

For this, the behaviour of the University of California, Los Angeles Large-Eddy Simulation (UCLA-LES) [74, 75, 79] as a typical LES numerical algorithm is investigated simulating Mellado et al.'s [42] two-dimensional cloud-top mixing problem and their direct numerical simulation (DNS) solution is used as a reference. This particular case is explored because it embodies a number of important features of the STBL relevant to cloud-top entrainment such as a stably oscillating inversion, molecular diffusion, baroclinic production of vorticity, and evaporative cooling leading to buoyancy reversal.

In the LES, the subgrid-scale (SGS) model was switched off and a constant molecular viscosity was introduced. (It is emphasized that in this chapter, the term LES will be used solely to refer to the UCLA-LES numerical algorithm. Where, in contrast, LES modelling is meant it will be clear from the context.) The reference DNS uses a 6th-order compact scheme in space whereas in LES low-order methods are commonly used, typically 2nd-order as in this study. The emphasis on lower order on LES scales arises because the flow is not smooth on the grid scale; thereby obviating the advantages of higher-order methods. Low-order methods also use a smaller stencil and thus are more easily to implement efficiently in a highly parallel environment.

It is analyzed how sensitive solutions are to numerical errors and what the resolution requirements are as compared to a high-order DNS solver. For that, a grid convergence study is carried out where the computational grid is systematically refined the until convergence is achieved. By doing that, the UCLA-LES code is also verified for the test case. Because the choice of high- versus low-order methods often involves trade-offs, it is also investigated how the computational costs of both codes compare.

4.2 BUOYANCY REVERSAL AND THE CLOUD-TOP ENTRAINMENT INSTABILITY

The main processes that drive entrainment are (i) radiative cooling, (ii) shear due to large-scale boundary layer vortices, and (iii) evaporative cooling. Above the cloud top of subtropical marine stratocumulus, the environment is relatively warm and dry, as it is characteristic of the large-scale environment of subsiding air in which the STBL prevails. The STBL itself is more characteristic of the underlying ocean surface in that it is much cooler and moister, and as the name indicates, cloud-topped. On the one hand, warmer air that is mixed into a cloud-top parcel raises its temperature. On the other hand, because the warmer air is drier, evaporation takes place which cools the mixture. Both effects compete and if the latter dominates, mixtures can develop that are heavier than either one of the two unmixed states. This effect is known as buoyancy reversal [68, 90], that in this case is caused by evaporative cooling. In past studies of this problem the influence of effects at the molecular scale and below have largely been ignored; these include droplet dynamics, phase changes and molecular mixing. The question whether buoyancy reversal alone can cause a runaway instability by positive feedback of evaporative cooling, mixing, and entrainment leading to cloud break-up [13, 55]—the so called cloud-top entrainment instability (CTEI)—has long been debated. The strength of the reversal is typically expressed by the buoyancy reversal parameter $D = -b_s/b_1$ [68], that relates minimum and maximum buoyancy b_s and b_1, respectively. This parameter is typically small. For instance, in the first research flight (RF01) of the DYCOMS II field study [78] a buoyancy reversal parameter of $D = 0.031$ was measured.

Large-eddy simulations have been extensively used as a tool to improve understanding of the processes at the cloud-top. Unfortunately, even LESs currently have, and in the foreseeable future will have, insufficient grid resolution to resolve the cloud top and the small-scale mixing processes which give rise to buoyancy reversal. High-resolution methods, which allow for a representation of molecular effects, have been used to improve the understanding of the entrainment mechanism. Examples include, one-dimensional stochastic models such as the linear eddy model [28] and the one-dimensional turbulence model [90] but also DNS, based on the Boussinesq approximation and a continuous two-fluid formulation [40]. Mellado et al. [42] show by means of two-dimensional DNS that complex flow patterns can be generated by weak buoyancy reversal typical for stratocumulus. The DNS also shows that the turbulent mixing dominates the downward development of the cloudy layer and that there is no significant enhancement of turbulent entrainment of upper fluid in the shear-free case. Furthermore, linear stability analysis identifies two time scales: the time scale associated with the downdraughts of heavy fluid due to buoyancy reversal and the time scale of the restoring force of the inversion. The ratio between both is $\sqrt{D}$ and the conjecture is that for typical conditions ($0 < D \ll 1$) buoyancy reversal alone can not dissipate the cloud because the inversion returns to equilibrium much faster than the time required by downdraughts to descend deep enough into the cloud layer. Three-dimensional DNS [44] confirm this conjecture. In the simulation buoyancy reversal promotes convection leading to turbulence with an intensity that is too weak to overturn the inversion. The system evolves into a self-preserving state that retains the vertically layered structure. Above the convection layer a thin diffusion layer with a constant thickness $h = \kappa/w_e$ forms and travels upwards at a constant

mean speed $w_e \sim (\kappa|b_s\chi_c^2)^{1/3}$, where κ is the molecular diffusivity and χ_c is the cross-over mixture fraction, equal to the interval of negatively buoyant mixtures. Analysis of the budgets of turbulent kinetic energy shows that a strong conversion of horizontal to vertical momentum occurs in a thin region between the inversion layer and the convection layer [40, 44]. Probability density functions of velocity in the turbulent region show a strong vertical variability and often non-Gaussian behaviour, even in the horizontal component [45]. This indicates strong anisotropy and inhomogeneity of the turbulence which, in addition to the relevance of molecular transport, further complicates turbulence modelling in LES for this kind of flows.

4.3 FORMULATION

4.3.1 *Reference problem*

The system considered consists of two layers: A cold moist layer, which is saturated and has liquid water is topped by a relatively warmer, drier layer. In the mixing region between the two layers the total water mixing ratio q_t and specific enthalpy h transition between the two values characteristic of the upper unsaturated and lower saturated layer respectively. Initially, the system is at rest, gravity acting downwards. The system so defined is a simplified surrogate of the stratocumulus top in order to investigate the physical phenomena associated with relatively small-scale dynamics.

The multiphase flow is described using the two-fluid formulation presented in Sect. 2.1. The main underlying hypotheses were the following: (i) The liquid water can be considered a continuous phase, (ii) the mixture always stays in local thermodynamic equilibrium, and (iii) the diffusivity of the liquid phase equals that of dry air and water vapour. Assuming equal thermal and mass diffusivities, the thermodynamic coordinates h and q_t obey the same advection-diffusion equation. This implies that, with appropriate boundary conditions, both quantities have the same normalized solution after an initial transient. Thus, their evolution can be described by that of a single conserved scalar – the mixture fraction χ. With the indices 0 (zero) and 1 indicating the states in the lower and upper layer, respectively, the mixture fraction can be expressed in terms of h and q_t as

$$\chi(\boldsymbol{x},t) = \frac{h(\boldsymbol{x},t) - h_0}{h_1 - h_0} = \frac{q_t(\boldsymbol{x},t) - q_{t,0}}{q_{t,1} - q_{t,0}} \quad . \tag{4.1}$$

Herein, $\boldsymbol{x} = (x,z)$ denotes the location and t is the time coordinate. Hence, the mixture fraction simply measures the fraction of mass of fluid from the top layer in an arbitrary fluid parcel in the flow; by definition, $\chi = 0$ in the bottom layer and $\chi = 1$ in the top layer. The thermodynamic state of the system, in particular the density field, is then completely defined by the field of χ.

Using the Boussinesq approximation, gravitational forces are described in terms of the buoyancy

$$b(\boldsymbol{x},t) = \frac{\rho_0 - \rho(\boldsymbol{x},t)}{\rho_0}\, g\,, \tag{4.2}$$

with g denoting the magnitude of the gravitational acceleration and ρ is the density. This is justified because differences in density across the cloud-top inversion are small. Depending on the initial data, evaporative cooling can

cause saturated mixtures to be heavier than either one of the unmixed reference states. The term "buoyancy reversal" is introduced to identify this eventuality [68, 90]. The heaviest mixture $0 \leq \chi_s \leq 1$ occurs at saturation conditions and has buoyancy $b_s = \frac{\rho_0 - \rho_s}{\rho_0} g$. Shy and Breidenthal [67] introduce the buoyancy reversal parameter

$$D = \frac{\rho_s - \rho_0}{\rho_1 - \rho_0} = -\frac{b_s}{b_1}$$

to describe the strength of the reversal, relating buoyancy of the heaviest mixture to the buoyancy jump $b_1 = \frac{\rho_0 - \rho_1}{\rho_0} g$ across the inversion. With the above assumptions and for small density differences $\rho_0 - \rho_1$, buoyancy can be accurately approximated by a piecewise linear function of the mixture fraction. Here, the formulation

$$b(\chi)/b_1 = -\frac{D}{\chi_s}\chi + \left(\frac{1+D}{1-\chi_s} + \frac{D}{\chi_s}\right) \delta_s \ln\left[\exp\left(\frac{\chi - \chi_s}{\delta_s}\right) + 1\right] \qquad (4.3)$$

introduced by Mellado et al. [42] is adopted. Figure 11 shows three examples of the graph of $b(\chi)$: namely a non-reversing and a strongly reversing case for illustrative purposes, and the buoyancy mixing function for the present case. The parameter δ_s was introduced to smooth the discontinuity between the piecewise linear sections. Obviously, the smoothing damps the maximum negative buoyancy $-b_s$ and, thus, the effective reversal parameter D. Previous work by Mellado et al. [42] shows that a smoothing parameter of $\delta_s = \chi_s/16$ leads to a sufficient independence of the solution from changes in δ_s. This value of δ_s is adopted here for consistency in the comparison.

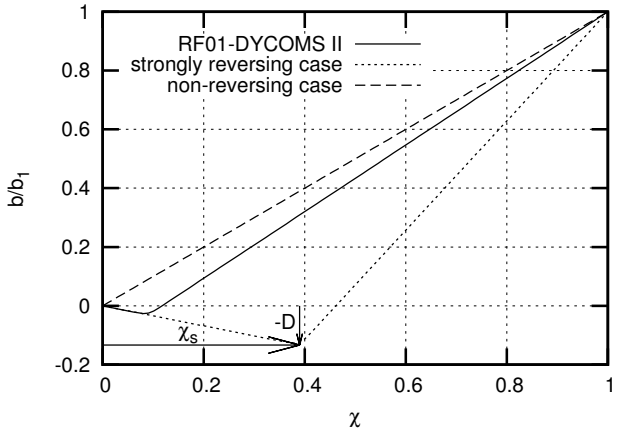

Figure 11: Non-dimensional buoyancy mixing function for the present case (solid), and two fictional cases: a non-reversing (dashed) and a strongly reversing case (dotted). The latter one corresponds to the case A3 by Mellado et al [42].

4.3.2 *Model equations*

With the assumptions made in section 4.3.1, the set of prognostic variables in two dimensions consists of the two Cartesian velocity components $v =$

$(u, w)^T$, the dynamic pressure p, and the mixture fraction χ. The reference DNS solves the Boussinesq limit of the Navier-Stokes equations, given by

$$\frac{\partial \boldsymbol{v}}{\partial t} + \boldsymbol{v} \cdot \nabla \boldsymbol{v} = -\nabla p + \nu \nabla^2 \boldsymbol{v} + b(\chi)\boldsymbol{k} \tag{4.4}$$

$$\frac{\partial \chi}{\partial t} + \boldsymbol{v} \cdot \nabla \chi = \nu \nabla^2 \chi \tag{4.5}$$

$$\nabla \cdot \boldsymbol{v} = 0\,. \tag{4.6}$$

Herein, ν is the constant kinematic viscosity of the mixture. The buoyancy mixing function $b(\chi)$ is given by Eq. (4.3), $\boldsymbol{k}$ is the vertical unit vector, and p is a modified pressure, normalized by the density. The Poisson equation for the dynamic pressure

$$\nabla^2 p = \nabla \cdot \left[-\boldsymbol{v} \cdot \nabla \boldsymbol{v} + \nu \nabla^2 \boldsymbol{v} + b(\chi)\boldsymbol{k} \right] \tag{4.7}$$

couples conservation of mass, Eq. (4.6), to the momentum Eq. (4.4) and completes the system of equations.

The LES code, whose native formulation solves Ogura-Phillips [49] type anelastic equations, Eqs. (2.70)-(2.73), was modified to solve exactly the same system. This was done by setting $\rho_0(z) \equiv 1$ kg m^{-3}, using the total water mixture fraction q_t as χ, and replacing the buoyancy term in Eq. (2.70) by the buoyancy function $b(\chi)$ in Eq. (4.3). Since the focus in the present analysis are low-order numerical effects, and not the subgrid-scale models intrinsic to LES (cf. Pope [54]), the SGS model in the UCLA-LES was disabled and the constant molecular viscosity ν was introduced. Note that convergence to the DNS solution would be achieved with the SGS model turned on in addition to molecular diffusion, because at the resolutions used, the contribution of the SGS term vanishes. The values of the turbulent viscosity computed based on the solution of the unfiltered equations were two orders of magnitude smaller than the molecular viscosity at reference resolution.

Throughout all LESs, Courant-Friedrichs-Lewy (CFL) numbers of

$$CFL_{\text{adv}} = \frac{\max[u(\boldsymbol{x}), w(\boldsymbol{x})]\,\Delta t}{\Delta x} \leq 0.5 \tag{4.8}$$

and

$$CFL_{\text{diff}} = \frac{\Delta t\, \nu}{(\Delta x)^2} \leq 0.5 \tag{4.9}$$

were maintained.

4.3.3 *Initial and boundary conditions*

The density-stratified system is at rest in the beginning. Profiles of specific enthalpy and total water mixing ratio change in the vertical from values characteristic of the saturated and unsaturated layer over a height of the order of 4δ following an error function. Employing the mixture fraction formulation (4.1) allows for a specification of the initial thermodynamic conditions by

$$\chi(t = 0, x, z) = \frac{1}{2}\left[1 + \text{erf}\left(\frac{z - z_0(x)}{2\delta}\right)\right]. \tag{4.10}$$

Herein, z_0 denotes the vertical position of maximum stratification which corresponds to the height where $\chi = 0.5$. The combination of Eqs. (4.3) and

(4.10) gives the vertical profile of the buoyancy. Both profiles are plotted in Fig. 12. In a non-reversing scenario (cf. dashed graph of Fig. 11) the normalized buoyancy would match the mixture fraction profile. In contrast, under conditions of buoyancy reversal, a small peak to the negative buoyancy axis develops just below the $\chi = 0.5$ isoline. Thus, the system is unstable with respect to the lower fluid in a thin layer.

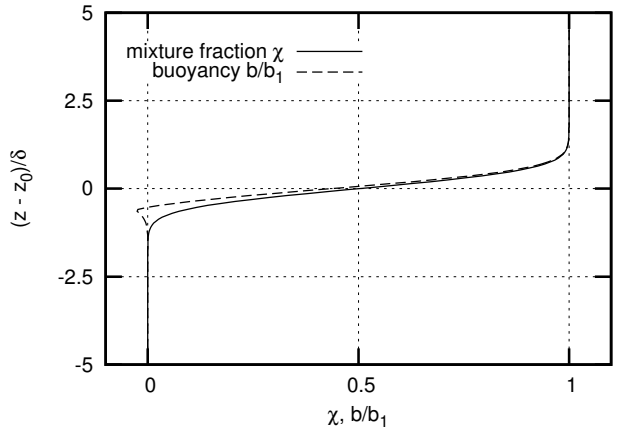

Figure 12: Vertical profiles of the mixture fraction and buoyancy as following from Eqs. (4.3) and (4.10).

The instability process is triggered by imposing one mode of a sinusoidal wave on the inversion height z_0 with the wave length λ and amplitude $a/2$ according to

$$z_0(x) = \frac{a}{2} \cos\left(\frac{2\pi x}{\lambda}\right) .$$

Here, a measures the thickness of the perturbed mixing layer. The ratio of amplitude to wave length is $(a/2)/\lambda = 0.1$ and the initial thickness of the error function profile is $\delta/\lambda = 0.025$. The flow is simulated on a two-dimensional rectangular domain with the extent $(\Omega_x, \Omega_z) = (\lambda, 2\lambda)$. The mean height of the inversion, given by the mean height of the $\chi = 0.5$ isoline, is located at 60% of the vertical domain. The leftmost plot in Fig. 13 shows the initial situation.

The conditions considered correspond to the STBL as observed in the first research flight of the second DYCOMS field programme [78]. The data shows weak buoyancy reversal with a buoyancy reversal parameter of $D = 0.031$. The mixture fraction at saturation conditions is $\chi_s = 0.09$ which completes the description of the buoyancy function (4.3) (cf. Fig. 11). Mellado et al. [42] introduce the reference Grashof number

$$Gr = \frac{a^4 b_1}{\nu^2 \lambda} ,$$

which can be interpreted as the square of the ratio of two characteristic time scales. The first one is the viscous time that scales as a^2/ν; the second one is the period of the oscillation of the interface and is proportional to $\sqrt{\lambda/b_1}$ [42]. For the reference simulation the kinematic viscosity $\nu = 1.5 \cdot 10^{-5}\ \mathrm{m^2/s}$ and $Gr = 6.4 \cdot 10^5$ were used. That corresponds to, keeping the above ratio of $(a/2)/\lambda$ in mind, a wave length $\lambda \approx 0.71$ m of the sinusoidal perturbation.

Cyclic boundary conditions are imposed at the lateral boundaries and free-slip conditions are used at the top and bottom of the domain. For scalars

zero gradients in the vertical are set at the top and bottom. The simulations are stopped before finite-size effects associated with the computational domain become important.

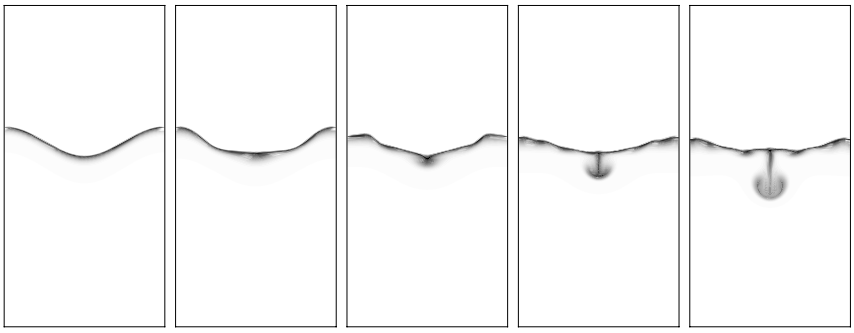

Figure 13: Time series of the buoyancy field at times $t/T = (0.0, 1.05, 2.18, 3.32, 4.45)$ with $T = 2\sqrt{\pi}\sqrt{\lambda/b_1}$, colours range from zero (white) to $-b_1$ (black). UCLA-LES, 512×1024 grid cells.

4.4 SIMULATIONS

4.4.1 *The reference DNS code*

The reference DNS uses finite differences and a regular Cartesian mesh. Spectral-like 6th-order compact Padé schemes are used to discretize the first- and second-order spatial derivatives (closed at the top and bottom with 3rd-order biased formulae, which leads to a global 4th-order accuracy in space). A low-storage 5-stages 4th-order Runge-Kutta scheme is employed for the time advancement. This scheme has a stability region larger than that of the 3rd-order counterpart, and the CFL numbers used in the DNS are $CFL_{\text{adv}} < 1.2$ and $CFL_{\text{diff}} < 1.2/4$. Similarly to the UCLA-LES, the solenoidal constraint is imposed using Fourier decomposition along the periodic horizontal planes in order to reduce it to a set of one-dimensional second-order equations which are solved using those same compact schemes. The boundary conditions imposed at the top and the bottom are the same as those in the UCLA-LES code (Mellado, private communication [41]). Further details of the numerical algorithm can be found in Mellado et al. [40].

Besides the present non-turbulent case of the evaporatively-driven cloud-top mixing layer in two dimensions [42, 43, 45], the numerical algorithm was also used to study the 3D turbulent case with [40] and without additional shear [46] as well as a smoke cloud mixing layer driven purely by radiative cooling [10].

The major difference between the DNS and the UCLA-LES code is the resolving efficiency. This resolving efficiency is normally quantified in terms of the number of points per wavelength (PPW) required to maintain errors in the corresponding transfer function below a specified level (or, equivalently, a specified error in the dispersion velocity of the linear advection problem). In these terms, an error of 1% requires 4 PPW in the case of the implicit compact scheme used in the DNS, whereas the second-order explicit scheme requires 25 PPW [30, 33] (this difference is even higher if the common reference error of 0.1% is retained, for which the previous finite difference schemes require 6 PPW and 100 PPW, respectively). However, these are theoretical values based on linear analysis of the algorithm: in this work, the

relative performance of these two numerical schemes is ascertained in an applied case very relevant to the physics of the STBL, namely the stratocumulus top (Mellado, private communication [41]).

4.4.2 *Analysis of the flow*

The qualitative evolution of the flow is illustrated in Fig. 13 through successive snapshots that visualize the negative buoyancy field. The data shown was obtained from the UCLA-LES run on the reference grid with 512×1024 cells. The leftmost panel corresponds to the sinusoidal initial condition, as previously discussed in section 4.3.3. The stratified system is initially at rest. In the vicinity of the inversion, net vertical accelerations arise from horizontal buoyancy differences. A persistent oscillation of the interface sets in that, at high Gr, is only slowly damped by molecular viscosity. At the same time a spike or finger starts to form of the thin negatively buoyant sheet at the lowest point of the oscillation. The spike grows downwards and later rolls up to a vortex pair. Molecular diffusion mixes fluid of the falling finger with the ambient moist fluid and, thus, spreads buoyancy reversal. According to the buoyancy mixing function (cf. Fig. 11) moist fluid ($\chi = 0$) that is mixed with negatively buoyant fluid is negatively buoyant itself. This process continues as the pulsating motion of the inversion pumps more negatively buoyant fluid downwards.

The instability process is driven by the transformation of potential energy (here subsumed within the enthalpy of vaporization) to kinetic energy. As the unsaturated fluid in the upper layer mixes with the saturated fluid in the lower layer, more negatively buoyant fluid is produced due to evaporative cooling, part of it is ejected downwards. This gradually leads to a vertical growth of both, the size of the saturated bottom layer, and the depth of the mixing region.

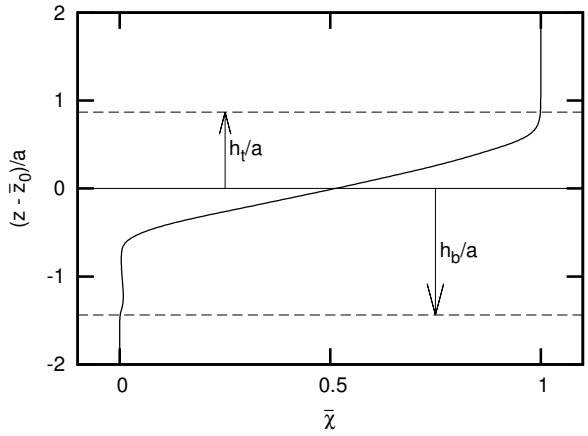

Figure 14: Definition of the penetration length h_b and the upper perturbation thickness h_t using the horizontally averaged mixture fraction profile $\bar{\chi}$. The dashed lines indicate the vertical position where $\bar{\chi}$ departs from a given threshold (10^{-3}) of the upper and lower state, respectively.

Mellado et al. [42] quantify the instability process by means of two characteristic lengths that measure the thickness of the mixing layer to the top and to the bottom. These are the penetration length h_b of the falling finger and the perturbation thickness h_t that measures the upwards growth of the moist layer. Both are defined with the help of the horizontally averaged

mixture fraction profile $\bar{\chi}(z)$ as shown in Fig. 14. Taking the mean initial height of the $\chi = 0.5$ isoline, $\bar{z}_0$, as a reference, both lengths are defined as distances to the vertical position where the mean mixture fraction departs from a given threshold of the value of the respective layer. For h_b, the first position looking from the bottom, for h_t the first position looking from the top are detected, respectively. Because mixing in the lower layer is limited to small fractions of $\bar{\chi}$ below 0.1, a threshold of 10^{-3} is chosen.

The temporal evolution of these lengths is presented in Figs. 15 and 16, respectively, where the solid lines indicate the results from the DNS by Mellado et al. [42]. The evolution of the penetration length h_b observed in Fig. 15 exhibits a superposition of the stable oscillatory mode of the inversion and the unstable mode of the falling finger. If buoyancy reversal was not present (cf. dashed graph in Fig. 11), only the stable mode would be visible. The evolution of the upper perturbation thickness h_t also has the stable mode; it is superimposed by a quasi-linear growth that results from molecular mixing of χ at the top of the inversion and the baroclinic production of vorticity. The transport of mixed fluid away from the inversion due to buoyancy reversal steepens local scalar gradients which in return enhances molecular mixing. In the following, these two lengths are used to quantify numerical errors and the convergence of the UCLA-LES code.

4.4.3 *Convergence behaviour*

In order to study the convergence behaviour of the UCLA-LES code a grid convergence study was carried out. The reference DNS employs a grid with 512×1024 grid points; this will be referred to as reference resolution or reference mesh in the following. Here, simulations were carried out on six different meshes, ranging from 1/8th to 4 times the reference resolution (see Tab. 5).

The UCLA-LES code, used as explained in section 3.2, has an anticipated second-order convergence in space. To confirm this, simulations on all meshes have been performed with a common time increment, and the order of convergence p in terms of the L_2 norm and the maximum norm L_∞ of the mixture fraction field have been determined. Based on the solution of χ on three meshes resolved by $\Delta x = \Delta z = h$, $2h$, and $4h$, respectively, the norms

$$L_2(h) = \sqrt{\frac{1}{N}\sum_{i=1}^{N} \left[\, \chi_{2h}(\boldsymbol{x}_i) - \chi_h(\boldsymbol{x}_i) \,\right]^2}$$

and

$$L_\infty(h) = \max\left(\left| \chi_{2h}(\boldsymbol{x}_i) - \chi_h(\boldsymbol{x}_i) \right| \right)$$

are computed, where $\boldsymbol{x}_i = (x_i, z_i)$ is the position of the ith cell-centred point of the mesh. Linear interpolation on the staggered mesh is used to interpolate values from the finer mesh to the coarser mesh. The order of convergence is computed according to

$$p_{2,\infty} = \ln\left(\frac{L_{2,\infty}(2h)}{L_{2,\infty}(h)} \right) / \ln(2)\,.$$

This procedure is repeated for all subsets of three neighbouring meshes. The results are presented in Table 5 and confirm the anticipated second-order convergence in both, the maximum and L_2 norm.

Table 5: Order of convergence p of the UCLA-LES according to the L_2 and maximum norm L_∞. The factors in the mesh row refer to the number of mesh cells, e.g. 1/8 refers to an eight times coarser mesh.

Mesh	1/8	1/4	1/2	[512×1024]2x		4x
p $[L_2]$	-	1.9991	1.9975	1.9987	1.9976	-
p $[L_\infty]$	-	1.9948	1.9951	1.9874	1.9508	-

In the following, the absolute errors of the solution are quantified. This is done by comparing the evolution of h_b and h_t in the DNS and LES code. Besides the reference DNS solution, Figs. 15 and 16 show the results obtained from the LES on the six meshes. For both h_b and h_t, a clear trend is obvious: with coarsening the mesh spacing the growth of both quantities is increased. This can mainly be attributed to increased numerical mixing, yielding more generation of negatively buoyant fluid that enhances the convective mixing process in the cloud layer. The temporal evolution of the relative errors is explicitly showed in the second panel of Fig. 15 and Fig. 16. On the coarsest grid, relative errors of h_b are up to 30 % and decrease to 5 % at reference resolution and to 2.4 % on the finest grid. Relative errors of h_t tend to be greater on the coarsest grid but vanish more rapidly as the grid is refined. On the finest grid, i.e. four times the number of grid points in each direction than in the reference DNS, the relative error remains below 1 % throughout the simulation.

The mean vertical growth of the upper perturbation thickness h_t is an effect that resembles the cloud-top entrainment in real stratocumulus. This mean growth E is quantified with help of a linear regression based on the data points after the first period until the ninth period of each individual data set. The latter corresponds to the last h_t maximum in the DNS reference data. The regression lines for the DNS solution and the finest and coarsest LES solution are shown in Fig. 16. Relative errors with respect to the DNS solution are presented in Tab. 6. While at four times the reference resolution, the error in the mean vertical growth of the upper perturbation thickness reduces to 1.4%, it increases to 89% on the coarsest grid with 1/8th the reference resolution. The latter corresponds to a mesh spacing of about 1 cm, still much finer than in current high-resolution LES of stratocumulus, where typically the vertical resolution is between 1 and 5 m at the cloud top [79, 91]. This result shows clearly that state-of-the-art LES does not resolve the sharp gradients at the cloud top and that this under-resolution has important effects on the thermodynamics of the system, and helps explain the difficulties encountered in understanding local processes of the cloud top [71].

Figure 17 shows the total amount of fluid entrained from the upper layer into the section of the domain below the lowest point of the initial wave. This portion of fluid is simply measured by the (vertical) integral I of the mean mixture fraction profile $\bar{\chi}$ in that subdomain and that portion of fluid monotonously increases when the grid is coarsened. This indicates that the more rapid increase of h_b on the coarser grids is, in fact, associated with a larger amount of fluid from the upper layer carried downwards by the falling finger. It is not solely attributed to the stronger spurious (numerical) spread of the border of the falling finger, but also to a modification of the global dynamics of the system. Here, numerical errors act as to increase the entrainment of drier fluid into the cloudy layer.

Table 6: Relative errors of the h_t growth rate E_{LES} in the low-order simulations with respect to the DNS solution.

Mesh	$\frac{E_{\text{LES}}-E_{\text{DNS}}}{E_{\text{DNS}}} \cdot 100\%$
1/8	88.8%
1/4	47.3%
1/2	33.8%
[512×1024]	18.6%
2x	7.9%
4x	1.4%

4.4.4 *Computational efficiency*

Both the DNS and UCLA-LES algorithms were originally implemented to solve three-dimensional problems. For the work discussed so far, the codes have been run on a two-dimensional grid in order to reduce computational cost and focus on some details of the cloud top in a very controlled manner. However, that causes computational overheads that depend on the respective methods and their implementations. To enable for a fair comparison in terms of computational efficiency, three-dimensional runs where carried out. The 128×256 grid ($1/4$th of the reference resolution) was extended in the lateral to $128 \times 128 \times 256$. Both codes were compiled with the same compiler and run on one core of an AMD Opteron model 2384, 2.7 GHz of a Sun X2200 M2 machine. Table 7 compares the computational time per iteration, T_1, and the computational time T_2 needed per characteristic time of the system $\sqrt{\lambda/b_1}$. (Averages over 100 iterations were considered in order to eliminate I/O times and other overheads.)

Table 7: Mean computational times per iteration, T_1, and computational time T_2 per characteristic time of the system $\sqrt{\lambda/b_1}$. DNS results are based on a low-storage 4th-order Runge-Kutta scheme and UCLA-LES results on a 3rd-order Runge-Kutta scheme.

	DNS	UCLA-LES
T_1 [s]	36.7	15.7
T_2 [s/$\sqrt{\lambda/b_1}$]	547.7	489.3

The DNS is more expensive per iteration, as expected because of the 4th-order Runge-Kutta scheme (which uses 5 stages because of the two-level storage property) and an implicit spatial discretization. When the DNS code is run with a 3rd-order Runge-Kutta scheme, similarly to the LES code, then the time per iteration is 22 seconds. This is about 40% more expensive than the low-order code; this 40% difference is due purely to spatial discretization and accounts for the overhead due to the solution of the linear systems being associated with the implicit compact schemes, in contrast to the explicit character of the second-order central schemes.

However, it is arguably more interesting to consider the computational cost per characteristic physical time of the system, i.e. how much it costs to advance the transport equations during a given time interval. This is the

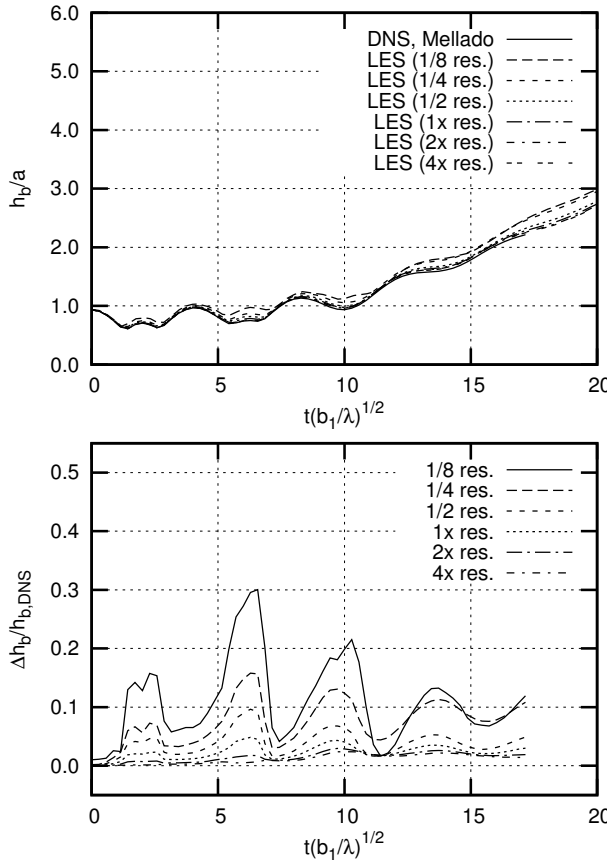

Figure 15: History of the penetration length (top) and the relative error with respect to the reference DNS (bottom). Grid resolutions are given with respect to the reference grid with 512×1024 grid points.

second parameter shown in Table 7, the time T_2. The difference with the measurement per iteration T_1 discussed in the previous paragraph is due to the fact that the low-storage 4th-order Runge-Kutta has a stability region significantly larger than that of the 3rd-order Runge-Kutta and allows a larger CFL number. Comparisons of the values of T_2 between the DNS and the UCLA-LES codes show that the DNS is still slower, but only by 10%.

This last result is very important. As was shown in section 4.4.3, using the low-order numerical method of the UCLA-LES code, higher resolution is needed to converge to the reference solution. For the particular problem studied here, the buoyancy reversal instability at the cloud top, using the low-order algorithm leads to errors of the order of 20% and is only about 10% faster. Suppose one desired to reduce errors using the UCLA-LES code to about 10%. Then, according to Tab. 6, the resolution needs to be increased by about a factor of two. This step already implies a higher computational cost; a reasonable rough estimate would be a factor of 8 in three-dimensions, or a factor of 4 in two-dimensions, assuming a linear relation between the operation count and the number of grid points and neglecting deviations due to parts of the algorithm which do not scale linearly with the number of points, like fast Fourier transforms or cache-size management. On top of that, the time increment Δt imposed by the explicit scheme, so stability is satisfied, multiplies further this factor by 2 or 4, according to Eq. (4.8) or Eq. (4.9), respectively. In the present problem, it was found that the latter dominates

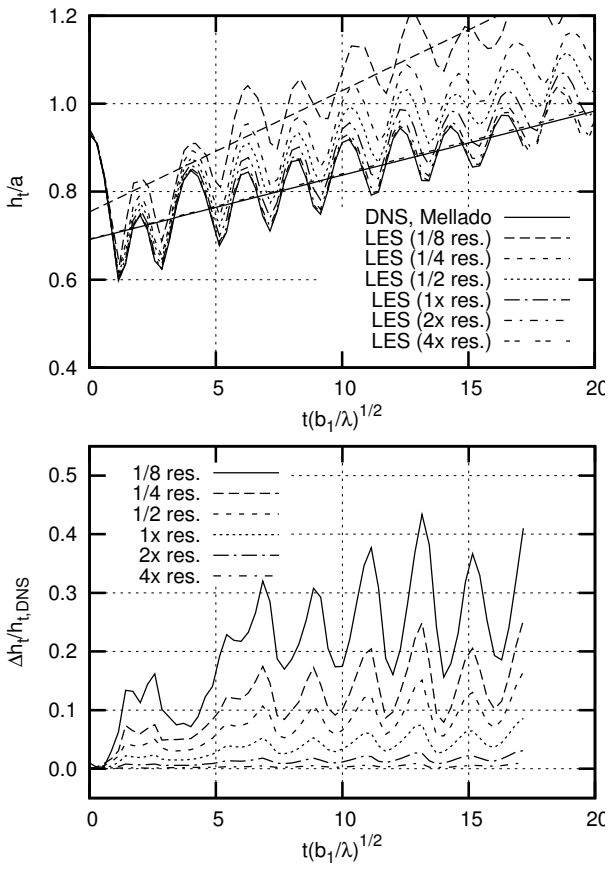

Figure 16: History of the upper perturbation thickness (top) and the relative error with respect to the reference DNS (bottom). Straight lines (top) are least squares regressions of the growth rate from the 2nd to the 9th local maximum. Grid resolutions are given with respect to the reference grid with 512×1024 grid points.

because the diffusion constraint Eq. (10) becomes the most restrictive and Δt scales as $(\Delta x)^2$. Altogether, this analysis means about a factor of 10 or more increase in computational cost using a low-order algorithm, compared to a factor 1.1 increase using the implicit spectral-like compact finite differences, to obtain a solution within a 10% error.

It is appropriate to note that the discussion of the last paragraph refers to a serial implementation of the algorithm. The advantage of low-order spatial schemes is that they are explicit and parallelizations thereof are known to scale almost linearly, so that the computational cost remains approximately independent of the number of processors, whereas the implicit schemes suffer a strong overhead from the communication among a relatively large number of processors. Hence, there is a trade-off and a cross-over number of processors beyond which a low-order scheme is more efficient than a high-order implicit scheme. However, this cross-over value is a relatively high number. For instance, the DNS algorithm used here as a reference is run typically in 1024 or 2048 MPI (message-passing interface) tasks (e.g. simulations presented in [40]) in the German Climate Computer Centre and in the Jülich Supercomputer Centre. In those architectures, the time spent in communication among processors varies between 40% and 60%, meaning an overhead of the order of a factor of 2 with respect to the reference com-

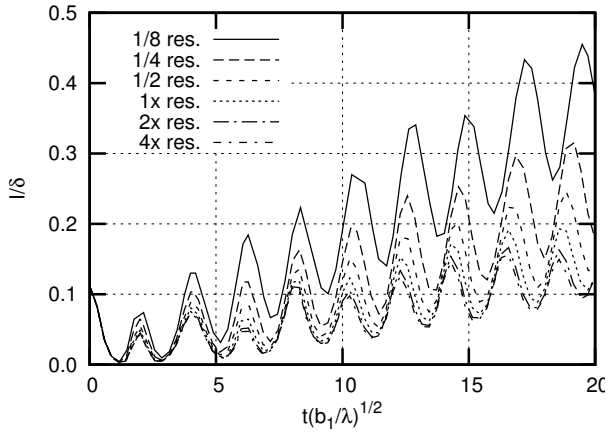

Figure 17: Evolution of the amount of fluid entrained in the section of the domain below the lowest point of the initial wave of the $\chi = 0.5$ isoline. It is measured by the integral I of the mean mixture fraction profile $\bar{\chi}$ normalized by δ as in Eq. (4.10).

putational cost. The same behaviour has been observed in scaling studies of the DNS code up to 8192 tasks in the Jülich Supercomputer Centre. This overhead is still significantly smaller than the factor of 10 estimated above for a second-order scheme used in the UCLA-LES code to obtain solutions within 10%. Last but not least, the additional memory requirements need to be considered that is associated with the larger number of points when using low-order schemes. (This can actually be the most critical aspect in large-scale three-dimensional simulations.)

Hence, as a summary, high-order schemes, in spite of the higher complexity in implementation, might be attractive for LES of stratocumulus and other high Reynolds number flows if small-scale processes might play a relevant role or simply to better represent the smooth portions of the flow, such as waves, that might exist at some multiple of the grid scale. This has implications for the current trend to increase resolution in LES models and the application of adaptive solvers to such problems. These conclusions hold also for parallel implementation, at least up to the order of 10000 processors, which current architectures provide.

4.5 SUMMARY AND CONCLUSIONS

This chapter presented in detail the two-dimensional evaporatively driven cloud-top mixing layer as a test case for the study of low-order numerical effects. This was done by comparing the UCLA-LES code, which uses an explicit second-order scheme, against a DNS solution, based on a spectral-like compact sixth-order accurate method. The subgrid-scale turbulence model of the UCLA-LES code was switched off, and a constant molecular viscosity was used instead so that only numerical effects were addressed in this work. A grid convergence study was presented where investigating the sensitivity of the solution to numerical errors and the resolution requirements for the UCLA-LES algorithm to achieve convergence.

Analysis of the solutions on the various grids showed that the LES numerical algorithm is self-convergent meeting the anticipated effective 2nd-order rate of convergence. In order to quantify numerical errors, the evolution of the penetration length h_b of the downdraught and the upper perturba-

tion thickness h_t was compared between the LES and DNS solutions. The coarsest grid had a vertical spacing of approximately 1 cm which is at least two orders of magnitude finer than in typical LES. For these quantities, 30% and 40% relative errors, respectively, were measured on the coarsest mesh; almost 100% relative errors in the entrainment rate. Hence, very high resolution or high-order schemes are needed to capture the small-scale molecular mixing. If these small-scale effects are not accurately represented, important large-scale characteristics, such as the vertical growth of the inversion height, resembling cloud-top entrainment, may contain order one defects caused by numerical artefacts.

The analysis of the computational efficiency showed that the cloud-top problem is solved more efficiently (in terms of total CPU time) by the high-order scheme used in the reference DNS than by the low-order scheme of the UCLA-LES code. This suggests that increasing the order of numerical methods might be better suited than further increasing the resolution of low-order methods to improve the LES of flows that are not smooth on the grid scale (such as LES of stratocumulus). Furthermore, the larger computational cost per integration step is by far compensated by a smaller number of grid points, a larger possible temporal stride, and reduced magnitude of numerical errors. The difference is so remarkable that the same conclusion holds in a parallel implementation of the algorithms, at least up to the order of 1-10 thousand processors, despite the communication overhead associated with the implicit schemes.

5 CONTROLLING ENTRAINMENT IN THE SMOKE CLOUD

The results presented in this chapter have previously been published in

[16] Dietze, E., Schmidt, H., Stevens, B., & Mellado, J. P. (2015). Controlling entrainment in the smoke cloud using level set-based front tracking. *Meteorologische Zeitschrift*, 23(6), pp. 661-674. Schweizerbart'sche Verlagsbuchhandlung Stuttgart. doi:10.1127/metz/2014/0595.

The code used to produce the results is available on GitHub:

https://github.com/uclales/uclales/tree/level-set-smoke-cloud .

5.1 INTRODUCTION

In this chapter, the front-tracking algorithm is applied to Lilly's [32] smoke cloud, as discussed in Sect. 1.3, where the case of vanishing entrainment is considered. The smoke cloud is a simplified surrogate of the stratocumulus-topped boundary layer (STBL) that is only driven by radiative cooling from the cloud top. Bretherton et al. [8] carried out an large-eddy simulation (LES) intercomparison for this case with the goal to better understand the effect different numerics on errors in the solution. This was possible because of the smoke cloud's simplified configuration as compared to the STBL. It is simpler than the STBL in that it is dry and, thus, avoids evaporative feedback on entrainment. Bretherton et al. [8] found that differences in how the liquid water content is diagnosed from total water content gave rise to substantial variations of the between numerical models. In addition, the same radiation model was used in all participating codes, leaving differences in the numerics and the choice of the subgrid-scale (SGS) models as remaining causes for differences in the solution.

This chapter is structured as follows. Section 5.2 describes the smoke cloud case, the governing equations, and initial and boundary conditions. Specifics of the front-tracking algorithm for this case are summarized in Sect. 5.3, and simulation results thereafter in Sect. 5.4. The study is summarized and the main conclusions are presented in Sect. 5.5.

5.2 FORMULATION

5.2.1 *Governing equations*

The case considered is the smoke cloud as described by Bretherton et al. [8]. It is a dry convective boundary layer (CBL) filled with radiatively active smoke. The CBL is topped by clear and relatively warmer air forming a temperature inversion between the two layers. There are no surface fluxes of heat or smoke. The problem is formulated in terms of the potential temperature θ and the non-dimensional smoke concentration S. The latter is bounded by 0 and 1 and can also be interpreted as a mixture fraction relating mass of air from the CBL relative to the total mass of a fluid parcel (cf. [45]).

Radiation is represented by the same 1D column-wise model as used by Bretherton et al. [8]. They incorporated radiation in terms of the vertical

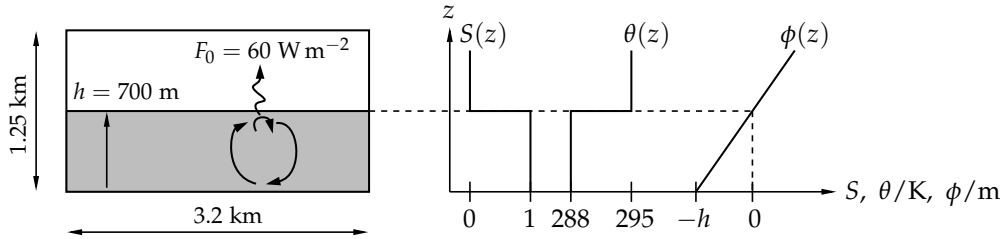

Figure 18: Vertical structure and initial conditions of the smoke cloud case. The left side shows a sketch of a vertical cut through the domain. The boundary layer filled with smoke (grey) has an initial depth h and is driven by a constant radiative heat flux F_0. The right hand side shows the initial profiles of the non-dimensional smoke concentration S, the potential temperature θ, and the level set function ϕ.

radiative flux F_{rad}, the vertical gradient of which contributes to the temperature tendency according to

$$\left(\frac{\partial\theta}{\partial t}\right)_{\mathrm{rad}} = -\frac{1}{c_p\rho_0}\frac{\partial F_{\mathrm{rad}}}{\partial z} \quad . \tag{5.1}$$

Assuming the average temperature of the smoke cloud stays close to its initial value over the time considered, the cloud cools at a constant net rate limited by the radiative flux F_0 at the top of the domain. With this assumption, the radiative flux at any given height z is given by

$$F_{\mathrm{rad}}(z) = F_0\,\exp\big(-K_a\int_{z'=z}^{H}\rho_0 S\,dz'\big)\,. \tag{5.2}$$

Here, H is the height of the domain and K_a is the smoke absorptivity (cf. Tab. 8). The remaining prognostic variables are the Cartesian velocity vector $\boldsymbol{v} = (u, v, w)$ and the dynamic Exner pressure $\pi = (p/p_{00})^{R/c_p}$ (p is the physical dynamic pressure). The governing equations are the LES-filtered, Ogura-Phillips-type [49] anelastic equations (2.70)-(2.73) with two modifications: First, the liquid water potential temperature θ_l reduces to the potential temperature θ in the absence moisture. And Second, the general source term Q in Eq. (2.71) is replaced by Eq. (5.1). The result in differential form is

$$\frac{\partial\bar{\boldsymbol{v}}}{\partial t} + \frac{1}{\rho_0}\nabla\cdot(\rho_0\bar{\boldsymbol{v}}\otimes\bar{\boldsymbol{v}}) = c_p\Theta_0\nabla\bar{\pi} + \frac{g\bar{\theta}'}{\Theta_0}\boldsymbol{k} + \frac{1}{\rho_0}\nabla\cdot(\rho_0\boldsymbol{\tau}) \tag{5.3}$$

$$\frac{\partial\bar{\theta}}{\partial t} + \frac{1}{\rho_0}\nabla\cdot(\rho_0\bar{\theta}\bar{\boldsymbol{v}}) = \frac{1}{\rho_0}\nabla\cdot(\rho_0\gamma_\theta) - \frac{1}{\rho_0 c_p}\frac{\partial F_{\mathrm{rad}}}{\partial z} \tag{5.4}$$

$$\frac{\partial\bar{S}}{\partial t} + \frac{1}{\rho_0}\nabla\cdot(\rho_0\bar{S}\bar{\boldsymbol{v}}) = \frac{1}{\rho_0}\nabla\cdot(\rho_0\gamma_S) \tag{5.5}$$

$$\nabla\cdot(\rho_0\bar{\boldsymbol{v}}) = 0\,, \tag{5.6}$$

where the bar represents the filter operator. In these equations, ρ_0 is the hydrostatic density profile of the isentropic atmosphere at temperature Θ_0, $\bar{\theta}'$ is the temperature anomaly $(\bar{\theta} - \Theta_0)$, and $\boldsymbol{k}$ is the vertical unit normal vector. Table 8 shows the values of the physical parameters used here. These are the isobaric heat capacity and the gas constant of dry air, c_p and R,

Table 8: Physical parameters

Smoke absorptivity	K_a	0.02	$\mathrm{m^2\,kg^{-1}}$
Specific gas constant of dry air	R	287	$\mathrm{J\,(kg\,K)^{-1}}$
Isobaric heat capacity of dry air	c_p	1004	$\mathrm{J\,(kg\,K)^{-1}}$
Isochoric heat capacity of dry air	c_v	717	$\mathrm{J\,(kg\,K)^{-1}}$
Gravitational acceleration	g	9.8	$\mathrm{m\,s^{-2}}$
Reference pressure	p_{00}	1000	hPa
Reference temperature	Θ_0	291.5	K
Reference density	ρ_0	1.1436	$\mathrm{kg\,m^{-3}}$

respectively, the gravitational acceleration g, the basic state temperature Θ_0, and reference pressure p_{00}.

The anelastic continuity equation (5.6) is obeyed by solving the Poisson equation for $\bar{\pi}$

$$\nabla\cdot(\rho_0\nabla\bar{\pi}) = \frac{1}{c_p\Theta_0}\left[\nabla\cdot\left(-\nabla\cdot(\rho_0\bar{\boldsymbol{v}}\otimes\bar{\boldsymbol{v}}) + \frac{\rho_0\bar{\theta}'g}{\Theta_0}\boldsymbol{k} + \nabla\cdot(\rho_0\boldsymbol{\tau})\right)\right]. \quad (5.7)$$

In the present case of the radiatively driven smoke cloud, two scalar transport equations are solved, one for S, the non-dimensional smoke concentration, and another one for θ, the potential temperature. Both equations are coupled via the radiative cooling term in the temperature equation, which causes the two scalar fields to diverge over time and a mixture fraction formulation as in the purely evaporatively driven case in Chapt. 4 is not possible.

5.2.2 *Initial and boundary conditions*

Following Bretherton et al. [8], the 3D domain extends over 3.2 km in the two horizontal directions and from 0 to 1.25 km in the vertical. The bottom of the domain is filled with smoke over a depth of 700 m (cf. Fig.18). The initial profiles of the potential temperature θ and the smoke S are:

$$S(z) = \begin{cases} 1 & \text{if } z\in[0,687.5]\mathrm{m} \\ 1-0.04(\frac{z}{\mathrm{m}}-687.5) & \text{if } z\in(687.5,712.5)\mathrm{m} \\ 0 & \text{if } z\in[712.5,1250]\mathrm{m} \end{cases}$$

and

$$\theta(z) = \begin{cases} 288\mathrm{K} & \text{if } z\in[0,687.5]\mathrm{m} \\ 288\mathrm{K}+0.28\,(\frac{z}{\mathrm{m}}-687.5)\mathrm{K} & \text{if } z\in(687.5,712.5)\mathrm{m} \\ 295\mathrm{K}+10^{-4}\,(\frac{z}{\mathrm{m}}-712.5)\mathrm{K} & \text{if } z\in[712.5,1250]\mathrm{m}\,. \end{cases}$$

When the level set method is used, the linear transitional layer is omitted and the profiles are set up such that they are piecewise constant with only one vertical cell having an intermediate value. In order to trigger the spin-up

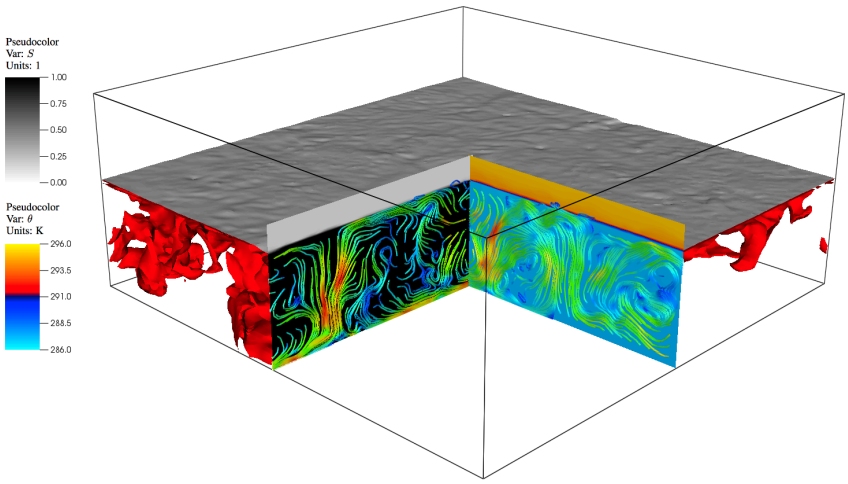

Figure 19: The smoke cloud after 3 hours as simulated by the LS-LES at the double resolution. The grey sheet indicates the location of ϕ_0. Colours on the left slice show the smoke concentration, colours on the right slice show potential temperatures. Both slices are overlaid with streamlines in the respective planes colour-coded by velocity magnitude. In the background is an arbitrary potential temperature isosurface in red ($\theta \approx 287.3$ K).

of the boundary layer (BL) convection, all temperature values below 650 m where perturbed by a spatially uncorrelated uniform random noise. The amplitude of the noise was set to ± 0.1 K. The boundary layer is initially at rest. The domain is periodic in the two lateral directions and free-slip boundary conditions are imposed at the top and bottom. For scalars, zero-gradient boundary conditions are set at the top and bottom. A sponge layer is used occupying the top ten grid levels. The smoke cloud is simulated for a period of four hours.

5.3 DETAILS OF THE FRONT-TRACKING ALGORITHM

For the simulation of the smoke cloud, a precursor of the front-tracking algorithm presented in Sect. 3.3 has been used. It is simpler in two ways. First, only advective fluxes of the scalars are coupled to the level set method and the diffusion is computed using the original method of the UCLA-LES. Second, a simplified version of the level set synchronization presented in Sect. 3.3.7 is used. In the present case, where there is no mixing across the interface. i.e. $w_e = 0$, and where there are no other sources or sinks of smoke, the exact reconstruction in cut cells is known to be $S_0 \equiv 1$ and $S_1 \equiv 0$. This is used for the synchronisation instead of the PDE-based extrapolations used in the ghost fluid method. The potential temperature, however, is reconstructed using the PDE-based extrapolation.

5.4 SIMULATIONS AND RESULTS

5.4.1 *Goals and setup*

The smoke cloud was simulated using the LS-LES and the standard LES as a reference. By analyzing the results, the following two main questions are addressed:

1. How accurately does the LS-LES maintain the prescribed zero entrainment and decouple the entrainment process from the BL convection? This is a requirement for (super-)parameterizing entrainment.

2. Does the method minimize the dependency of flow statistics on grid resolution and details of numerical methods used? The hypothesis is that by avoiding discretization over the interface, part of this problem can be removed.

For this, a series of simulations is carried out where two parameters are modified. The first one is grid resolution. Equidistant grids are used with Bretherton et al.'s [8] standard resolution of $64 \times 64 \times 50$ grid cells, denoted 'S', as well as double that resolution denoted by 'D'. The standard resolution corresponds to a grid spacing of 50 m in the horizontal directions and 25 m in the vertical direction. The double resolution reduces these numbers by a factor of 2. The second parameter is the choice of the flux limiter. In this study, the Minmod, Superbee, and monotonized-central (MC) limiter are used. These two parameters span a total of 12 simulations, 6 for both the standard LES and the LS-LES. In addition, two simulations were carried out with the standard LES with the limiter switched off.

Figure 19 shows a snapshot of the 'D' LS-LES after 3 hours with the grey sheet indicating the $\phi = 0$ isosurface. The instantaneous streamlines and the θ isosurface (red) indicate a complex turbulent flow in the BL. At the same time, there is a large-scale motion with strong vertical flow in the BL interior and horizontal redirection near the cloud top and bottom. The following sections discuss horizontally averaged statistics and focus specifically on entrainment and how it is affected by the choice of the numerical parameters. In addition, their effect on the turbulent kinetic energy (TKE), its evolution, and distribution in the vertical and horizontal components is assessed. A more extensive discussion of the details of the flow can be found in Bretherton et al.'s original paper [8].

The entrainment rate, in the context of interfacial convection, is typically defined as the time derivative of the height of an interface, z_i, chosen to separate the turbulent rotational flow from the irrotational flow:

$$w_e = \frac{d}{dt} \langle z_i \rangle \ .$$

Here, z_i is defined as the height of the $S = 0.5$ isosurface and $\langle\rangle$ denotes the horizontal averaging operator. In order to evaluate the accuracy at which the LS-LES maintains the prescribed entrainment, the simplest possible case is considered which is to prescribe zero entrainment ($w_e \equiv 0$ in Eq. (2.97)). Thus, numerical errors are separated from uncertainties in the modelling of entrainment and any net entrainment can be attributed to numerical errors. In both cases, the standard LES and the LS-LES, an estimate for the exact

entrainment is needed in order to define the error and a common reference entrainment. For this Bretherton et al.'s [8] formula

$$w_e^{\mathrm{th}}(A) = \frac{1.25A}{1+1.25A}\frac{gF_0(1-(2/K_a\rho_0 z_i))}{\rho_0 c_p \Theta_0 \Delta b} \tag{5.8}$$

is used as an estimate ('th' stands for theoretical). It is derived from Sayler and Breidenthal's[59] Richardson number scaling using a mixed layer model. A is an empirical model parameter with values of 0.2 to 0.4 as suggested by Sayler and Breidenthal's [59] experiments. The physical parameters used are listed in Tab. 8. As the buoyancy jump Δb, the value 0.25 $\mathrm{m\,s^{-2}}$ is used which is the average buoyancy difference across the inversion during the third hour of the 'D' simulations. For the given range of the A parameter, Eq. (5.8) predicts entrainment rates between

$$w_{e,\mathrm{min}}^{\mathrm{th}} = w_e^{\mathrm{th}}(0.2) = 1.24\ \mathrm{mm\,s^{-1}} \quad \text{and}$$
$$w_{e,\mathrm{max}}^{\mathrm{th}} = w_e^{\mathrm{th}}(0.4) = 2.06\ \mathrm{mm\,s^{-1}}\,.$$

With the LES generally overestimating entrainment, the two values define the worst case and best case errors, respectively. Using these two values as a reference, two relative errors are defined in the form

$$\frac{\Delta w_e}{w_e^{\mathrm{th}}} = \frac{w_e - w_e^{\mathrm{th}}}{w_e^{\mathrm{th}}} \quad . \tag{5.9}$$

5.4.2 *Standard LES*

Figure 20 shows the evolution of the inversion height for the standard LES for the 'S' and 'D' grid and the above mentioned limiter choices. All simulations show an initial transient, after which the BL depth grows quasi linearly with superimposed oscillations with a time-scale of one to two hours. The initial transient as well as the amplitude of the oscillations are reduced in the double-resolution case. Relative to the results obtained with the MC limiter, inversion heights are consistently higher with the Minmod limiter and lower with the Superbee limiter. Due to the oscillations in the standard-resolution case, this order is not always reflected in the hourly averaged entrainment rates. In order to ensure comparability with Bretherton et al.' [8] results, statistics are averaged over the third hour (i.e. 2h-to-3h averages). However, as noted by those authors, the oscillations in the standard resolution runs render statistics averaged over just one hour less reliable. For this reason 2h-to-4h averages are also considered here.

Average entrainment rates, as presented in Tab. 9, are in agreement with Bretherton et al.'s [8] intercomparison. Across our simulations, entrainment rates between 3.1 and 4.1 $\mathrm{mm\,s^{-1}}$ were observed which is within the observed range of the 3D runs of the intercomparison. As mentioned before, there is a consistent correlation between higher and lower entrainment and the limiter used. This is best seen in the 2h-to-4h averages in the second column. Minmod consistently produces greater entrainment than MC (+7.37% and +13.41% in the S and D run, respectively), and Superbee produces lower entrainment (-6.12% and -10.51%). The present simulations show a trend of increasing entrainment rates over time, consistent with Bretherton et al.' [8] results, which results from the gradual weakening of the inversion and a slight increase of cloud-top mixing due to increasing TKE over time. The increase of the entrainment rate is stronger in the standard-resolution simulations, which in part may be attributed to the phase of the oscillations of

the inversion height and in part to greater weakening of the inversion on the coarser grid. The last two columns show how entrainment rates change with grid resolution. Entrainment rates reduce as the resolution is increased which is also consistent with Bretherton et al.'s [8] observation. The reductions of more than 10% in the 2-to-3-hours averages should be considered less reliable than the 2-to-4-hours averages due to the above mentioned oscillations. The trend, however, clearly remains when considering 2h-to-4h averages.

Figure 21 shows the evolution of the horizontal average of the vertically integrated TKE density (VTKE) for the standard LES. The subgrid-scale part of the TKE is diagnosed from the filtered velocity field consistent with the Smagorinsky model (see e.g. [76]). As with the evolution of the inversion height, the VTKE exhibits an initial transient and a decaying oscillation. It eventually settles at a relatively stable magnitude after about 1.5 to 2 hours. Table 11 lists the 2h-to-4h averaged values. The data reveals a consistent ordering for the three limiters with Superbee exceeding the MC limiter by +10.12% (S) and +9.47% (D), respectively, and Minmod going below it by -23.6% (S) and -12,88% (D), respectively. This trend continues to exist in the individual profiles of the horizontal and vertical velocity variances which are shown in Fig. 22. The non-vanishing velocity variances above the cloud layer in the no-limiter case are due to scalar overshoots caused by the non-monotone advection scheme.

5.4.3 *LS-LES*

Figure 26 shows the evolution of the inversion height for the LS-LES. It exhibits a similar initial transient over a period of roughly 30 minutes after which it evolves in a quasi linear way. While there is a dependence on the limiter visible, it is minimal compared to the standard LES runs. Overall, entrainment is drastically reduced.

Table 10 compares the 2h-to-4h averaged entrainment rates for both the standard LES and the LS-LES with the rates predicted by Eq. (5.8).

On the left side are the entrainment rates compared to the lower entrainment prediction; the right side compares them to the greater predicted value. The entrainment rates w_e are the maximum and minimum values from the high resolution 'D' runs. This range of entrainment rates is representative of the overall range observed with the standard LES. It also contains the lowest one observed which is closest to theoretical predictions. The combination of lowest and highest observed entrainment and lowest and highest predicted entrainment defines the four cases for which the relative errors are presented.

In the least favourable scenario, the standard LES overestimates entrainment by 229%. This is, if the exact entrainment meets the lower bound of 1.24 $\mathrm{mm\,s^{-1}}$. In the most favourable scenario, assuming 2.06 $\mathrm{mm\,s^{-1}}$ is the exact value and choosing the minimal entrainment rate across all simulations, the overestimation reduces to 53% for the present simulations. Using the level set method, these errors are reduced by about a factor of 25 to 8% in the worst case and 2% in the most favourable scenario. It is important to note, that also the spread of the errors associated with the choice of the limiter is reduced by at least a factor of 10, namely from 74% and 45% to 4% or less.

Figure 24 shows the evolution of the VTKE for the three limiter choices with the LS-LES. Two things are immediately obvious when comparing the

Table 9: Time-averaged entrainment rates w_e (left) and their relative changes (right) with grid resolution and flux limiter choice for the standard LES. The percentages in brackets are the relative changes with respect to the MC limiter.

	w_e [mm s^{-1}]		Relative changes		
	(I) 2h - 3h average	(II) 2h - 4h average	(I) $\rightarrow$ (II)	S $\rightarrow$ D (2h - 3h avg.)	S $\rightarrow$ D (2h - 4h avg.)
(S) Standard resolution					
Minmod	3.4817 (-0.74 %)	4.1339 (+7.37 %)	+18.73 %		
MC	3.5076 $\nearrow\searrow$	3.8503 $\nearrow\searrow$	+9.77 %		
Superbee	3.3815 (-3.60 %)	3.6148 (-6.12 %)	+6.90 %		
(D) Double resolution					
Minmod	4.0396 (+15.84 %)	4.0727 (+13.41 %)	+0.82 %	-14.22 %	-1.48 %
MC	3.4841 $\nearrow\searrow$	3.5565 $\nearrow\searrow$	+2.08 %	-13.45 %	-7.63 %
Superbee	3.0984 (-11.00 %)	3.1519 (-10.51 %)	+1.73 %	-16.70 %	-12.80 %

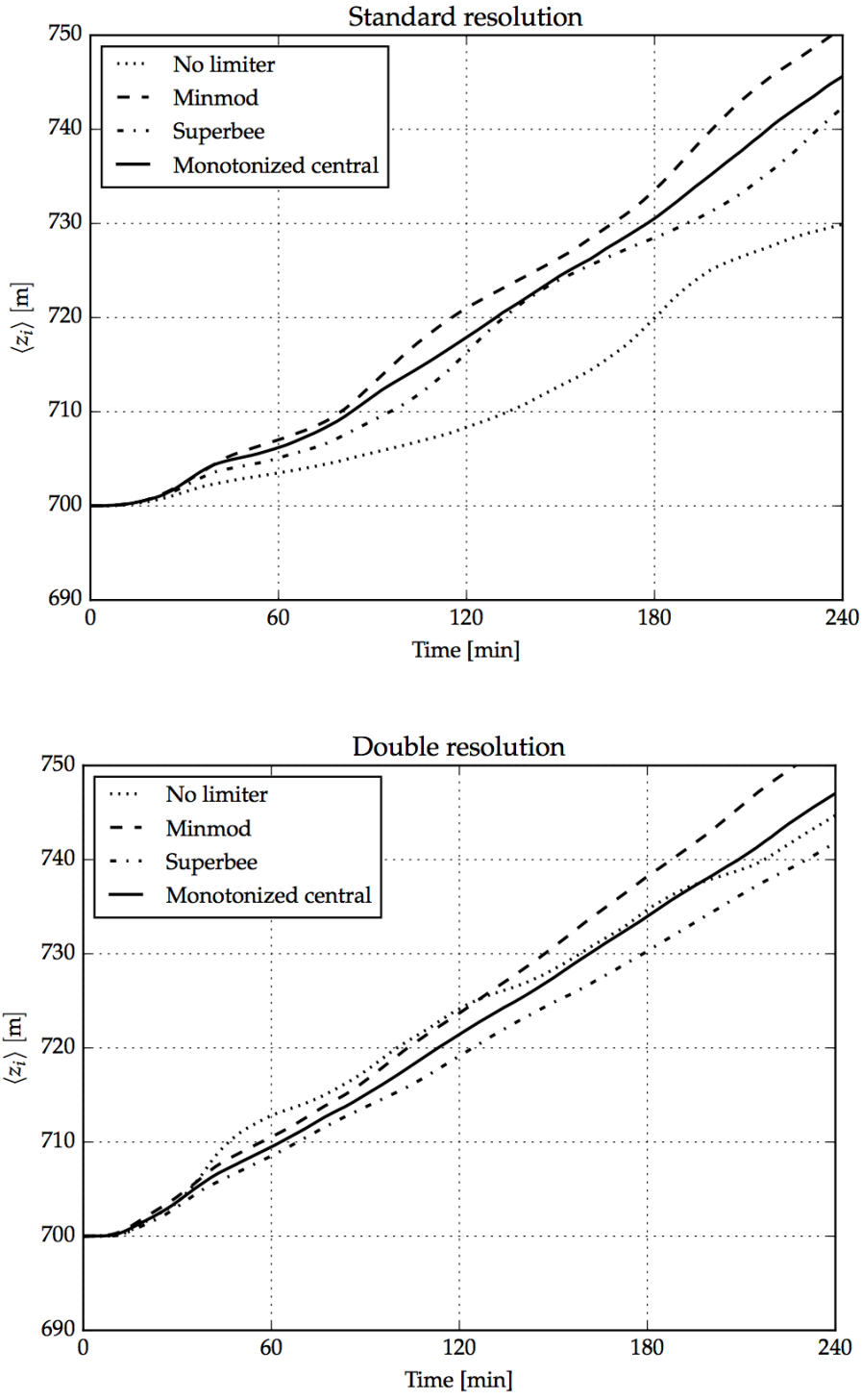

Figure 20: Evolution of the horizontally averaged cloud top height $\langle z_i \rangle$ comparing various limiter choices for the standard LES. z_i is defined as the height of the $S = 0.5$ isosurface. Top: standard resolution, bottom: double resolution.

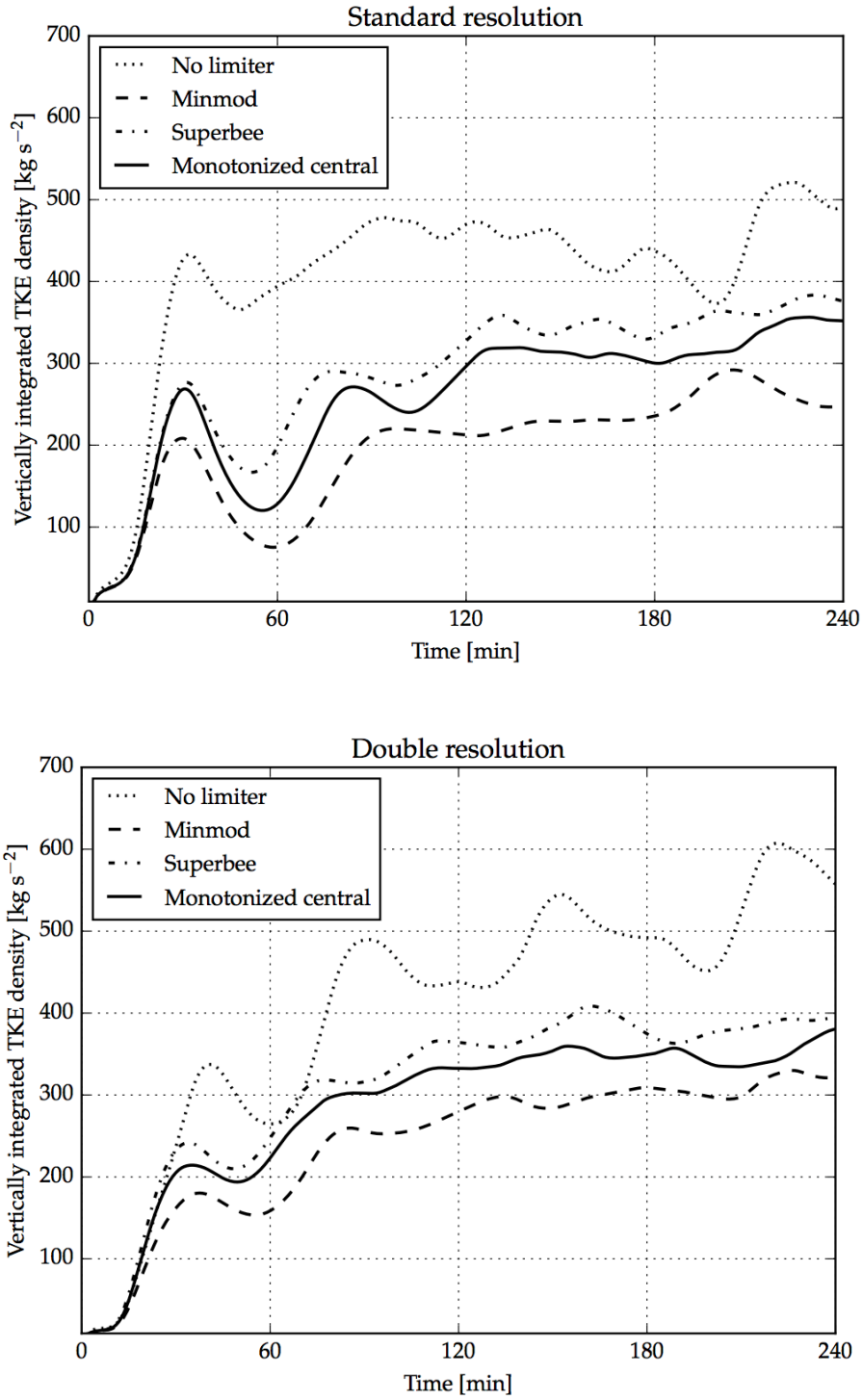

Figure 21: Evolution of the horizontal average of the vertically integrated TKE density (resolved + subgrid-scale) comparing various limiter choices for the standard LES. Top: standard resolution, bottom: double resolution.

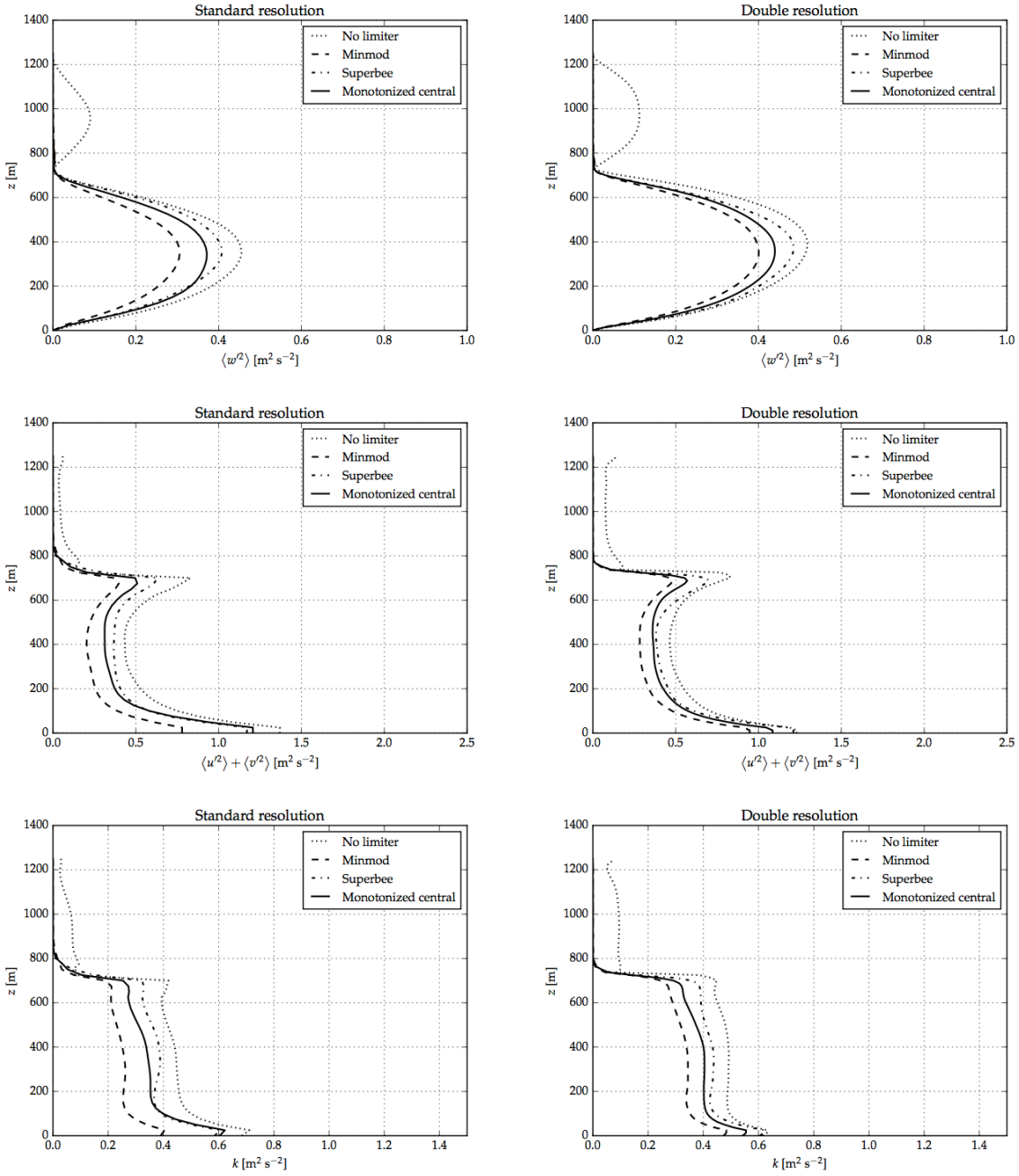

Figure 22: Profiles of various turbulence statistics of the resolved fields averaged over the third hour for the standard LES. From top to bottom, the profiles shown are the vertical velocity variance $\langle w'^2 \rangle$, horizontal velocity variance $\langle u'^2 \rangle + \langle v'^2 \rangle$, and turbulent kinetic energy $k = 1/2(\langle u'^2 \rangle + \langle v'^2 \rangle + \langle w'^2 \rangle)$, for the standard resolution (left column) and double resolution (right column).

Table 10: Entrainment rates w_e and their relative errors of the double-resolution runs of the standard LES and the LS-LES. Relative errors according to Eq. (5.9) are shown with respect to the minimum (left major column) and maximum (right major column) entrainment estimate. Each column subdivides into the case of lowest and highest entrainment across the three limiters.

	$w_e^{\text{th}} = 1.24\ \text{mm s}^{-1}$		$w_e^{\text{th}} = 2.06\ \text{mm s}^{-1}$	
	lowest w_e	greatest w_e	lowest w_e	greatest w_e
Std. LES				
w_e [mm s^{-1}]	3.1519	4.0727	3.1519	4.0727
Δw_e [mm s^{-1}]	1.9147	2.8354	1.0899	2.0106
$\Delta w_e / w_e^{\text{th}}$	+155 %	+229 %	+53 %	+98 %
LS-LES				
Δw_e [mm s^{-1}]	0.0465	0.1019	0.0465	0.1019
$\Delta w_e / w_e^{\text{th}}$	+4 %	+8 %	+2 %	+5 %

Table 11: 2h-to-4h averages of the vertically integrated TKE

	VTKE [kg s^{-2}]	
Limiter	Standard LES	LS-LES
(S) Standard resolution		
Minmod	244.80	580.08
MC	320.40	533.94
Superbee	352.83	572.76
(D) Double resolution		
Minmod	302.11	579.63
MC	346.78	541.30
Superbee	379.62	535.79

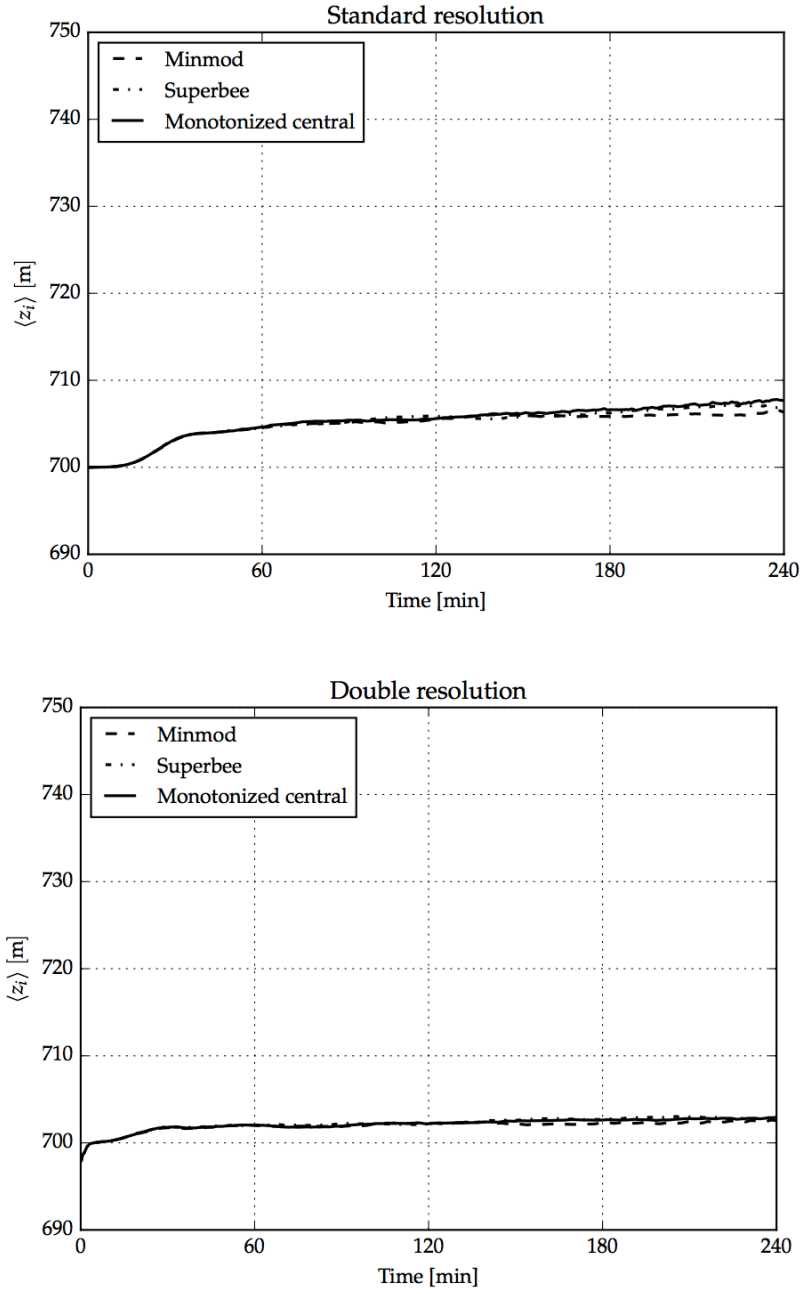

Figure 23: Evolution of the horizontally averaged cloud top height $\langle z_i \rangle$ comparing various limiter choices for the LS-LES. z_i is defined as the height of the $S = 0.5$ isosurface. Left: standard resolution, right: double resolution.

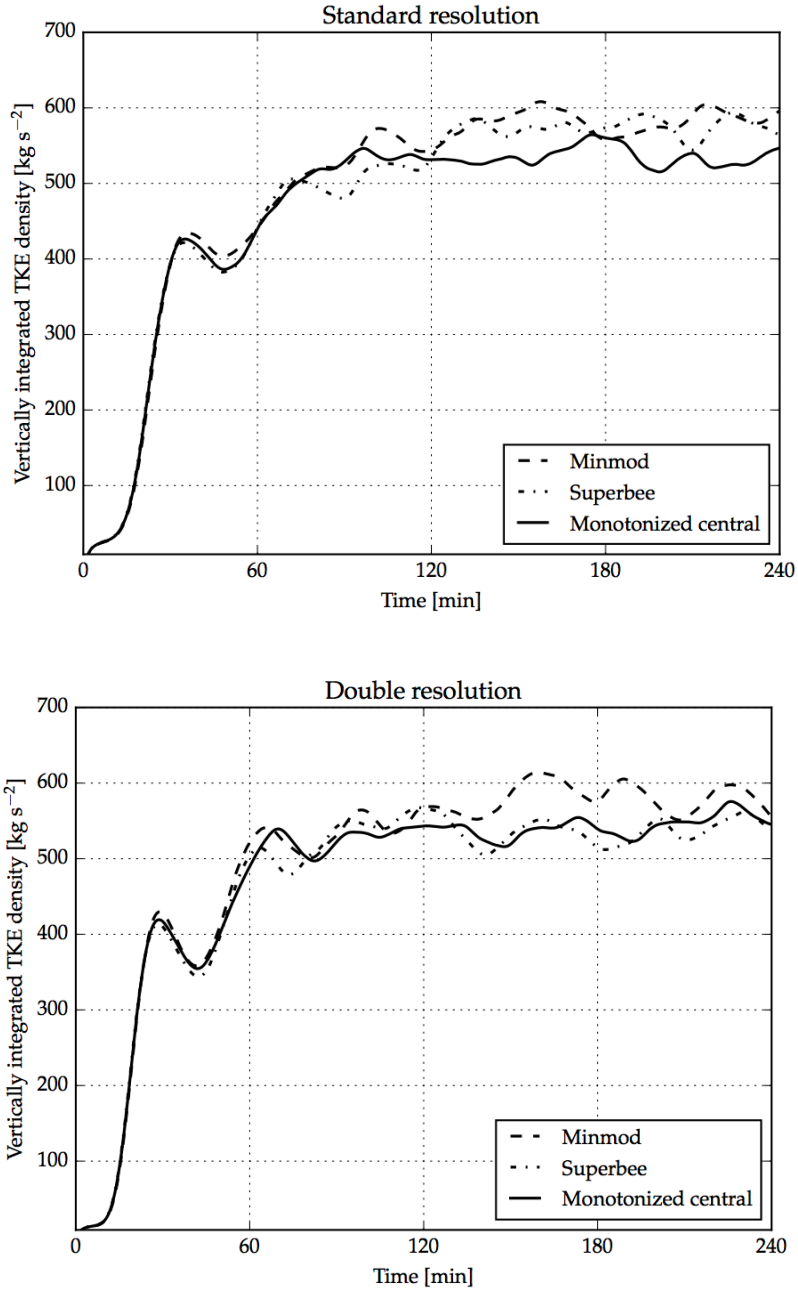

Figure 24: Evolution of the horizontal average of the vertically integrated TKE density (resolved + subgrid-scale) comparing various limiter choices for the LS-LES. Left: standard resolution, right: double resolution.

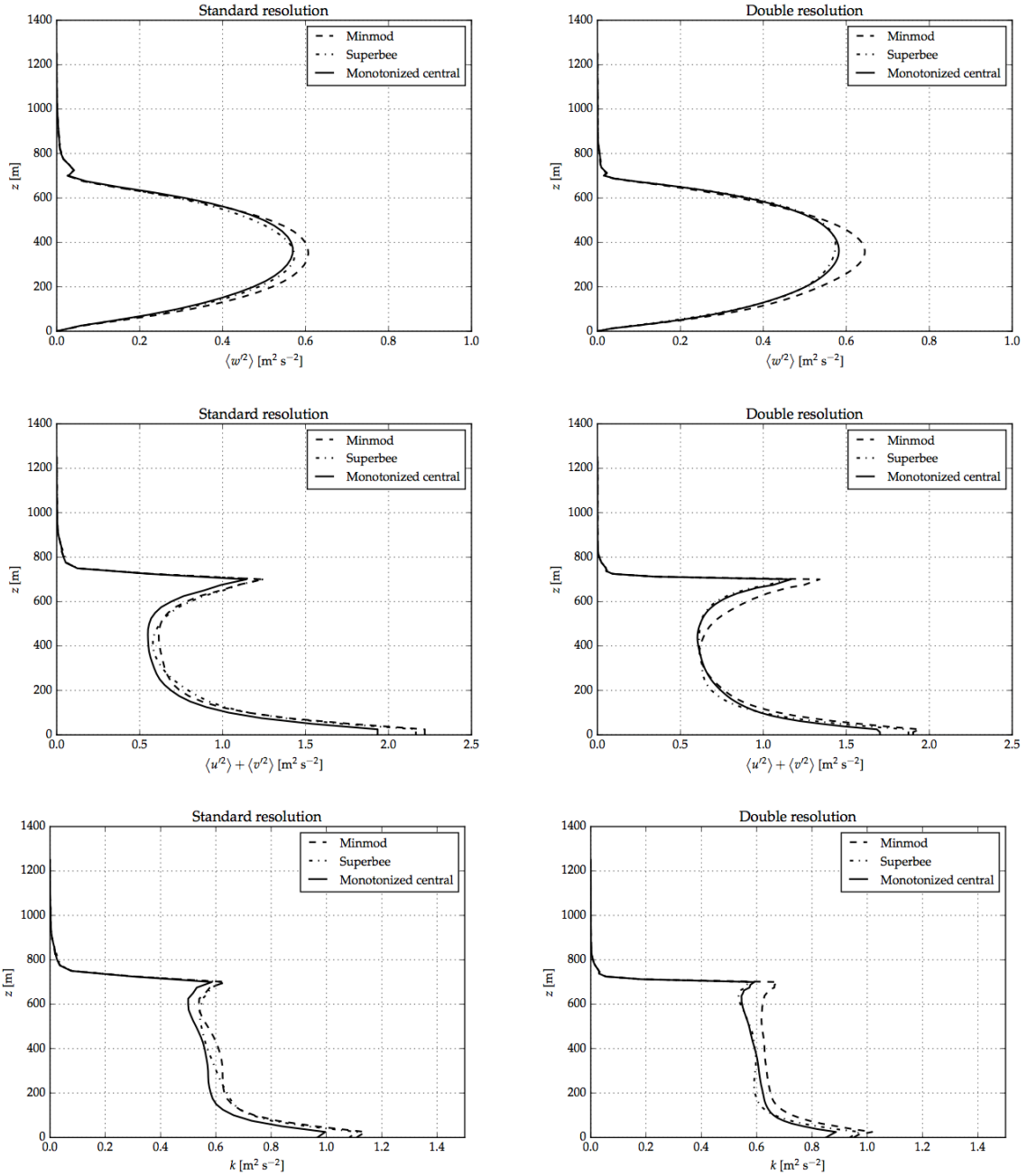

Figure 25: Profiles of various turbulence statistics of the resolved fields averaged over the third hour for the LS-LES. From top to bottom, the profiles shown are the vertical velocity variance $\langle w'^2 \rangle$, horizontal velocity variance $\langle u'^2 \rangle + \langle v'^2 \rangle$, and turbulent kinetic energy $k = 1/2(\langle u'^2 \rangle + \langle v'^2 \rangle + \langle w'^2 \rangle)$, for the standard resolution (left column) and double resolution (right column).

plots with the ones for the standard LES. First, VTKE levels are higher; they are increased by about 80%. And second, the dependency of the VTKE on the limiter is reduced. Table 11 lists 2h-to-4h averaged values of the vertically integrated TKE for both the standard LES and LS-LES. The higher VTKE levels can be explained in terms of the missing entrainment in the LS-LES runs. Entrainment reduces TKE, primarily, because the potential energy of the BL fluid is increasing as less dense fluid from aloft is being mixed into the BL leading to a deeper layer of dense fluid. In addition, work needs to be done in order to accelerate entrained parcels being previously at rest. At the same time, the radiative cooling reduces as the smoke concentration is progressively reduced due to mixing with the warmed air entrained from above. This reduces the buoyant production of TKE in the first place. All of these processes, when absent, tend to increase TKE in the BL. In fact, this is consistently seen across all simulations. The simulations featuring lower entrainment rates, exhibit higher TKE levels and vice versa. The simulations using the level set method, having vanishing net entrainment, exhibit the highest TKE levels.

The 2h-to-3h averaged profiles of the TKE and their vertical and horizontal components, shown in Fig. 25, reflect that increase. Besides the greater magnitude, another interesting feature is the sharper peak in the variance of the horizontal velocity compared to the standard LES (Fig. 22). Here, a similar reasoning applies as with the TKE magnitude. In the absence of entrainment at the cloud top, TKE is dissipated more weakly, resulting in higher levels close to the cloud top. Also, the sharper inversion deflects the vertical motions more strongly towards horizontal motions.

Overall, the dependency of turbulence statistics on the limiter is reduced compared to the standard LES results. The effect of flux limiters on the advection scheme is strongest in regions where second derivatives are great. This is especially the case close to the cloud top. In the level set framework the discontinuous cloud-top problem is replaced by two smooth ones based on the ghost fluids. Thus, the effects of a limiter near the cloud top are much reduced and the dependence on any specific limiter reduces also. Some dependence, however, remains in the interior of the flow.

5.5 SUMMARY AND CONCLUSIONS

Large-eddy simulation of a radiatively driven convective boundary layer filled with optically thick smoke, often simply referred to as 'smoke cloud' have been carried out. This case was the object of the LES intercomparison study by Bretherton et al. [8] and this is the setup that was used here. Simulations were run with the standard version of the LES as reference, as well as simulations with the level set method enabled. With the level set method enabled, zero entrainment was prescribed. This served as test case to analyse the accuracy of the presented front-tracking algorithm. Two parameters were varied—the grid resolution and the flux limiter for scalar advection—and their influence on statistics of the flow was quantified. The analysis focussed specifically on the entrainment rate and the turbulent kinetic energy. Using an empirically-based entrainment law, an upper and lower bound of entrainment errors were estimated and the improvements achieved using the level set method were discussed.

The entrainment rates and turbulence statistics measured with the standard LES closely resembled those observed in Bretherton et al.'s [8] intercomparison. Entrainment was overestimated in all of these simulations by

at least 50%, on the coarser grid by more than 150%. Increasing the grid resolution reduced simulated entrainment across all runs which is a tendency typically observed in LES of cloud-top entrainment. With the level set method, the prescribed entrainment was maintained with errors less than 5-10%. At the same time, the dependence of the entrainment errors on the choice of the limiter was reduced by more than a factor of 10.

6

CONTROLLING ENTRAINMENT IN THE STRATOCUMULUS-TOPPED ATMOSPHERIC BOUNDARY LAYER

The code that was used to produce the simulation results presented in this chapter is available on GitHub:

https://github.com/uclales/uclales/tree/level-set-stbl .

6.1 INTRODUCTION

In this chapter, the front-tracking algorithm is applied to the stratocumulus-topped boundary layer (STBL). It is shown that its use in the University of California, Los Angeles Large-Eddy Simulation (UCLA-LES) yields similar benefits as in the case of the smoke cloud, despite the increased complexity of the case.

The STBL is different from the smoke cloud case considered in the last chapter in a number of ways. The central difference is the presence of moisture which allows for condensation and evaporation and the associated release and consumption of latent heat. Furthermore, the boundary conditions are more complex. Instead of zero-flux boundary conditions at the bottom, the ocean supplies the boundary layer (BL) with fluxes of heat and moisture. At the same time, relatively warm and dry tropical air from aloft, supplied by the Hadley circulation, steadily subsides on the BL tending to increase stratification. As a result, the potential temperature profile, which was constant above the smoke cloud BL, now features a positive lapse rate. In addition to the more complex thermodynamics, the momentum in the BL is affected by Coriolis forces, which where ignored in the smoke cloud.

The simulation setup is based on the stratocumulus cloud field observed during research flight 1 (RF01) of the Dynamics and Chemistry of Marine Stratocumulus (DYCOMS) II field study. The same setup was used by Stevens et al. [79] in their large-eddy simulation (LES) intercomparison. The DYCOMS II field study [77, 78] took place in July 2001, over the Pacific Ocean approximately 500 km west-southwest of San Diego, California, USA. It consisted of nine research flights, six of which, including RF01, were carried out during the night [77].

Stevens et al. [79] chose RF01 in particular for the LES intercomparison because it combined a number of favourable features. First of all, nocturnal flights are favoured because the radiative forcing of nocturnal stratocumulus is simpler and more stationary than during the day. This made it easier to estimate entrainment rates under strong subsidence from the energy budget of the STBL. They estimated the entrainment rate to be

$$w_e^{\text{est}} = (3.8 \pm 1)\,\text{mm}\,\text{s}^{-1} \quad . \tag{6.1}$$

In addition, the environmental conditions were relatively homogeneous and no appreciable drizzle was present. Research flight 1 was especially appealing for an LES intercomparison because of another aspect. As Stevens et al. [77] point out, the BL observed during RF01 is unstable according to Deardorff [13] and Randall's [55] cloud-top entrainment instability (CTEI) criterion. According to their theory, the cloud would rapidly dissolve due to a

runaway instability caused by buoyancy reversal (cf. Chapt. 4.1). But in reality, the cloud persisted. Whether or not the CTEI occurs according to the theory is indicated by the parameter κ exceeding a critical value κ^*. The critical value for the conditions of RF01 is $\kappa^* = 0.23$ which is far exceeded by the actual value of $\kappa = 0.45$ [79], and still the cloud persists. In fact, Stevens et al. [77] estimate that the cloud even deepens by several metres per hour. Although the runaway instability leading to a complete dissipation of the cloud was not seen in any of the simulations, most of them showed partial dissipation and more broken, thinner clouds.

6.2 FORMULATION

6.2.1 *Governing equations*

The evolution of the STBL is simulated using the moist anelastic LES equations, Eqs. (2.85) to (2.87), with additional forcings, namely the inclusion of a subsidence term in the scalar equations, radiative cooling in the temperature equation, and Coriolis forces in the momentum equations. The presence of subsidence requires some further discussion since (i) it is modelled in the anelastic system and (ii) since it affects how entrainment is measured in the simulation.

The net growth of the BL depth results from the balance of the large-scale subsidence and entrainment of warm fluid into the turbulent BL. As a result, entrainment in the simulations can be measured as

$$w_e = \frac{d\,\langle z_i \rangle}{dt} - w_s \quad , \tag{6.2}$$

where w_s is the mean subsidence velocity at $z = \langle z_i \rangle$. Both, w_e and w_s, are comparable in magnitude and are expected to have values of several $\mathrm{mm\,s^{-1}}$. The mean subsidence velocity results from an inflow from aloft driven by the Hadley circulation and an according outflow in the lateral directions that satisfies mass conservation. However, the anelastic equations were derived under the requirement that the fluid does not penetrate the top and bottom boundaries and that the flow is laterally periodic, i.e. there is no mean outflow (cf. Eq. (2.35)). (The anelastic equations can also be derived with the more restrictive no-penetration boundary conditions in the lateral, which results in the same conclusion.) From this resulted the fact that the zeroth-order density, ρ_0, is constant in time and only a function of the height. In order to satisfy said boundary conditions, the effect of subsidence has to included in a different way. In the UCLA-LES, this is done by prescribing an additional forcing in the scalar equations in the form of a non-conservative transport term, e.g. for the temperature $\boldsymbol{w}_s \cdot \nabla\theta_l$, where $\boldsymbol{w}_s = (0, 0, w_s)^T$. If this non-conservative term is expanded as

$$\boldsymbol{w}_s \cdot \nabla\theta_l = \frac{1}{\rho_0}\left(\nabla \cdot (\rho_0 \theta_l \boldsymbol{w}_s) - \theta_l \nabla \cdot (\rho_0 \boldsymbol{w}_s)\right) \quad , \tag{6.3}$$

it can be seen that it models conservative advective transport in the vertical plus a divergence that reflects the lateral outflow in reality in the laterally periodic model. The mean subsidence velocity w_s is modelled as a function of height according to

$$w_s(z) = -Dz \tag{6.4}$$

where D is the divergence of the large scale winds. Thus, $w_s(z)$ satisfies zero-penetration boundary conditions at the bottom. The divergence D is

Table 12: Physical parameters for the STBL

Isobaric heat capacity of moist air	c_p	1015	$\mathrm{J\,(kg\,K)^{-1}}$
Enthalpy of vaporization of water	L_v	2.46×10^6	$\mathrm{J\,kg^{-1}}$
Gravitational acceleration	g	9.8	$\mathrm{m\,s^{-2}}$
Reference pressure	p_{00}	1000	hPa
Reference temperature	Θ_0	289	K

set to $3.75 \times 10^{-6}\,\mathrm{s^{-1}}$ yielding a mean subsidence velocity of approximately $3\,\mathrm{mm\,s^{-1}}$ at the initial inversion height of 840 m in RF01.

With the modifications discussed above, the anelastic system becomes

$$\frac{\partial \bar{\boldsymbol{v}}}{\partial t} + \frac{1}{\rho_0}\nabla\cdot(\rho_0 \bar{\boldsymbol{v}} \otimes \bar{\boldsymbol{v}}) = c_p \Theta_0 \nabla \bar{\pi} + \frac{g\bar{\theta}_v'}{\Theta_0}\boldsymbol{k} + \boldsymbol{f}_k \times (\bar{\boldsymbol{v}} - \boldsymbol{v}_g) + \frac{1}{\rho_0}\nabla\cdot(\rho_0 \boldsymbol{\tau}) \quad , \tag{6.5}$$

$$\frac{\partial \bar{\theta}_l}{\partial t} + \frac{1}{\rho_0}\nabla\cdot(\rho_0 \bar{\theta}_l \bar{\boldsymbol{v}}) = \frac{1}{\rho_0}\nabla\cdot(\rho_0 \boldsymbol{\gamma}_{\theta_l}) + Dz\frac{\partial \theta_l}{\partial z} - \frac{1}{\rho_0 c_p}\frac{\partial F_{\mathrm{rad}}}{\partial z} \quad , \tag{6.6}$$

$$\frac{\partial \bar{q}_t}{\partial t} + \frac{1}{\rho_0}\nabla\cdot(\rho_0 \bar{q}_t \bar{\boldsymbol{v}}) = \frac{1}{\rho_0}\nabla\cdot(\rho_0 \boldsymbol{\gamma}_{q_t}) + Dz\frac{\partial q_t}{\partial z} \quad , \tag{6.7}$$

$$\nabla\cdot(\rho_0 \bar{\boldsymbol{v}}) = 0\,, \quad . \tag{6.8}$$

Herein, $\boldsymbol{f}_k = (0, 0, f)^{\mathrm{T}}$ models the Coriolis forces. The Coriolis parameter is given by $f = 2\Omega\sin(\phi)$ with the mean angular velocity of Earth[1] of $\Omega = 7.292 \times 10^{-5}\,\mathrm{s^{-1}}$ and the latitude ϕ where the RF01 took place of 31.5N. (The flight path and location is shown, for instance, in Fig. 2 in [78].) Furthermore, $\boldsymbol{v}_g = (7\,\mathrm{m\,s^{-1}}, -5.5\,\mathrm{m\,s^{-1}}, 0)^{\mathrm{T}}$ is the geostrophic wind vector. The values of all other parameters are chosen following Stevens et al. [79] and are listed in Tab. 12.

6.2.2 *Initial and boundary conditions*

The same initial and boundary conditions were chosen as specified by Stevens et al. [79] for their intercomparison. The domain extends over 3.36 km in the two lateral directions and over 1.5 km in the vertical direction. The cloud top interface of the STBL is initially located at $z_i = 840\,\mathrm{m}$ with the initial profiles of total water and liquid water potential temperature being

$$\theta_l(z) = \begin{cases} 289.0\,\mathrm{K} & \text{if } z \le z_i \\ 297.5\,\mathrm{K} + (\frac{z - z_i}{\mathrm{m}})^{1/3}\,\mathrm{K} & \text{if } z > z_i \end{cases} \tag{6.9}$$

$$q_t(z) = \begin{cases} 9.05\,\mathrm{g\,kg^{-1}} & \text{if } z \le z_i \\ 1.50\,\mathrm{g\,kg^{-1}} & \text{if } z > z_i \end{cases} \tag{6.10}$$

The surface pressure is set to 1017.8 hPa and the sea surface temperature (SST) is 292 K. As in the smoke cloud simulations in Chapt. 5, all temperature values below 650 m where perturbed by a spatially uncorrelated uniform random noise in order to trigger the spin-up of the BL convection. The amplitude of the noise was set to ± 0.1 K. The boundary layer is initially at rest. The domain is periodic in the two lateral directions and free-slip boundary

1 The angular velocity $\Omega = 2\pi * (24 * 3600. - 4 * 60. + 4.1)$ corresponds to one stellar day.

conditions are imposed at the top and bottom. For scalars, Neumann boundary conditions are set: At the top, zero-gradient boundary conditions are set and at the surface, a constant sensible heat fluxes of $15\,\mathrm{W\,m^{-2}}$ and latent heat flux of $115\,\mathrm{W\,m^{-2}}$ are imposed. A sponge layer is used occupying the top ten grid levels. The STBL is simulated for a period of four hours.

6.2.3 *Details of the front-tracking algorithm*

The front-tracking algorithm is used as presented in Sect. 3.3. In summary, both scalars are coupled to the level set using both advective and diffusive coupling. The level set synchronisation with the scalars is based on the extrapolated fields for both q_t and θ_l. The conservation error associated with the synchronisation method was below 4 % (0.2 %) of the initially contained water mass (thermal energy).

Subsidence is included as an additional velocity component in the level set equation, i.e. Eq. 2.97 becomes

$$\frac{\partial \phi}{\partial t} + (\boldsymbol{v} - Dz\boldsymbol{k}) \cdot \nabla \phi = 0 \quad , \tag{6.11}$$

where $\boldsymbol{k}$ is the vertical Cartesian unit vector.

6.3 SIMULATION AND RESULTS

6.3.1 *Goals and setup*

The goal of this study is to assess the accuracy of the front-tracking algorithm for the more complex conditions of the STBL (as compared to smoke cloud). In particular, the STBL features a positive lapse rate above the inversion, latent heat effects, as well as more complex boundary conditions with non-zero transfer of latent and sensible heat at the surface and large scale subsidence from the top. In this study, zero entrainment is prescribed in all simulations. Thus, net entrainment can be attributed to numerical errors in the front-tracking algorithm.

The STBL is simulated using the standard UCLA-LES as well as the level set LES (LS-LES). Two different configurations are investigated: simulations of RF01 excluding subsidence and simulations with the prescribed subsidence. Both configurations are simulated on three differently resolved grids: the standard resolution of $96 \times 96 \times 150$ grid cells, corresponding to grid spacings of $35\,\mathrm{m} \times 35\,\mathrm{m} \times 10\,\mathrm{m}$, as well as twice and half that resolution. The standard resolution is what was also used in Stevens et al.'s [79] intercomparison study. This gives a total of 12 simulations, six for both the configuration with and without prescribed subsidence.

The analysis of the results mainly focusses on how well the front-tracking algorithm maintains the prescribed zero entrainment under both conditions and on how turbulence statistics change as compared to simulations using the standard UCLA-LES. Because it is assumed that LESs of the STBL similarly depend on the choice of the flux limiter, this parameter is not investigated and the MC limiter is used in all simulations.

6.3.2 *Entrainment*

Figure 26 shows the evolution of the inversion height for both the configuration with and without prescribed subsidence. Following Stevens et al. [79],

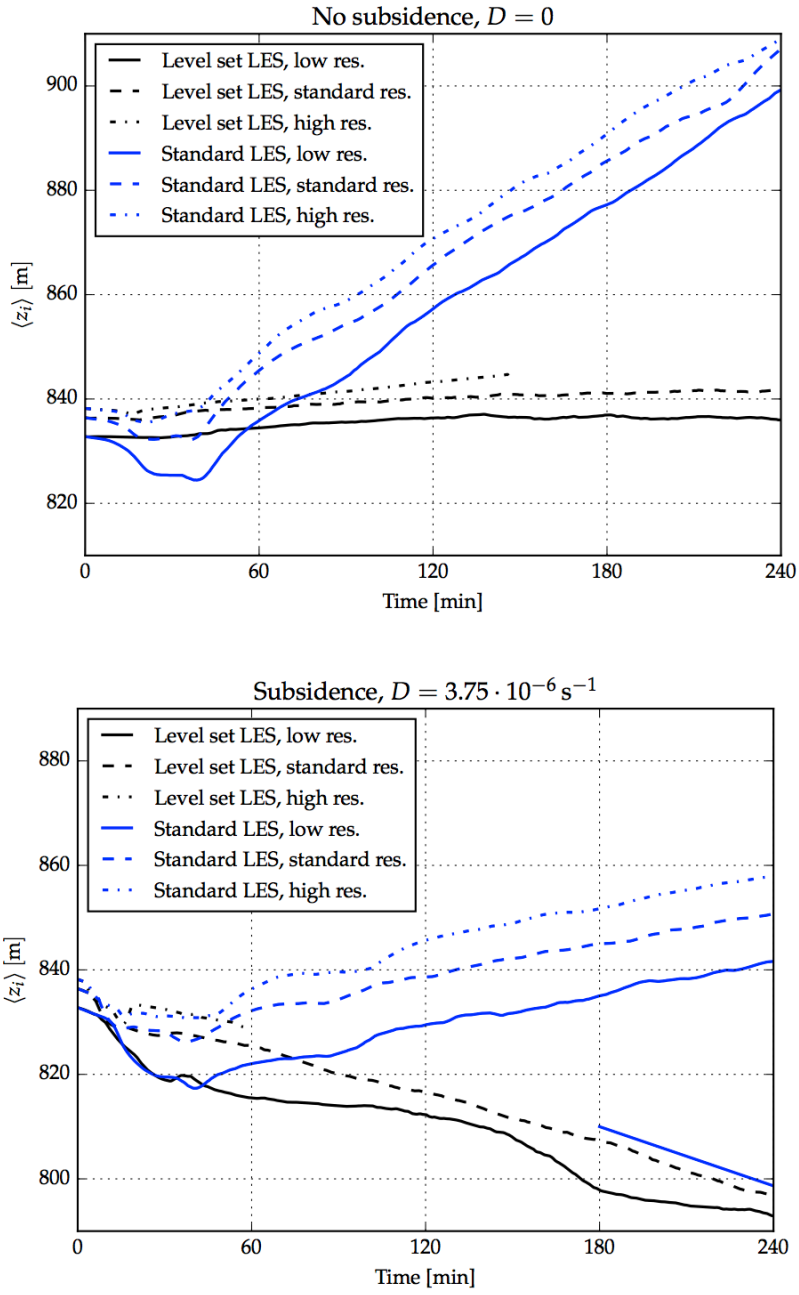

Figure 26: Evolution of the horizontally averaged cloud top height $\langle z_i \rangle$ for the case excluding (top) and including subsidence (bottom). The cloud-top height is defined as the height of the $q_t = 8\,\mathrm{g\,kg^{-1}}$ isosurface. The blue slope in the bottom plot indicates the subsidence rate at 810 m according to Eq. (6.4).

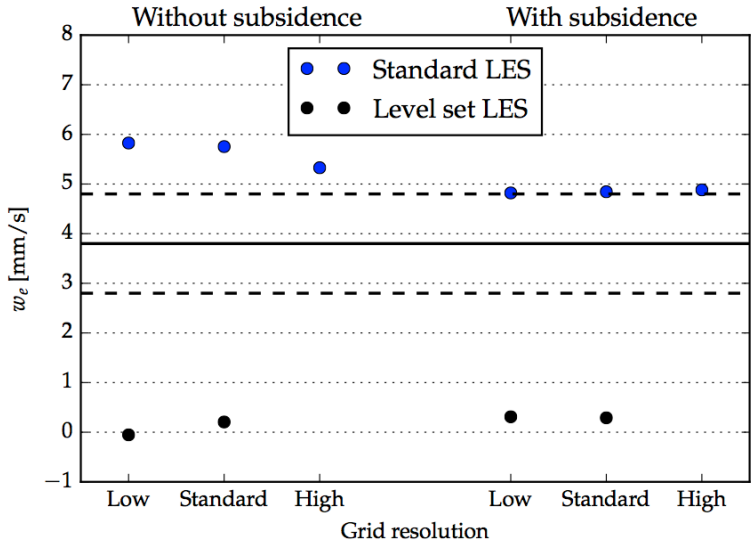

Figure 27: Entrainment rates in a simulated STBL for the case including (left) and excluding subsidence (right). The solid and dashed black lines indicate Stevens et al.'s [77] estimate of the entrainment rate and its uncertainty of $w_e^{\text{est}} = (3.8 \pm 1)\,\text{mm}\,\text{s}^{-1}$.

the inversion height is measured by the average height of the $q_t = 8\,\text{g}\,\text{kg}^{-1}$ isosurface. The graph for the high resolution run ends prematurely due to an yet unresolved error in the code which causes the simulation to terminate. (One possible reason for this may be the presence of overturning waves which become more likely as the grid is refined. The level-set coupling of the vertical implicit diffusion problem is not designed to handle multiple sections of the same fluid in one column. This eventuality was, however, not investigated further.) For this reason data from these runs are omitted in the following discussion.

Generally, the simulated STBL behaves analogous to the smoke cloud BL. After an initial transient, the BL depth changes quasi linearly but much more steadily with less oscillation than in the smoke cloud case. Using the LS-LES, boundary layer growth is drastically reduced approaching the prescribed zero growth (in the case without subsidence) or approaching the subsidence rate (indicated by the blue slope in the bottom plot of Fig. 26).

The inversion height in the plots in Fig. 26 are located slightly below the anticipated 840 m mark initially and this shift depends on the grid resolution. The reason is that the $q_t = 8\,\text{g}\,\text{kg}^{-1}$ level is located below the centre of the jumps in the scalar profiles if they are initialized according to Eqs. (6.9) and (6.10). As the grid is refined, the initial $q_t = 8\,\text{g}\,\text{kg}^{-1}$ height approaches the inversion height specified in Eq. (6.10). This shift was not seen in the smoke cloud simulations because $S = 0.5$ was used as an indicator for the location of the cloud-top interface which is located in the centre of the valid interval for S of $[0, 1]$. The initial decrease of the inversion height seen in the standard LESs is caused by an initial transient in the total water profile. Turbulent mixing during the simulation spin-up blurs the cloud-top interface lowering the $q_t = 8\,\text{g}\,\text{kg}^{-1}$ height. If present, the subsidence of rate Dz_i further adds to this decrease.

Table 13: Entrainment rates w_e and their relative errors averaged over the last two hours. The table compares entrainment rates in the standard-resolution runs of the standard LES and the LS-LES. Relative errors according to Eq. (5.9) are shown with respect to Stevens et al.'s [77] entrainment estimate of $w_e^{\text{est}} = 3.8\,\text{mm}\,\text{s}^{-1}$.

	Without subsidence	With subsidence
Std. LES		
w_e [mm s^{-1}]	5.7542	4.8446
Δw_e [mm s^{-1}]	–	1.0446
$\Delta w_e / w_e^{\text{th}}$	–	+27.5 %
LS-LES		
Δw_e [mm s^{-1}]	0.2064	0.2904
$\Delta w_e / w_e^{\text{th}}$	+5.4 %	+7.6 %

Figure 27 compares the average entrainment rates over the last two hours of all simulations with Stevens et al.'s [77] estimate indicated by the solid black line. The entrainment rates were computed using Eq. (6.2) where the subsidence rates, w_s, were computed using Eq. (6.4) with the individual average inversion height used for z.

Generally, the STBL entrains more efficiently if no subsidence is present. Given the positive lapse rate above the STBL, subsidence will increase the temperature stratification at the cloud top reducing the entrainment rate as compared to the cases with weak or no subsidence. Thus, higher entrainment rates are to be expected in the simulation with no subsidence which is shown by the data in Fig. 27. However, in this case, Stevens et al.'s [77] entrainment estimate is not valid anymore.

Entrainment rates in the simulations with subsidence fall within the spread of entrainment rates found in Stevens et al.'s [79] intercomparison. All standard LES exceed the estimated entrainment for RF01, but with values barely greater than the upper error bound of the estimate. For all runs, entrainment is less sensitive to the grid resolution than it was in the smoke cloud case. For the standard LES with subsidence, entrainment reduces from low to standard resolution and from standard to high resolution by only -1.2 % and -7.4 %, respectively. There is almost no dependency of entrainment on the grid resolution in the case including subsidence with entrainment only increasing by +0.5 % and 0.8 %, respectively.

Table 13 lists entrainment rates of Fig. 27 for the standard resolution. Using the estimate (6.1) as a reference, relative errors of the entrainment rates for the standard LES and LS-LES are listed. In case of the standard LES, the entrainment error is measured by the difference to the estimate. For the LS-LES, the entrainment rate itself represents the error since the prescribed entrainment is zero. In the absence of an appropriate estimate for the standard LES, errors are omitted in this case. With errors of less than 30 % with respect to Stevens et al.'s estimate, entrainment is predicted more accurately for the STBL than the smoke cloud where errors where between 50 and more than 200 %. As with the smoke cloud, entrainment errors were reduced to 8 % or below using the front-tracking algorithm.

6.3.3 *Turbulence statistics*

There are similar effects on the turbulent kinetic energy (TKE) components and vertically integrated TKE density (VTKE) as in the smoke cloud when using the level set method. First, the overall TKE levels measured by the VTKE increase when using the level set method (see Fig. 28 in Appendix C). In the case of the STBL they increase by a factor of about 2 with and without subsidence being present. As with entrainment rates, no significant dependency on the grid resolution is apparent. Including subsidence tends to decrease VTKE for both the standard LES and the LS-LES. These trends are reflected by the horizontal and vertical velocity variances shown in Fig. 29. While the horizontal variance profiles also show minimal dependency on the grid resolution, the vertical variances respond more strongly to changes in resolution. Since the TKE profiles are dominated by the horizontal variances, its dependence on resolution is less pronounced.

The difference of the TKE levels between the standard LES and the LS-LES can be explained the same way as in the smoke cloud simulations. With the lack of entrainment, the mean potential energy of the BL fluid is not increased at the cost of TKE. This is best illustrated by time-averaged profiles of the turbulent buoyancy flux $\langle b'w' \rangle$ shown in Figs. 30 and 31 in Appendix C. A positive turbulent buoyancy flux in the BL indicates that relatively buoyant air is moving upwards and less buoyant air is moving downwards. In a STBL, where convection is driven by cooling from the top, this is naturally the case below the cloud top. The turbulent buoyancy flux appears in the TKE budget (not shown) as a source term, i.e. a positive buoyancy flux also indicates buoyant generation of TKE. The turbulent buoyancy flux can also be negative inside the BL, which would in turn indicate that TKE is consumed in the mean in order to lift heavier fluid. The buoyancy flux profiles in Figs. 30 and 31 reveal that in the LS-LES (black lines) much more buoyant production of TKE of occurs, especially in the core of the BL. In contrast, in the standard LES even negative buoyancy fluxes occur in some cases, albeit having small magnitude. Similarly, simulations without subsidence tend to show greater buoyancy fluxes yielding higher VTKE levels.

6.4 SUMMARY AND CONCLUSIONS

Large-eddy simulations of the stratocumulus-topped boundary layer (STBL) with and without the front-tracking algorithm were presented. The setup of the STBL was based on the research flight 1 of the DYCOMS II field study as specified Stevens et al. [79]. Two different szenarios were considered, one where there is no large-scale subsidence present and one where there is. For both scenarios, simulations at three different grid resolutions were carried out. When using the front-tracking algorithm, zero entrainment was prescribed. Based on Stevens et al.'s [77] estimate of the cloud-top entrainment rate for the case, the entrainment errors of the standard LES and the front-tracking algorithm estimated. Furthermore, the effect of enforcing vanishing entrainment on turbulence statistics of STBL using the front-tracking algorithm were investigated.

Given the similarities of the STBL and the smoke cloud discussed in Chapt. 5, similar observations have been made for the STBL. Entrainment was overestimated in all simulations using the standard LES by about 27 % compared to Stevens et al.'s [77] estimate. The front-tracking algorithm can control the prescribed zero-entrainment in both cases, with and without subsidence,

with errors less than 8 %. In contrast to the smoke cloud simulation, entrainment and other statistics showed a reduced dependency on the grid resolution.

Assuming the correct entrainment is closer to the estimated $3.8\,\mathrm{mm\,s^{-1}}$ than to the upper error bound, it seems that much higher resolution is needed in LES to converge to the correct value. On the other hand, the simulations reveal that LES already approaches the error margins of data derived from the DYCOMS II field campaign and the entrainment errors of the front-tracking algorithm are well below that. Thus, further analysis of this algorithm should be focussed on comparisons against field observations with less uncertainty and especially against high-resolution simulations such as the ones carried out by Mellado et al. [40, 46] and deLozar and Mellado [10, 11] for dry as well as moist mixing layers.

7 SUMMARY AND OUTLOOK

A front-tracking algorithm for cloud-topped boundary layers under strong inversions based on the level set method has been developed. The main goal of this algorithm is to separate numerical and physical mixing at the cloud top inversion by representing it as a discontinuity instead of resolving it on the grid. The level set method solves an additional transport equation for a monotone scalar function which implicitly defines the location of the cloud-top interface as its zero isosurface. Interface boundary conditions are supplied using the ghost-fluid method. The algorithm has been implemented in a finite-volume incompressible atmospheric flow solver, the University of California, Los Angeles Large-Eddy Simulation (UCLA-LES), which is based on the anelastic limit of the Navier-Stokes equations. The algorithm couples both the explicit advection scheme and the semi-implicit diffusion scheme for scalar transport to the level set method. Momentum transport and the associated Poisson problem is kept as is.

The issue of numerical mixing at the cloud top is investigated by analysing the behaviour of the UCLA-LES for an idealized two-dimensional cloud top mixing case in the limit of direct numerical simulation (DNS) resolutions. For this, the original UCLA-LES code, which uses a globally second-order scheme, was compared to a DNS solution, based on a spectral-like compact sixth-order accurate method. The subgrid-scale turbulence model of the UCLA-LES code was switched off and a constant molecular viscosity was used instead so that only numerical effects were addressed. A grid convergence study was carried out in order to investigate the sensitivity of the solution to numerical errors and the resolution requirements for the UCLA-LES algorithm to achieve convergence. It was shown that the UCLA-LES code meets the anticipated second-order rate of convergence and that it converges to the DNS solution. It was found that the high-order method solves the problem much more efficiently, despite its higher computational cost per iteration. On the coarsest grids, which where still much finer than typical LES resolutions, leading-order errors were observed in the growth of the inversion height.

In order to estimate the capability of the front-tracking algorithm to remove errors due to numerical mixing at the cloud-top, a series of large-eddy simulation (LES) of the smoke cloud, a radiatively driven atmospheric boundary layer, were carried out. In this case, zero entrainment was specified with the level set method and only scalar advection was coupled. Simulations with and without the level set method were carried out where the numerical flux limiter and grid resolution were varied. Analysis of the vertically integrated turbulent kinetic energy and horizontal and vertical velocity variances showed that the dependence of the solution to both parameters was drastically reduced with the front-tracking algorithm. Using the standard LES, entrainment rate errors of 50 % to more than 150 % were observed relative to a theoretical estimate. With the level set method, these errors were reduced to less than 10 %.

An improved front-tracking algorithm that also couples diffusive scalar transport was used to simulate the stratocumulus-topped boundary layer (STBL) using a case based on observations during the DYCOMS II field campaign. Again, zero entrainment was specified and the algorithm's capability

of removing spurious mixing at the cloud-top was investigated. Entrainment rate errors were measured here relative to best estimates from DYCOMS II field data. Similar to the smoke cloud simulations, entrainment errors due to spurious mixing were reduced to values of less than 8 %.

In both applications, the idealistic smoke cloud case and the more realistic STBL, entrainment can effectively be controlled with the front-tracking algorithm. This ability is one the one hand an important tool to remove spurious cloud-top mixing in LES despite using relatively coarse grids. On the other hand, this ability is an important prerequisite to introduce accurate (super-)parameterization of entrainment in LES which will enable more accurate simulations of the STBL, both in terms of their general evolution as well as in terms of their detailed internal structure. While constant or algebraic models may be used, statistical one-dimensional models promise high accuracy. Meiselbach [39] carried out simulations of the radiatively driven smoke cloud using the one-dimensional turbulence (ODT) model [26] and showed that global statistics such as the entrainment rate could be accurately predicted, making ODT a promising candidate for superparameterizing cloud-top entrainment.

The presented front-tracking approach can be further improved by making the level set conservative. The synchronous evolution of the level set equation and the coupled scalar fields poses an overdetermination that causes instabilities in the numerical solution. The present implementation uses a non-conservative approach in order to resolve this, which causes net entrainment even if zero entrainment is prescribed. This can be circumvent if conservative synchronisation methods are used such as the one described by Waidmann et al. [88]. Entrainment mixing across the interface should be added where constant and algebraic parameterizations as well as superparameterizations based on ODT or other models are possible.

With such an improved front-tracking algorithm, high resolution LES of smoke cloud, for which accurate DNS data are available, would be most insightfull. For these, the front-tracking algorithm should be improved to handle breaking waves. Currently, the level-set coupling of the semi-implicit diffusion solver is based on the assumption, that this does not occur. Apart from stratocumulus clouds the presented front-tracking approach can be used for other stratified interfaces in the atmosphere and ocean as well. Especially in cases where important dynamics are tied to the interface, such as turbulent heat and mass exchange at the ocean surface.

Other possible improvements concern code reusability and computational performance. The level set equation can probably equally well be solved using the scalar finite-volume advection scheme. This would involve the same number of interpolations, but instead of the velocities, the level set function had to be interpolated onto the grid nodes. Also, level set reinitialization and the extrapolation used for generating interface boundary conditions could benefit from introducing convergence criterions in order to limit the number of iterations performed.

A THERMODYNAMIC APPENDIX

A.1 MIXING RATIO DEFINITIONS

The composition of air in large-eddy simulation (LES) is typically characterized by mixing ratios. Mixing ratios relate the mass of one component to a reference mass. Two definitions are frequently used and they differ in the choice of that reference. In this thesis, the ones consistent with Etling's book [17] are used where the components are related to the total mass of an air parcel. That is, for a parcel having the total mass m, the mixing ratio of an arbitrary component is

$$q_x = m_x / m \quad , \tag{A.1}$$

where the subscript x represents dry air (d), total water (t), water vapour (v), or liquid water (l). Sometimes, the dry air mass is used as a reference and mixing ratios are defined as

$$r_x = m_x / m_d \quad . \tag{A.2}$$

Then, by definition $r_d = 1$.

Mixture fractions of both definitions can directly be converted into each other. Dividing both the enumerator and denominator in Eq. (A.1) by the dry air mass one obtains

$$q_x = \frac{m_x}{m} = \frac{m_x / m_d}{m / m_d} = q_d r_x \quad . \tag{A.3}$$

Thus, for a multi-component fluid, the error between the two is given by $(1 - q_d)$. Specifically for moist air, a multi-phase fluid with only two components and $q_t = 1 - q_d$, the relative error is the total water mixing ratio itself

$$\frac{r_x - q_x}{r_x} = 1 - q_d = q_t \quad . \tag{A.4}$$

In most cases, q_d almost equals 1 in the atmosphere and only a small fraction of an air parcel's mass is water. In the case of stratocumulus, a typical value for the total water content q_t is $10\,\mathrm{g/kg} = 0.01$. Thus, r_x and q_x assume similar values.

A.2 THE FIRST LAW OF THERMODYNAMICS

The first law of thermodynamics reflects conservation of energy of a system in thermodynamic equilibrium. The internal energy contained in a system may be changed by work done by the system, i. e. expansion, or by exchange of heat, for instance in the form of radiation or conduction. This section gives a brief overview of various forms of the first law. More elaborate explanation and discussion can be found in textbooks such as the one by Etling [17].

The first law states that the specific internal energy u of a system can be changed through work w done by the system or through exchange of heat q with its environment. In differential form, this is expressed by

$$du = \delta q - dw \quad , \tag{A.5}$$

where δq is a small finite amount of heat exchanged with the environment. Assuming work is done against a constant environmental pressure p, the differential amount of work is $dw = p\,dv = p\,d(1/\rho)$. In moist systems, the internal energy may also change due to release or consumption of latent heat depending on the amount of condensation dq_l. Including this, the first law becomes

$$du = \delta q - dw + L_v\,dq_l \quad , \tag{A.6}$$

where L_v is the enthalpy of vaporization of water. Using $p\,dv = d(pv) - v\,dp$, an alternative form of the first law can be derived: Since both u and (pv) are state functions of an ideal gas, and their sum forms a new state function, known as the enthalpy h. Thus, the first law can be restated as

$$dh = v\,dp + \delta q + L_v\,dq_l = \frac{1}{\rho}dp + \delta q + L_v\,dq_l \quad . \tag{A.7}$$

It can be shown (via Joule's law) that both the internal energy and the enthalpy are directly related to the temperature of the system,

$$u = c_v T \tag{A.8}$$

$$h = c_p T \quad , \tag{A.9}$$

with c_v and c_p being the isochoric and isobaric heat capacities of the working fluid, respectively. Both are approximately constant for atmospheric conditions [17]. Typical values for c_p, c_v and L_v for dry air are listed in Tab. 8. With Eq. (A.9), the first law, Eq. (A.7), can be rewritten as

$$c_p\,dT = \frac{1}{\rho}dp + \delta q + L_v\,dq_l \quad . \tag{A.10}$$

And using the ideal gas law and dividing by T, one obtains

$$\frac{\delta q}{T} = c_p\frac{dT}{T} - R\frac{dp}{p} - \frac{L_v}{T}dq_l \quad , \tag{A.11}$$

with $R = c_p - c_v$ being the specific gas constant of the working fluid. For atmospheric flows, it is useful to consider adiabatic processes, i.e. processes where the enthalpy only changes due to the system performing work without exchange of heat ($\delta q = 0$). Such is the case for parcels lifted in the atmosphere due to their buoyancy or by winds breezing over mountains. For such processes, the first law simplifies to

$$0 = c_p\frac{dT}{T} - R\frac{dp}{p} - \frac{L_v}{T}dq_l \quad . \tag{A.12}$$

It is customary, do define temperatures that are indifferent to adiabatic changes, both for systems with and without phase changes. These are the potential and the liquid water potential temperature, respectively. Their derivation is explained in the next sections.

A.3 POTENTIAL TEMPERATURE

The potential temperature is defined as the temperature a dry air parcel at temperature T assumed if it was brought adiabatically from an arbitrary pressure level p to a reference pressure P. Typically the reference P is chosen to be 10^5 Pa, which is a typical air pressure at the sea level. The definition

equation can be obtained by integrating the adiabatic first law, Eq. (A.12), assuming no condensate is present, over this process. In this case, Eq. (A.12) becomes

$$\frac{dT}{T} = \kappa \frac{dp}{p} \quad , \tag{A.13}$$

where κ is the Poisson constant R/c_p. Using the fact that $dx/x = d\ln x$, Eq. (A.13) can be rewritten as

$$d\ln T = \kappa\, d\ln p \quad . \tag{A.14}$$

The integration from the reference state (θ, P) to an arbitrary end state (T, p) yields

$$\ln \frac{T}{\theta} = \kappa \ln \frac{p}{P} \quad , \tag{A.15}$$

which gives the potential temperature, after moving κ inside the logarithm and subsequently removing the logarithms, as

$$\theta = T \left(\frac{P}{p}\right)^{\kappa} = T\pi^{-1} \quad , \tag{A.16}$$

where π is the Exner pressure $(p/P)^{\kappa}$.

Using the potential temperature, a new form of the first law, Eq (A.11), can be derived. First, using logarithmic differentiation of the potential temperature equation (A.16), a new expression for $c_p\, dT/T$ can be found. Taking the natural logarithm of Eq. (A.16) gives

$$\ln T = \ln\theta + \kappa \ln p - \kappa \ln P \tag{A.17}$$

the differential of which is

$$d\ln T = d\ln\theta + \kappa\, d\ln p \quad . \tag{A.18}$$

Again, using $dx/x = d\ln x$, and multiplying by c_p one obtains

$$c_p \frac{dT}{T} = c_p \frac{d\theta}{\theta} + R\frac{dp}{p} \quad . \tag{A.19}$$

Replacing $c_p\, dT/T$ in Eq. (A.11) gives the first law in terms of the potential temperature differential as

$$\frac{\delta q}{T} = c_p \frac{d\theta}{\theta} - \frac{L_v}{T} dq_l \quad . \tag{A.20}$$

This equation confirms that that the potential temperature is in deed conserved ($d\theta = 0$) if (i) no phase changes occur ($dq_l = 0$) and (ii) the process is adiabatic ($\delta q = 0$). Note that θ remains conserved not only in dry air but also in moist unsaturated air and more generally, as long as the amount of condensate does not change. e.g. $q_l = 0 = \text{const}$.

Equation (A.20) can be used to derive an evolution equation for θ, by formally dividing by the time differential dt. Considering the case $dq_l = 0$, Eq. (A.20) becomes

$$\frac{dT}{dt} = \frac{\theta \dot{q}}{T c_p} \quad . \tag{A.21}$$

This equation describes the evolution of a material parcel along its path. An equation in the Eulerian frame of reference is obtained by expanding the total derivative of θ which gives

$$\frac{\partial\theta}{\partial t} + \boldsymbol{v}\cdot\nabla\theta = \frac{\theta\dot{q}}{T c_p} \quad . \tag{A.22}$$

A.4 LIQUID WATER POTENTIAL TEMPERATURE

The potential temperature θ is conserved in the case where no condensation or evaporation takes place. The liquid water potential temperature θ_l, originally proposed by Betts [6], is conserved approximately even if phase changes occur. Betts defines θ_l via the adiabatic first law, Eq. (A.20), as

$$c_p \frac{d\theta_l}{\theta_l} := c_p \frac{d\theta}{\theta} - \frac{L_v}{T} dq_l \quad . \tag{A.23}$$

The latent heat term can be expanded to

$$\frac{L_v}{T} dq_l = d\left(\frac{L_v q_l}{T}\right) - q_l \, d\left(\frac{L_v}{T}\right) \quad . \tag{A.24}$$

In order to integrate Eq. (A.23) more easily, the second term in this is typically neglected. (See Tripoli and Cotton [85] for a detailed discussion of this approximation.) Then, Eq. (A.23) becomes

$$c_p \frac{d\theta_l}{\theta_l} \approx c_p \frac{d\theta}{\theta} - d\left(\frac{L_v \, d_l}{T}\right) \tag{A.25}$$

which can be integrated to obtain

$$\theta_l \approx \theta \exp\left(-\frac{q_l L_v}{c_p T}\right) \quad . \tag{A.26}$$

Herein, the integration constant is dropped out by requiring $\theta_l(q_l = 0)$ to equal θ.

An evolution equation for the liquid water potential temperature θ_l is obtained in a similar way to the derivation for the potential temperature. Combining Eq. (A.23) and the first law of thermodynamics, Eq. (A.20), gives

$$c_p \frac{d\theta_l}{\theta_l} = \frac{\delta q}{T} \quad . \tag{A.27}$$

Dividing by the time differential dt and expanding the total time derivative gives the evolution equation

$$\frac{\partial \theta_l}{\partial t} + \boldsymbol{v} \cdot \nabla \theta_l = \frac{\theta_l \dot{q}}{T c_p} \quad . \tag{A.28}$$

The liquid water potential temperature is useful, because (i) it is approximately conserved under water phase changes, which the potential temperature is not, and (ii) it reduces to the potential temperature if no condensate is present.

A.5 PARAMETERS OF ATMOSPHERIC FLOW

Some parameters as used in the UCLA-LES are listed in Table 14.

A.6 EXNER PRESSURE GRADIENT

In the anelastic equations presented in Sect. 2.1.2, the dynamic pressure perturbation is formulated in terms of the Exner pressure

$$\pi = \left(\frac{p}{p_{\text{ref}}}\right)^{R/c_p} \quad . \tag{A.29}$$

Table 14: Parameters of atmospheric flow

Specific gas constant of dry air	$R_d = R$	287.04	$\mathrm{J\,(kg\,K)^{-1}}$
Specific gas constant of water vapor	R_v	461.5	$\mathrm{J\,(kg\,K)^{-1}}$
Isobaric specific heat of dry air	c_p	1005.0	$\mathrm{J\,(kg\,K)^{-1}}$
Volumetric specific heat of dry air	$c_v = c_p - R$	717	$\mathrm{J\,(kg\,K)^{-1}}$
Poisson constant	$\kappa = R/c_p$	0.2856	$[-]$
Isentropic exponent	γ	1.4	$[-]$
Enthalpy of vaporization of water	L_v	2.5×10^6	$\mathrm{J\,kg^{-1}}$
Gravitational acceleration	g	9.8	$\mathrm{m\,s^{-2}}$
Exner reference pressure	p_{00}	10^5	Pa

In order to obtain the appropriate Exner pressure term from the equation above, one can apply the Nabla operator and exploit the chain rule of differentiation.

$$\begin{aligned}\nabla\pi &= \nabla\left(\frac{p}{p_0}\right)^{R/c_p} \\ &= \frac{R}{c_p}\left(\frac{p}{p_0}\right)^{R/c_p-1}\frac{\nabla p}{p_0} \\ &= \frac{R}{c_p}\frac{\pi}{p}\nabla p\end{aligned}$$

The physical pressure p on the right hand side may be replaced by the ideal gas law $p = \rho R\theta\pi$. Doing so, one arrives at the relation

$$\frac{1}{\rho}\nabla p = c_p\theta\,\nabla\pi \quad . \tag{A.30}$$

A.7 THE CONTINUITY EQUATION IN (θ, π) COORDINATES

In their original derivation of the anelastic equations, Ogura and Phillips [49] formulate the continuity equation in terms of θ and π. The present review of their derivation in Sect. 2.1.2 uses the continuity equation formulated in terms of the density ρ.

$$\frac{\partial\rho}{\partial t} + \nabla\cdot(\rho\boldsymbol{v}) = 0 \quad . \tag{A.31}$$

This section shows that these two formulations are equivalent.

First, density is expressed as a function of potential temperature and the Exner pressure. This is done by using their respective definition equations, Eq. (2.4) and (2.6), to replace temperature and pressure in the ideal gas law (2.3). One obtains

$$\rho = \frac{p_{\mathrm{ref}}\pi^{(1/\kappa-1)}}{R\theta} \quad .$$

Then logarithmic differentiation, i.e. taking the natural logarithm and considering the differential, yields

$$-d\ln\rho = -\frac{d\rho}{\rho} = d\ln\theta + (1-1/\kappa)d\ln\pi \quad . \tag{A.32}$$

Here, the differentials involving R and p_{ref} drop out of the equation because they are considered constant. Second, the continuity equation (A.31) is stated in the Lagrangian form by expanding the divergence using the product rule and collecting the time derivative and the velocity divergence into the material time derivative. Devision by $(-\rho)$ yields

$$-\frac{1}{\rho}\frac{d\rho}{dt} = \nabla \cdot \boldsymbol{v} \quad . \tag{A.33}$$

Combining Eqs. (A.32) and (A.33) produces the continuity equation used by Ogura and Phillips [49]

$$\frac{d}{dt}\Big(\ln\theta + (1-1/\kappa)\ln\pi\Big) = \nabla \cdot \boldsymbol{v} \quad . \tag{A.34}$$

B

NUMERICAL APPENDIX

In the following, a possible strategy for including entrainment mixing in the front-tracking algorithm is presented. The strategy represents the boundary conditions for a contact discontinuity, as used in the front-tracking algorithm with zero entrainment, followed by an additional entrainment mixing event. The mixing event is based on three assumptions:

1. Turbulence at the cloud-top mixes only vertically. This is an approximation to mixing in the normal direction of the interface, which in the mean propagates vertically, opposing gravitation.

2. Turbulence leads to mixing equilibrium in cut cells within one time step (homogeneuous mixing). Entrainment mixes the conserved scalars (q, θ_l) homogeneously across all cut cells in that vertical column. Thus, the reconstructed scalar φ_0 below the interface reaches the same value φ_0^* in all cut cells in the column, that is

$$\varphi_{0,k_1} = \varphi_{0,k_2} = ... = \varphi_0^* \quad , \tag{B.1}$$

   where k_i index all cut cells in the current column.

3. The reconstruction above the interface, q_1, is given and constant during the mixing. As the entrainment interface propagates vertically into the free atmosphere, it consumes the clear air and mixes it into the boundary layer. Thus, the reconstructed state above the interface (φ_1) is known from the ghost fluid reconstruction before entrainment and is not changed by entrainment. Thus, the unknowns remaining to be solved for are the reconstructed values below the interface φ_0^*.

During the mixing event, it is required that the total mass of the mixed component remains constant. Since an equation is sought for the post-mixed values in the cells cut during the mixing event, the condition is applied to these cells only. This can be expressed by the conservation equation

$$\sum(\rho_k \varphi_k \Delta z_k)^n = \sum(\rho_k \varphi_k \Delta z_k)^{n+1} \tag{B.2}$$

where the φ_k are the cell averages in the kth vertical cell of the current column and the time levels n and $n+1$ indicate times before and after the entrainment mixing event, respectively. In order to derive an equation for the post-mixed states in cells cut during the mixing event, the cell averages are substituted by the decomposition

$$\varphi = (1 - \alpha)\, \varphi_0 + \alpha\, \varphi_1 \,. \tag{B.3}$$

According to Eq. (B.1), the conservation equation, Eq. (B.2), can be rewritten by substituting the post-mixing values in each cell k, $k+1$, etc. with the same reconstructed value φ_0^* and to obtain

$$\varphi_0^* = \frac{\sum(\rho_k \varphi_k \Delta z_k)^n - \sum(\rho_k \varphi_{1,k} \alpha_k \Delta z_k)^{n+1}}{\sum((1 - \alpha_k)\rho_k \Delta z_k)^{n+1} + \epsilon} \quad , \tag{B.4}$$

where the small number ϵ was introduced to remove the singularity. In cases where the interface remains in one cell in the considered column, Eq. (B.4) reduces to

$$\varphi_0^* = \frac{\varphi^n - (\alpha\varphi_1)^{n+1}}{(1-\alpha)^{n+1} + \epsilon} \quad . \tag{B.5}$$

Then, in one cut cell entrainment mixing is a conservative reconstruction based on the old cell averages and the new volume fractions equivalent to the decomposition of Eq. (B.3).

If entrainment shall be included, the ghost fluid method as presented in Sect. 3.3.3 can be augmented in the following way.

1. Advect ϕ with $\boldsymbol{v}_\phi = (0, 0, w_e)$ according to the level set equation, Eq. (2.97), where w_e is an externally defined entrainment velocity.
2. Extrapolate the ghost fluids φ_1 and φ_0 according to Eq. (3.33).
3. Compute the equilibrium mixing value φ_0^* according to Eq. (B.4), and assign it to the post-entrainment fluid φ_0^{n+1} in all cells cut during step 1.
4. Extrapolate the post-entrainment fluid φ_0^{n+1} using Eq. (3.33) beyond the cells cut during step 1 with the post-entrainment values as boundary conditions. This is a difference to the extrapolation used in the case without entrainment, where Ω_0 cells are included and only Ω_- cells serve as boundary conditions.

This procedure adds one extrapolation step to the generation of interface boundary conditions presented in Sects. 2.2.4 and 3.3.3, respectively. After the generation of the two fluids, the boundary layer fluid is according to the additional mixing event. This procedure involves one more extrapolation step than in the case without entrainment in order to propagate the mixed state across the interface.

C

ADDITIONAL RESULTS

The following figures show additional statistics of the simulations of the STBL presented in Chapt. 6.

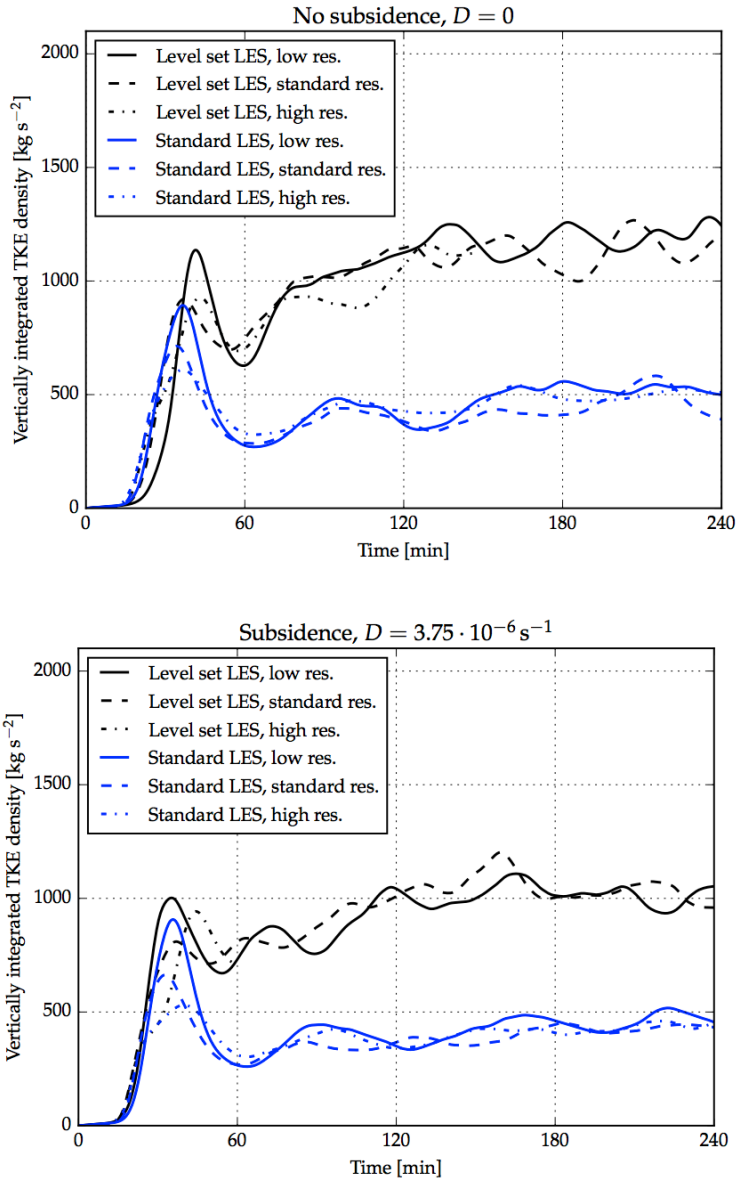

Figure 28: Evolution of the horizontal average of the vertically integrated TKE density (resolved + subgrid-scale) in the STBL for the case excluding (top) and including subsidence (bottom).

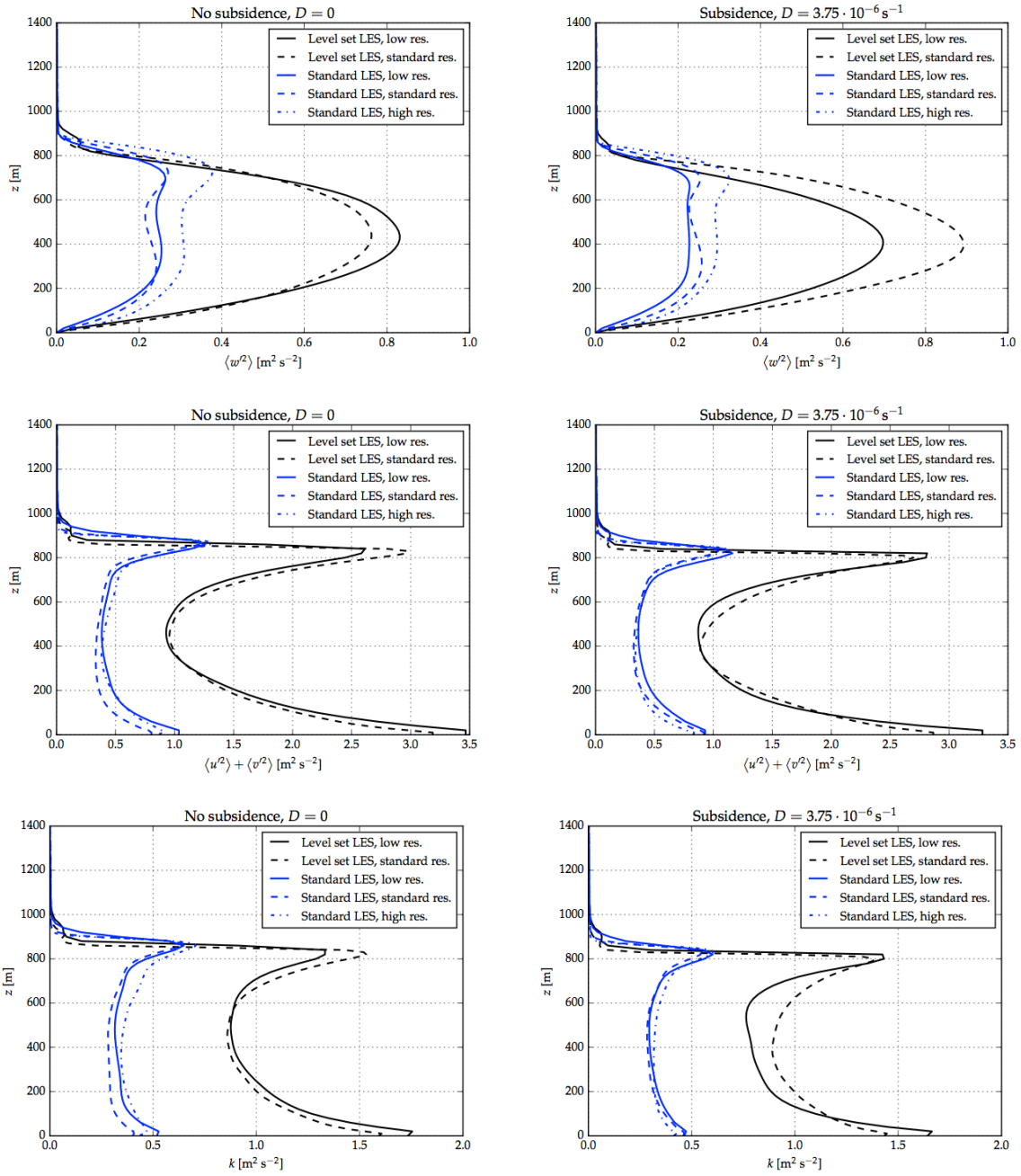

Figure 29: Profiles of various turbulence statistics of the resolved fields averaged over the third hour the STBL for the case excluding (left column) and including subsidence (right column). From top to bottom, the profiles shown are the vertical velocity variance $\langle w'^2 \rangle$, horizontal velocity variance $\langle u'^2 \rangle + \langle v'^2 \rangle$, and turbulent kinetic energy $k = 1/2(\langle u'^2 \rangle + \langle v'^2 \rangle + \langle w'^2 \rangle)$.

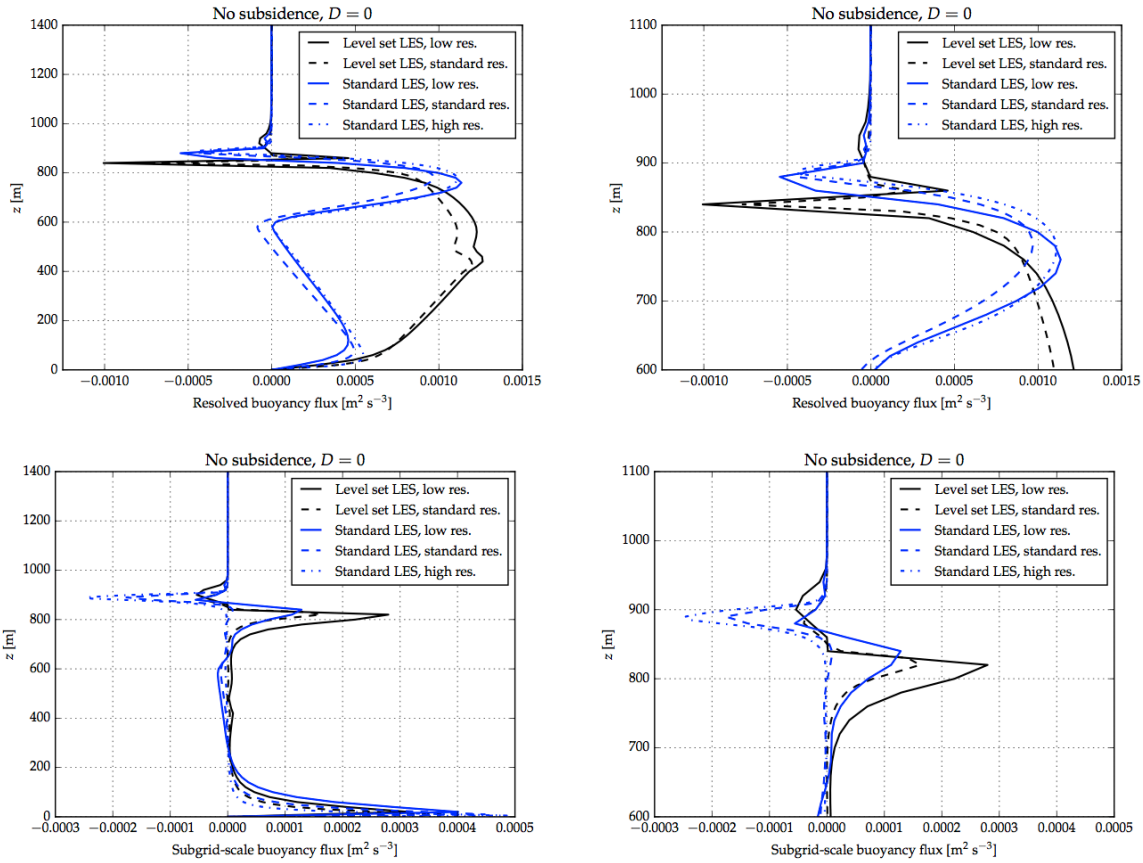

Figure 30: Profiles of the resolved (top) and subgrid-scale (bottom) vertical buoyancy fluxes in the STBL without subsidence averaged over the third hour. The left column shows the entire profile, the right column shows a closeup around the cloud-top.

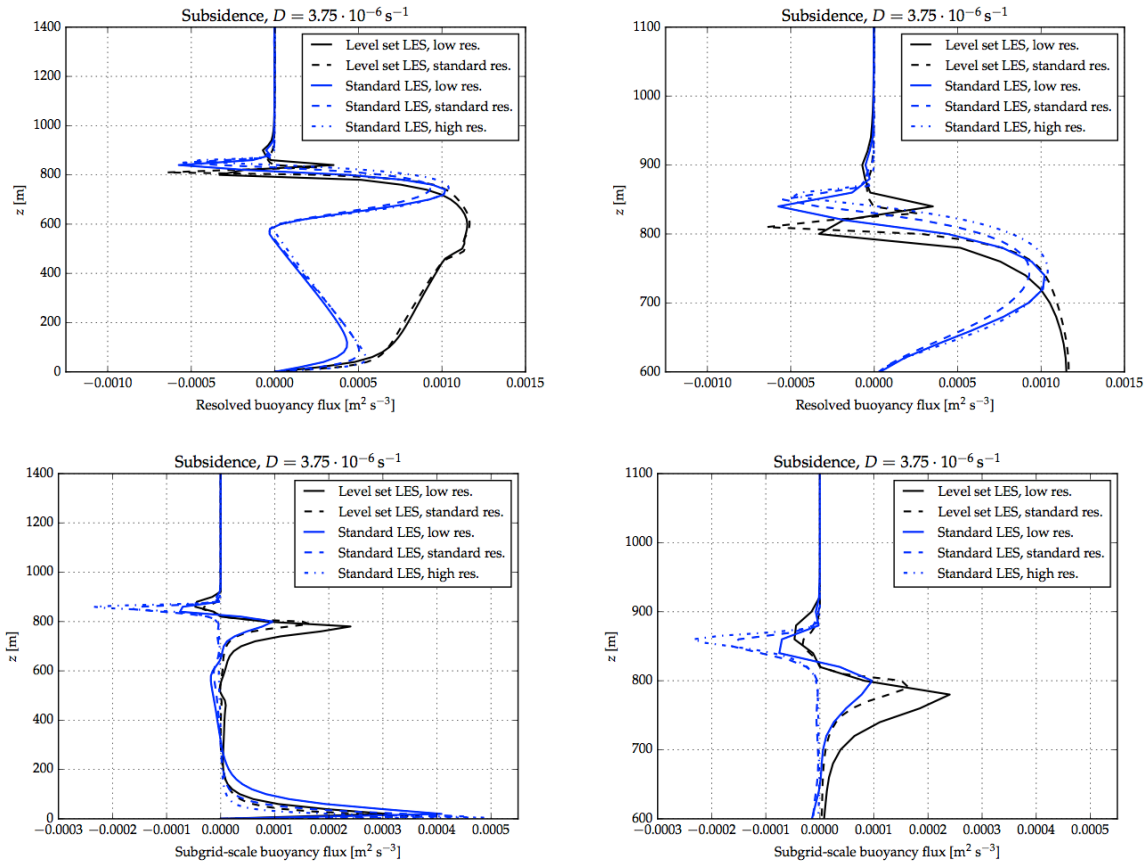

Figure 31: Profiles of the resolved (top) and subgrid-scale (bottom) vertical buoyancy fluxes in the STBL with subsidence averaged over the third hour. The left column shows the entire profile, the right column shows a closeup around the cloud-top.

BIBLIOGRAPHY

[1] Meteorology Glossary of the American Meteorological Society. URL http://glossary.ametsoc.org.

[2] Glossary of the NOAA's National Weather Service. URL http://w1.weather.gov/glossary/index.php.

[3] *International Cloud Atlas*, volume I. World Meteorological Organization, Geneva (Switzerland), revised edition, 1975. ISBN 9263104077.

[4] Andrew S. Ackerman, Margreet C. VanZanten, Bjorn Stevens, Verica Savic-Jovcic, Christopher S. Bretherton, Andreas Chlond, Jean-Christophe Golaz, Hongli Jiang, Marat Khairoutdinov, Steven K. Krueger, David C. Lewellen, Adrian Lock, Chin-Hoh Moeng, Kozo Nakamura, Markus D. Petters, Jefferson R. Snider, Sonja Weinbrecht, and Mike Zulauf. Large-Eddy Simulations of a Drizzling, Stratocumulus-Topped Marine Boundary Layer. *Monthly Weather Review*, 137(3):1083–1110, mar 2009. ISSN 0027-0644. doi: 10.1175/2008MWR2582.1. URL http://journals.ametsoc.org/doi/abs/10.1175/2008MWR2582.1.

[5] Gilles Bellon and Bjorn Stevens. Using the Sensitivity of Large-Eddy Simulations to Evaluate Atmospheric Boundary Layer Models. *Journal of the Atmospheric Sciences*, 69(5):1582–1601, may 2012. ISSN 0022-4928. doi: 10.1175/JAS-D-11-0160.1. URL http://journals.ametsoc.org/doi/abs/10.1175/JAS-D-11-0160.1.

[6] A. K. Betts. Non-precipitating cumulus convection and its parameterization. *Quarterly Journal of the Royal Meteorological Society*, 99(419):178–196, jan 1973. ISSN 00359009. doi: 10.1002/qj.49709941915. URL http://doi.wiley.com/10.1002/qj.49709941915.

[7] Sandrine Bony and Jean-Louis Dufresne. Marine boundary layer clouds at the heart of tropical cloud feedback uncertainties in climate models. *Geophysical Research Letters*, 32(20):L20806, 2005. ISSN 0094-8276. doi: 10.1029/2005GL023851. URL http://doi.wiley.com/10.1029/2005GL023851.

[8] Christopher S. Bretherton, M. K. Macvean, P. Bechtold, Andreas Chlond, W. R. Cotton, J. Cuxart, H. Cuijpers, M. Mhairoutdinov, B. Kosovic, D. Lewellen, Chin-Hoh Moeng, P. Siebesma, Bjorn Stevens, David E. Stevens, I. Sykes, and M. C. Wyant. An intercomparison of radiatively driven entrainment and turbulence in a smoke cloud, as simulated by different numerical models. *Quarterly Journal of the Royal Meteorological Society*, 125(554):391–423, jan 1999. ISSN 00359009. doi: 10.1002/qj.49712555402. URL http://doi.wiley.com/10.1002/qj.49712555402.

[9] Christopher S. Bretherton, Taneil Uttal, Christopher W. Fairall, Sandra E. Yuter, Robert A. Weller, Darrel Baumgardner, Kimberly Comstock, Robert Wood, and Graciela B. Raga. The EPIC 2001 Stratocumulus Study. *Bulletin of the American Meteorological Society*, 85(7):967–977,

jul 2004. doi: 10.1175/BAMS-85-7-967. URL http://journals.ametsoc.org/doi/abs/10.1175/BAMS-85-7-967.

[10] Alberto de Lozar and Juan Pedro Mellado. Direct Numerical Simulations of a Smoke Cloud-Top Mixing Layer as a Model for Stratocumuli. *Journal of the Atmospheric Sciences*, 70(8):2356–2375, aug 2013. ISSN 0022-4928. doi: 10.1175/JAS-D-12-0333.1. URL http://journals.ametsoc.org/doi/abs/10.1175/JAS-D-12-0333.1.

[11] Alberto de Lozar and Juan Pedro Mellado. Mixing driven by radiative and evaporative cooling at the stratocumuls top. *Journal of the Atmospheric Sciences*, page 150904104933002, 2015. ISSN 0022-4928. doi: 10.1175/JAS-D-15-0087.1. URL http://journals.ametsoc.org/doi/abs/10.1175/JAS-D-15-0087.1.

[12] J. W. Deardorff. Usefulness of Liquid-Water Potential Temperature in a Shallow-Cloud Model. *Journal of Applied Meteorology*, 15(1):98–102, jan 1976. ISSN 0021-8952. doi: 10.1175/1520-0450(1976)015<0098:UOLWPT>2.0.CO;2. URL http://journals.ametsoc.org/doi/abs/10.1175/1520-0450%281976%29015%3C0098%3AUOLWPT%3E2.0.CO%3B2.

[13] J. W. Deardorff. Cloud Top Entrainment Instability. *Journal of the Atmospheric Sciences*, 37(1):131–147, jan 1980. ISSN 0022-4928. doi: 10.1175/1520-0469(1980)037<0131:CTEI>2.0.CO;2. URL http://journals.ametsoc.org/doi/pdf/10.1175/1520-0469(1980)037<0131:CTEI>2.0.CO;2.

[14] Jacques Descloitres. Large Stratocumulus Deck Off The Coast Of Baja California, 2002. URL http://visibleearth.nasa.gov/view.php?id=58014.

[15] Eckhard Dietze, Juan Pedro Mellado, Bjorn Stevens, and Heiko Schmidt. Study of low-order numerical effects in the two-dimensional cloud-top mixing layer. In *Theoretical and Computational Fluid Dynamics*, volume 27, pages 239–251. Springer Berlin / Heidelberg, apr 2013. doi: 10.1007/s00162-012-0263-0. URL http://link.springer.com/10.1007/s00162-012-0263-0.

[16] Eckhard Dietze, Heiko Schmidt, Bjorn Stevens, and Juan Pedro Mellado. Controlling entrainment in the smoke cloud using level set-based front tracking. *Meteorologische Zeitschrift*, 23(6):661–674, jan 2015. ISSN 0941-2948. doi: 10.1127/metz/2014/0595. URL http://dx.doi.org/10.1127/metz/2014/0595.

[17] Dieter Etling. *Theoretische Meteorologie: Eine Einführung*. Springer Berlin / Heidelberg, 2002. ISBN 3540428151.

[18] Ronald Fedkiw, Tariq Aslam, Barry Merriman, and Stanley Osher. A Non-oscillatory Eulerian Approach to Interfaces in Multimaterial Flows (The Ghost Fluid Method). *Journal of Computational Physics*, 152(2):457–492, jul 1999. ISSN 00219991. doi: 10.1006/jcph.1999.6236. URL http://linkinghub.elsevier.com/retrieve/pii/S0021999199962368.

[19] Ronald Fedkiw, Tariq Aslam, and Shaojie Xu. The Ghost Fluid Method for Deflagration and Detonation Discontinuities. *Journal of Computational Physics*, 154(2):393–427, sep 1999. ISSN 00219991.

doi: 10.1006/jcph.1999.6320. URL http://linkinghub.elsevier.com/retrieve/pii/S0021999199963209.

[20] Joel H. Ferziger and Milovan Peric. *Numerische Strömungsmechanik*. Springer-Verlag Berlin Heidelberg, 2008. ISBN 978-3-540-67586-0. doi: 10.1007/978-3-540-68228-8. URL http://link.springer.com/10.1007/978-3-540-68228-8.

[21] Daniel Hartmann. *A Level-Set Based Method for Premixed Combustion in Compressible Flow*. Dissertation, RWTH Aachen, 2010.

[22] Daniel Hartmann, Matthias Meinke, and Wolfgang Schröder. Erratum to "Differential Equation Based Constrained Reinitialization for Level Set Methods" [J. Comput. Phys. 227 (2008) 6821-6845]. *Journal of Computational Physics*, 227(22):9696, nov 2008. ISSN 00219991. doi: 10.1016/j.jcp.2008.08.001. URL http://linkinghub.elsevier.com/retrieve/pii/S002199910800418X.

[23] Daniel Hartmann, Matthias Meinke, and Wolfgang Schröder. Differential equation based constrained reinitialization for level set methods. *Journal of Computational Physics*, 227(14):6821–6845, jul 2008. ISSN 00219991. doi: 10.1016/j.jcp.2008.03.040. URL http://linkinghub.elsevier.com/retrieve/pii/S0021999108001964.

[24] Daniel Hartmann, Matthias Meinke, and Wolfgang Schröder. The constrained reinitialization equation for level set methods. *Journal of Computational Physics*, 229(5):1514–1535, mar 2010. ISSN 00219991. doi: 10.1016/j.jcp.2009.10.042. URL http://linkinghub.elsevier.com/retrieve/pii/S0021999109006032.

[25] C.-Y. J. Kao, Y. H. Hang, Jon M. Reisner, and W. S. Smith. Test of the Volume-of-Fluid Method on Simulations of Marine Boundary Layer Clouds. *Monthly Weather Review*, 128(6):1960–1970, jun 1999. ISSN 0027-0644. doi: 10.1175/1520-0493(2000)128<1960:TOTVOF>2.0.CO;2. URL http://journals.ametsoc.org/doi/abs/10.1175/1520-0493(2000)128<1960:TOTVOF>2.0.CO;2.

[26] Alan R. Kerstein. One-dimensional turbulence: model formulation and application to homogeneous turbulence, shear flows, and buoyant stratified flows. *Journal of Fluid Mechanics*, 392:277–332, aug 1999. ISSN 00221120. doi: 10.1017/S0022112099005376. URL http://www.journals.cambridge.org/abstract_S0022112099005376.

[27] Ron Kimmel and James A. Sethian. Optimal Algorithm for Shape from Shading and Path Planning. *Journal of Mathematical Imaging and Vision*, 14:237–244, 2001.

[28] Steven K. Krueger. Linear Eddy Modeling of Entrainment and Mixing in Stratus Clouds. *Journal of the Atmospheric Sciences*, 50(18):3078–3090, sep 1993. ISSN 0022-4928. doi: 10.1175/1520-0469(1993)050<3078:LEMOEA>2.0.CO;2. URL http://journals.ametsoc.org/doi/abs/10.1175/1520-0469(1993)050<3078:LEMOEA>2.0.CO;2.

[29] Myoungkyu Lee and Robert D. Moser. Direct numerical simulation of turbulent channel flow up to $Re\tau = 5200$. *Journal of Fluid Mechanics*, 774(1987):395–415, jul 2015. ISSN 0022-1120. doi: 10.1017/jfm.2015.268. URL http://www.journals.cambridge.org/abstract_S0022112015002682.

[30] Sanjiva K. Lele. Compact finite difference schemes with spectral-like resolution. *Journal of Computational Physics*, 103(1):16–42, nov 1992. ISSN 00219991. doi: 10.1016/0021-9991(92)90324-R. URL http://linkinghub.elsevier.com/retrieve/pii/002199919290324R.

[31] Randall J. LeVeque. *Finite Volume Methods for Hyperbolic Problems*. Cambridge Univ. Press, Cambridge, 2002.

[32] D. K. Lilly. Models of cloud-topped mixed layers under a strong inversion. *Quarterly Journal of the Royal Meteorological Society*, 94(401): 292–309, jul 1968. ISSN 00359009. doi: 10.1002/qj.49709440106. URL http://doi.wiley.com/10.1002/qj.49709440106.

[33] Harvard Lomax, Thomas H. Pulliam, and David W. Zingg. *Fundamentals of computational fluid dynamics*. Springer, 1998.

[34] Len Margolin, Jon M. Reisner, and Piotr K. Smolarkiewicz. Application of the Volume-of-Fluid Method to the Advection-Condensation Problem. *Monthly Weather Review*, 125(9):2265–2273, sep 1997. ISSN 0027-0644. doi: 10.1175/1520-0493(1997)125<2265:AOTVOF>2.0.CO;2. URL http://journals.ametsoc.org/doi/abs/10.1175/1520-0493(1997)125<2265:AOTVOF>2.0.CO;2.

[35] G. Markstein. *Nonsteady flame propagation*. Pergamon Press, 1964.

[36] Georgios Matheou, Daniel Chung, Louise Nuijens, Bjorn Stevens, and Joao Teixeira. On the Fidelity of Large-Eddy Simulation of Shallow Precipitating Cumulus Convection. *Monthly Weather Review*, 139(9):2918–2939, 2011. doi: 10.1175/2011MWR3599.1.

[37] A. D. McEwan and G. W. Paltridge. Radiatively driven thermal convection bounded by an inversion-a laboratory simulation of stratus clouds. *Journal of Geophysical Research*, 81(6):1095–1102, feb 1976. ISSN 01480227. doi: 10.1029/JC081i006p01095. URL http://doi.wiley.com/10.1029/JC081i006p01095.

[38] Brian Medeiros, Bjorn Stevens, Isaac M. Held, Ming Zhao, David L. Williamson, Jerry G. Olson, and Christopher S. Bretherton. Aquaplanets, Climate Sensitivity, and Low Clouds. *Journal of Climate*, 21(19):4974–4991, oct 2008. ISSN 0894-8755. doi: 10.1175/2008JCLI1995.1. URL http://journals.ametsoc.org/doi/pdf/10.1175/2008JCLI1995.1.

[39] Falko Thorsten Meiselbach. *Application of ODT to Turbulent Flow Problems*. Dissertation, Brandenburg University of Technology, Cottbus-Senftenberg, 2015.

[40] Juan Pedro Mellado. The evaporatively driven cloud-top mixing layer. *Journal of Fluid Mechanics*, 660:5–36, jul 2010. ISSN 0022-1120. doi: 10.1017/S0022112010002831. URL http://www.journals.cambridge.org/abstract_S0022112010002831.

[41] Juan Pedro Mellado. private communication, 2011.

[42] Juan Pedro Mellado, Heiko Schmidt, Bjorn Stevens, and Norbert Peters. Analysis of the cloud-top mixing layer using DNS. Technical report, 2009.

[43] Juan Pedro Mellado, Bjorn Stevens, Heiko Schmidt, and Norbert Peters. Buoyancy reversal in cloud-top mixing layers. *Quarterly Journal of the Royal Meteorological Society*, 135(641):963–978, 2009. doi: 10.1002/qj.

[44] Juan Pedro Mellado, Bjorn Stevens, Heiko Schmidt, and Norbert Peters. Probability density functions in the cloud-top mixing layer. *New Journal of Physics*, 12(8), aug 2010. ISSN 1367-2630. doi: 10.1088/1367-2630/12/8/085010. URL http://stacks.iop.org/1367-2630/12/i=8/a=085010.

[45] Juan Pedro Mellado, Bjorn Stevens, Heiko Schmidt, and Norbert Peters. Two-fluid formulation of the cloud-top mixing layer for direct numerical simulation. *Theoretical and Computational Fluid Dynamics*, 24(6):511–536, feb 2010. ISSN 0935-4964. doi: 10.1007/s00162-010-0182-x. URL http://www.springerlink.com/index/10.1007/s00162-010-0182-x.

[46] Juan Pedro Mellado, Bjorn Stevens, and Heiko Schmidt. Wind Shear and Buoyancy Reversal at the Top of Stratocumulus. *Journal of the Atmospheric Sciences*, 71(3):1040–1057, mar 2014. ISSN 0022-4928. doi: 10.1175/JAS-D-13-0189.1. URL http://journals.ametsoc.org/doi/abs/10.1175/JAS-D-13-0189.1.

[47] Chin-Hoh Moeng, W. R. Cotton, Christopher S. Bretherton, Andreas Chlond, Marat Khairoutdinov, S. Krueger, W. S. Lewellen, M. K. Macvean, J. R. M. Pasquier, H. A. Rand, A. Pier Siebesma, Bjorn Stevens, and R. I. Sykes. Simulation of a Stratocumulus-Topped Planetary Boundary Layer: Intercomparison among Different Numerical Codes. *Bulletin of the American Meteorological Society*, 77(2):261–278, 1996.

[48] Chin-Hoh Moeng, Bjorn Stevens, and Peter P. Sullivan. Where is the Interface of the Stratocumulus-Topped PBL? *Journal of the Atmospheric Sciences*, 62(7):2626–2631, jul 2005. ISSN 0022-4928. doi: 10.1175/JAS3470.1. URL http://journals.ametsoc.org/doi/abs/10.1175/JAS3470.1.

[49] Yoshimitsu Ogura and Norman A. Phillips. Scale Analysis of Deep and Shallow Convection in the Atmosphere. *Journal of the Atmospheric Sciences*, 19(2):173–179, 1962.

[50] Stanley Osher and Ronald Fedkiw. *Level Set Methods and Dynamic Implicit Surfaces*. Springer Science+Busines Media, LLC, 2003. ISBN 978-038795482-0.

[51] Stanley Osher and Ronald P. Fedkiw. Level Set Methods: An Overview and Some Recent Results. *Journal of Computational Physics*, 169(2):463–502, may 2001. ISSN 00219991. doi: 10.1006/jcph.2000.6636. URL http://linkinghub.elsevier.com/retrieve/pii/S0021999100966361.

[52] Stanley Osher and James A. Sethian. Fronts propagating with curvature-dependent speed: Algorithms based on Hamilton-Jacobi formulations. *Journal of Computational Physics*, 79(1):12–49, nov 1988. ISSN 00219991. doi: 10.1016/0021-9991(88)90002-2. URL http://linkinghub.elsevier.com/retrieve/pii/0021999188900022.

[53] S. Planton. IPCC, 2013: Annex III: Glossary. In *Climate Change 2013: The Physical Science Basis. Contribution of Working Group I to the Fifth Assessment Report of the Intergovernmental Panel on Climate Change*, pages 1447–1466. Cambridge University Press, Cambridge, United Kingdom and New York, NY, USA, 2014. ISBN 978-1-107-66182-0. doi: 10.1017/

CBO9781107415324.031. URL http://ebooks.cambridge.org/ref/id/CBO9781107415324A040.

[54] Stephen B. Pope. *Turbulent flows*. Cambridge Univ. Press, Cambridge, 2000. ISBN 0-521-59125-2.

[55] David A. Randall. Conditional Instability of the First Kind Upside-Down. *Journal of the Atmospheric Sciences*, 37(1):125–130, jan 1980. ISSN 0022-4928. doi: 10.1175/1520-0469(1980)037<0125:CIOTFK>2.0.CO;2. URL http://journals.ametsoc.org/doi/pdf/10.1175/1520-0469(1980)037<0125:CIOTFK>2.0.CO;2.

[56] Giovanni Russo and Peter Smereka. A Remark on Computing Distance Functions. *Journal of Computational Physics*, 163(1):51–67, sep 2000. ISSN 00219991. doi: 10.1006/jcph.2000.6553. URL http://linkinghub.elsevier.com/retrieve/pii/S0021999100965537.

[57] Pierre Sagaut. *Large Eddy Simulation for Incompressible Flows*. Scientific Computation. Springer-Verlag, Berlin/Heidelberg, 2006. ISBN 3-540-26344-6. doi: 10.1007/b137536. URL http://link.springer.com/10.1007/b137536.

[58] Irina Sandu and Bjorn Stevens. On the Factors Modulating the Stratocumulus to Cumulus Transitions. *Journal of the Atmospheric Sciences*, 68(9):1865–1881, sep 2011. ISSN 0022-4928. doi: 10.1175/2011JAS3614.1. URL http://journals.ametsoc.org/doi/abs/10.1175/2011JAS3614.1.

[59] Bentley J. Sayler and Robert E. Breidenthal. Laboratory simulations of radiatively induced entrainment in stratiform clouds. *Journal of Geophysical Research*, 103(D8):8827, apr 1998. ISSN 0148-0227. doi: 10.1029/98JD00344. URL http://doi.wiley.com/10.1029/98JD00344.

[60] Heiko Schmidt and Rupert Klein. A generalized level-set/in-cell-reconstruction approach for accelerating turbulent premixed flames. *Combustion Theory and Modelling*, 7(2):243–267, jun 2003. ISSN 1364-7830. doi: 10.1088/1364-7830/7/2/303.

[61] Heiko Schmidt and Rupert Klein. Unpublished Code, 2010.

[62] Heiko Schmidt, Alan R. Kerstein, Scott Wunsch, Renaud Nédélec, and Ben J. Sayler. Analysis and numerical simulation of a laboratory analog of radiatively induced cloud-top entrainment. *Theoretical and Computational Fluid Dynamics*, 27(3-4):377–395, oct 2012. ISSN 0935-4964. doi: 10.1007/s00162-012-0288-4. URL http://link.springer.com/10.1007/s00162-012-0288-4.

[63] Thomas Schneider. *Verfolgung von Flammenfronten und Phasengrenzen in schwachkompressiblen Strömungen.* Dissertation, RWTH-Aachen, 2001.

[64] James A. Sethian. *Level Set Methods and Fast Marching Methods Evolving Interfaces in Computational Geometry, Fluid Mechanics, Computer Vision, and Materials Science*. Cambridge Univ. Press, 2nd editio edition, 1999.

[65] James A. Sethian and Peter Smereka. Level Set Methods for Fluid Interfaces. *Annual Review of Fluid Mechanics*, 35(1):341–372, jan 2003. ISSN 0066-4189. doi: 10.1146/annurev.fluid.35.101101.161105. URL http://www.annualreviews.org/doi/abs/10.1146/annurev.fluid.35.101101.161105.

[66] Chi-Wang Shu and Stanley Osher. Efficient implementation of essentially non-oscillatory shock-capturing schemes. *Journal of Computational Physics*, 77(2):439–471, 1988.

[67] Shenqyang S. Shy and Robert E. Breidenthal. Laboratory experiments on the cloud-top entrainment instability, 1990. ISSN 0022-1120.

[68] Steven T. Siems, Christopher S. Bretherton, Marcia B. Baker, Shenqyang Shy, and Robert E. Breidenthal. Buoyancy reversal and cloud-top entrainment instability. *Quarterly Journal of the Royal Meteorological Society*, 116(493):705–739, apr 1990. ISSN 00359009. doi: 10.1002/qj.49711649309. URL http://doi.wiley.com/10.1002/qj.49711649309.

[69] V. Smiljanovski, V. Moser, and Rupert Klein. A capturing - tracking hybrid scheme for deflagration discontinuities. *Combustion Theory and Modelling*, 1(2):183–215, feb 1997. ISSN 1364-7830. doi: 10.1088/1364-7830/1/2/004. URL http://www.tandfonline.com/doi/abs/10.1088/1364-7830/1/2/004.

[70] Raymond J. Spiteri and Steven J. Ruuth. A New Class of Optimal High-Order Strong-Stability-Preserving Time Discretization Methods. *SIAM Journal on Numerical Analysis*, 40(2):469–491, jan 2002. ISSN 0036-1429. doi: 10.1137/S0036142901389025. URL http://epubs.siam.org/doi/abs/10.1137/S0036142901389025.

[71] Bjorn Stevens. Entrainment in Stratocumulus Topped Mixed Layers. *Quarterly Journal of the Royal Meteorological Society*, 128(586):2663–2690, 2002. URL http://web.atmos.ucla.edu/~bstevens/Documents/mixed_layer.pdf.

[72] Bjorn Stevens. Atmospheric Moist Convection. *Annual Review of Earth and Planetary Sciences*, 33(1):605–643, may 2005. ISSN 0084-6597. doi: 10.1146/annurev.earth.33.092203.122658. URL http://www.annualreviews.org/doi/abs/10.1146/annurev.earth.33.092203.122658.

[73] Bjorn Stevens and Sandrine Bony. Climate change. What are climate models missing? *Science (New York, N.Y.)*, 340(6136):1053–4, may 2013. ISSN 1095-9203. doi: 10.1126/science.1237554. URL http://www.euclipse.eu/Publications/Stevens,Bony_Whatareclimatemodelsmissing.pdf.

[74] Bjorn Stevens and Axel Seifert. Understanding macrophysical outcomes of microphysical choices in simulations of shallow cumulus convection. *Journal of the Meteorological Society of Japan*, 86A:143–162, 2008. ISSN 0026-1165. doi: 10.2151/jmsj.86A.143. URL http://joi.jlc.jst.go.jp/JST.JSTAGE/jmsj/86A.143.

[75] Bjorn Stevens, Chin-Hoh Moeng, and Peter P. Sullivan. Large-Eddy Simulations of Radiatively Driven Convection : Sensitivities to the Representation of Small Scales. *Journal of the Atmospheric Sciences*, 56:3963–3984, 1999.

[76] Bjorn Stevens, Chin-Hoh Moeng, and Peter P. Sullivan. Entrainment and Subgrid Lengthscales in Large-Eddy Simulations of Atmospheric Boundary-Layer Flows. In Robert M. Kerr and Yoshifumi Kimura, editors, *IUTAM Symposium on Developments in Geophysical Turbulence*,

pages 253–269. Dordrecht: Kluwer, 2000. ISBN 978-94-010-0928-7. doi: 10.1007/978-94-010-0928-7_20. URL http://www.springerlink.com/index/10.1007/978-94-010-0928-7_20.

[77] Bjorn Stevens, Donald H. Lenschow, Ian Faloona, Chin-Hoh Moeng, D. K. Lilly, B. Blomquist, G. Vali, A. Bandy, T. Campos, H. Gerber, S. Haimov, B. Morley, and D. Thornton. On entrainment rates in nocturnal marine stratocumulus. *Quarterly Journal of the Royal Meteorological Society*, 129(595):3469–3493, oct 2003. ISSN 00359009. doi: 10.1256/qj.02.202. URL http://doi.wiley.com/10.1256/qj.02.202.

[78] Bjorn Stevens, Donald H. Lenschow, Gabor Vali, Hermann Gerber, A. Bandy, B. Blomquist, J.-L. Brenguier, C. S. Bretherton, F. Burnet, T. Campos, S. Chai, I. Faloona, D. Friesen, S. Haimov, K. Laursen, D. K. Lilly, S. M. Loehrer, Szymon P. Malinowski, B. Morley, M. D. Petters, D. C. Rogers, L. Russell, V. Savic-Jovcic, J. R. Snider, D. Straub, Marcin J. Szumowski, H. Takagi, D. C. Thornton, M. Tschudi, C. Twohy, M. Wetzel, and M. C. van Zanten. DYNAMICS AND CHEMISTRY OF MARINE STRATOCUMULUS–DYCOMS-II. *Bulletin of the American Meteorological Society*, 84(5):579–593, may 2003. ISSN 0003-0007. doi: 10.1175/BAMS-84-5-579. URL http://journals.ametsoc.org/doi/abs/10.1175/BAMS-84-5-579.

[79] Bjorn Stevens, Chin-Hoh Moeng, Andrew S. Ackerman, Christopher S. Bretherton, Andreas Chlond, Stephan de Roode, James Edwards, Jean-Christophe Golaz, Hongli Jiang, Marat Khairoutdinov, Michael P. Kirkpatrick, David C. Lewellen, Adrian Lock, Frank Müller, David E. Stevens, Eoin Whelan, and Ping Zhu. Evaluation of Large-Eddy Simulations via Observations of Nocturnal Marine Stratocumulus. *Monthly Weather Review*, 133(6):1443–1462, jun 2005. ISSN 0027-0644. doi: 10.1175/MWR2930.1. URL http://journals.ametsoc.org/doi/abs/10.1175/MWR2930.1.

[80] Bjorn Stevens, Anton Beljaars, Simona Bordoni, Christopher Holloway, Martin Köhler, Steven Krueger, Verica Savic-Jovcic, and Yunyan Zhang. On the Structure of the Lower Troposphere in the Summertime Stratocumulus Regime of the Northeast Pacific. *Monthly Weather Review*, 135(3):985–1005, 2007. ISSN 0027-0644. doi: 10.1175/MWR3427.1.

[81] David E. Stevens, John B. Bell, Ann S. Almgren, Vince E. Beckner, and Charles A. Rendleman. Small-Scale Processes and Entrainment in a Stratocumulus Marine Boundary Layer. *Journal of the Atmospheric Sciences*, 4(57):567–581, 2000.

[82] Mark Sussman, Peter Smereka, and Stanley Osher. A level set approach for computing solutions to incompressible two-phase flow. *Journal of Computational Physics*, 114(1):146–159, 1994.

[83] Mark Sussman, Ann S. Almgren, John B. Bell, Phillip Colella, Louis H. Howell, and Michael L. Welcome. An Adaptive Level Set Approach for Incompressible Two-Phase Flows. *Journal of Computational Physics*, 148(1):81–124, 1999. ISSN 00219991. doi: 10.1006/jcph.1998.6106. URL http://www.sciencedirect.com/science/article/pii/S002199919896106X.

[84] Mark Sussman, K. M. Smith, M. Y. Hussaini, M. Ohta, and R. Zhi-Wei. A sharp interface method for incompressible two-phase flows. *Journal*

of Computational Physics, 221(2):469–505, 2007. ISSN 00219991. doi: 10.1016/j.jcp.2006.06.020.

[85] Gregory J. Tripoli and William R. Cotton. The Use of Ice-Liquid Water Potential Temperature as a Thermodynamic Variable In Deep Atmospheric Models. *Monthly Weather Review*, 109(5):1094–1102, may 1981. ISSN 0027-0644. doi: 10.1175/1520-0493(1981)109<1094:TUOLLW>2.0.CO;2. URL http://journals.ametsoc.org/doi/abs/10.1175/1520-0493(1981)109<1094:TUOLLW>2.0.CO;2.

[86] Margreet C. VanZanten, Bjorn Stevens, Louise Nuijens, A. Pier Siebesma, A. S. Ackerman, F. Burnet, A. Cheng, F. Couvreux, H. Jiang, M. Khairoutdinov, Y. Kogan, D. C. Lewellen, D. Mechem, K. Nakamura, A. Noda, B. J. Shipway, J. Slawinska, S. Wang, and A. Wyszogrodzki. Controls on precipitation and cloudiness in simulations of trade-wind cumulus as observed during RICO. *Journal of Advances in Modeling Earth Systems*, 3(6):M06001, jun 2011. ISSN 1942-2466. doi: 10.1029/2011MS000056. URL http://doi.wiley.com/10.1029/2011MS000056.

[87] Matthias Waidmann. private communication, 2013.

[88] Matthias Waidmann, Stephan Gerber, Michael Oevermann, and Rupert Klein. A Conservative Coupling of Level-Set, Volume-of-Fluid and Other Conserved Quantities. In *Finite Volumes for Complex Applications VII-Methods and Theoretical Aspects*, volume 77, pages 457–465. 2014. ISBN 978-3-319-05683-8. doi: 10.1007/978-3-319-05684-5. URL http://link.springer.com/10.1007/978-3-319-05684-5.

[89] Robert Wood. Stratocumulus Clouds. *Monthly Weather Review*, 140(8):2373–2423, aug 2012. ISSN 0027-0644. doi: 10.1175/MWR-D-11-00121.1. URL http://journals.ametsoc.org/doi/abs/10.1175/MWR-D-11-00121.1.

[90] Scott Wunsch. Stochastic simulations of buoyancy-reversal experiments. *Physics of Fluids*, 15(6):1442, 2003. ISSN 10706631. doi: 10.1063/1.1572160. URL http://scitation.aip.org/content/aip/journal/pof2/15/6/10.1063/1.1572160.

[91] Takanobu Yamaguchi and David A. Randall. Large-Eddy Simulation of Evaporatively Driven Entrainment in Cloud-Topped Mixed Layers. *Journal of the Atmospheric Sciences*, 65(5):1481–1504, may 2008. ISSN 0022-4928. doi: 10.1175/2007JAS2438.1. URL http://journals.ametsoc.org/doi/abs/10.1175/2007JAS2438.1.

[92] Takanobu Yamaguchi and David A. Randall. Cooling of Entrained Parcels in a Large-Eddy Simulation. *Journal of the Atmospheric Sciences*, 69(3):1118–1136, mar 2012. ISSN 0022-4928. doi: 10.1175/JAS-D-11-080.1. URL http://journals.ametsoc.org/doi/abs/10.1175/JAS-D-11-080.1.

DECLARATION

I hereby certify that this thesis has been composed by me and is based on my own work, unless stated otherwise. No other person's work has been used without due acknowledgement in this thesis. All references and verbatim extracts have been quoted, and all sources of information, including graphs and data sets, have been specifically acknowledged.

Hiermit erkläre ich an Eides statt, dass ich die vorliegende Arbeit selbstständig und nur unter Zuhilfenahme der ausgewiesenen Hilfsmittel angefertigt habe. Sämtliche Stellen der Arbeit, die im Wortlaut oder dem Sinn nach anderen gedruckten oder im Internet verfügbaren Werken entnommen sind, habe ich durch genaue Quellenangaben kenntlich gemacht.

Cottbus, July 2016

Eckhard Kadasch

COLOPHON

This document was typeset using the typographical look-and-feel `classicthesis` developed by André Miede. The style was inspired by Robert Bringhurst's seminal book on typography "*The Elements of Typographic Style*". `classicthesis` is available for both LaTeX and LyX:

`http://code.google.com/p/classicthesis/`

Happy users of `classicthesis` usually send a real postcard to the author, a collection of postcards received so far is featured here:

`http://postcards.miede.de/`